
State Estimation of Autonomous Surface Vessel

Project Report
932

Aalborg University



Master Thesis

**Master's Program in
Control and Automation**

Department of Electronic Systems

Fredrik Bajers Vej 7C, 9220 Aalborg

Title:

Precision Control of an Autonomous Surface Vessel

Theme:

Multivariable Control

Project Period:

Fall 2017 - Spring 2018

Project Group:

832

Participants:

Anders Egelund Kjeldal

Supervisor:

Jesper Abildgaard Larsen

Pages: 114

Concluded: 6/09/2018

Synopsis:

The aim of this project is to design an estimation filter with the goal performing hydrographic measurements. A mathematical model of the vessel provided by Aalborg University is presented, which will be used to design an estimator able to provide the precision required to perform hydrographic Measurements. This is done utilizing an Inertial Measurement Unit (IMU) and a Real Time Kinematic (RTK) GPS to provide the necessary measurements. The estimation technique used in this project is an Extended kalman filter, which utilizes the model derived to provide a 6DOF estimate needed for hydrographic measurements.

Publication of this report's contents (including citation) without permission from the authors is prohibited

Contents

1 Preliminary Analysis	6
1.1 Introduction	7
1.2 Purpose	7
1.3 Problem Analysis	8
1.4 Requirements	13
2 System Analysis	14
2.1 Notation	14
2.2 System Description	17
3 Model Derivation	26
3.1 Hydrodynamic Forces	27
3.2 Rigidbody Dynamics	31
3.3 Hydrostatic Forces	32
3.4 Actuation Model	35
3.5 Sensor Noise	36
4 Sensor Fusion Design	41
4.1 Sensor Fusion	42
4.2 System Design	45
4.3 Implementation	47
5 Kalman Filter Design	49
5.1 Discretization	49
5.2 Verification of Discretization	52
5.3 Kalman Colored Noise Compensation	54
5.4 Kalman Bias Drift Compensation	55
5.5 Multi Rate Kalman Filtering	56
5.6 Simulation Results	57
6 Conclusion	65
7 Future Work	66
A Appendix	67
B Determination of Hydrodynamic and hydrostatic coefficients	68
B.1 Results	81
B.2 Conclusion	82
C Extracting Pull Test Data	83
C.1 Stim Driver: Datagram extraction	85
D Noise Test: IMU	87
D.1 Evaluation	90

Contents

E IMU Whiteness test	92
E.1 Theory:	92
E.2 Results	92
F Measurement Journal: IMU misalignment	100
G Coriolis and Centripetal Matrix	107
H Kalman Veification	109

1 | Preliminary Analysis

This chapter contains the Introduction, problem analysis of the system, its use case and the derivation of the system model. This will be used as a basis to the definition of the system requirements.

1.1 Introduction

Seaborn trade is responsible for transporting up to 90% of the goods on a global scale, as it is comparatively cheap and the most environment friendly way of transporting goods. [1] A requirement for sea born transport to work is that the goods must be transported between ports, meaning a ports ability to handle the load of transporting ships is important, as potential bottlenecks could limit the throughput of a said port, resulting in a net loss overall.

In specific cases, the bottlenecks might not be linked to the port itself, but rather it's surroundings. If the waters are particular shallow leading into a port, this might physically limit the amount of traffic that can get into that port, as transport ships might be forced to use dedicated lanes only capable of supporting transport in one direction at a time.

Such a case is applicable to transporting goods through the Limfjord, where sea fare between Egholm and Kattegat is regulated so that inbound ships is required to wait in a dredged channel at Hals Barre.[2]

This is required because the waters in The Limfjord is shallow, so that not all areas are passable by vessels with a deep keel. This makes the navigation of large ships difficult, as there only exists a few places where it's known to be deep enough for such ships to safely pass.

However, precaution might not be necessary as some parts of the Fjord could be temporarily deep enough to pass through, however, without sufficient knowledge of the seafloor, this is not possible. Such knowledge is obtained by mapping the depth of the seafloor relative to a position so that the potential additional fairways are known. This is know as a Hydrographic map. A hydrographic map describes the depth of the seabed and location of potential hazardous features relevant for navigation. Hydrographic survey is most commonly performed using multibeam echo sounders, which is swept over an area, to measure the depth, location of underwater features which is crucial for navigating shallow waters, like the ones in the Limfjord. The measured depth is then combined with a GPS position, to generate the depth map of the search area.[3] If a sufficient hydrographic map is available, temporary fairways could be utilized, allowing more ships to pass at once by removing the bottleneck.

However, as the seabed is constantly changing from effects such as shifting sands, maintaining a hydrographic map is cumbersome. Shifting sands is when the sand on the seafloor moves causing underwater dunes to form, meaning a potential hydrographic map must be updated regularly to stay relevant.

To prevent an excessive amounts of manpower maintaining the depth map, an autonomous system could be implemented through usage of Autonomous Surface vessels (ASV), capable of performing hydrographic measurements of the seabed.

1.2 Purpose

The purpose of this project is to design an autonomous system capable to perform bathymetric measurements of the Limfjord. A platform for this have been supplied by Aalborg University

and its components is described in section 2.2. This platform will be the basis for the project, where its dynamic behavior must be determined in order to for it to be modeled. The system must be designed in such that it is capable of performing measurements according to existing standards for hydrographic mapping. The focus of this project is to improve the quality of the measurements through advanced estimation theory.

1.3 Problem Analysis

To create a hydrographic map of the ocean floor, bathymetric measurements must be related to a set of GPS-coordinates. This is done by sweeping over the seabed within the targeted area to measure the depth for the entire targeted area. By combining the bathymetric measurements with GPS locations, a map of the seabed is created.

The accuracy of the bathymetric measurements is depending on the accuracy of the measured states of the system. The more uncertainty these states experiences, the more uncertainty of the position of the measurements there is. The S-44 IHO standard for bathymetric describes the requirements when performing such measurements.[4] This establishes different categories of hydrographic measurements, where the intended use case falls under the Special order category. This category includes under keel measurements of the sea floor, and maximum total horizontal uncertainty (THU) of 2m with a 95% confidence interval.[4] The special order is the strictest category defined in the S-44 IHO standard, and is used for depths of up to 40m, however The Canadian Hydrographic Services specifies a stricter category, namely the Exclusive order.[5] This standard is intended for hydrographic mapping of shallow water areas, like the ones found in the Limfjord. This category specifies a 95% confidence interval of the THU of 1 m, however further specifies that all error sources must be minimized.[5]

As the mapping is reliant on measured data to determine its position and orientation, it is also sensitive to measurement noise. Measurement noise reduction is desired to get the most accurate mapping of the seabed. By fusing all the measured states of the system, a better estimation of the states can be made. Additionally this allows the system to estimate states not measured by the sensors directly, giving additional data. This does not only improve the accuracy of the mapping, but also the accuracy of the controller, which in turn potentially increases the speed of the mapping.

To function autonomously, the system needs a control scheme. While the specific pattern used to map the seabed might be dependent on the use case, a more precise controller allows for wider sweeps because less error margins is required, allowing it perform less conservative sweeps. The design of such systems impact the performance of the vessel and a good control scheme can potentially increase survey speeds and operating range of the individual vessel. Many considerations arises when designing a sufficient control scheme, the robustness of the system in relation to wave and parameter disturbances, the efficiency in relation to speed and fuel cost, robustness towards trajectory deviations and more.

While the development of a control scheme is required for the system to perform autonomous measurements, it is not within the scope of this project to design one. Instead the focus will be

obtain a model of the system and through that design a estimator able to perform hydrographic measurements.

For an autonomous system operating in a non controlled environment safety features is needed. The system needs to be able to detect obstacles and replan the route to avoid coalitions. While stationary obstacles such as debris is relatively trivial to avoid, moving obstacles such as ships are more challenging as the speed and trajectory of the ship have to be accounted for. One solution to this could be to wait till the vessel have passed and resume mapping. If some fault arises, the system needs to be able to handle that. Depending on the situation, it might be optimal for the vessel to either shut down and let crew retrieve it, or sail back to dock on its own. While a finished system must be able to handle faults, the scope of this project does not involve such measures and it is deemed sufficient for the system to simply shut down, and let the operators steer it back to be maintained.

1.3.1 Design Considerations

Figure 1.1 illustrates some of the external disturbances the system can experience. These disturbances are primarily from two sources, constant and wave disturbances.

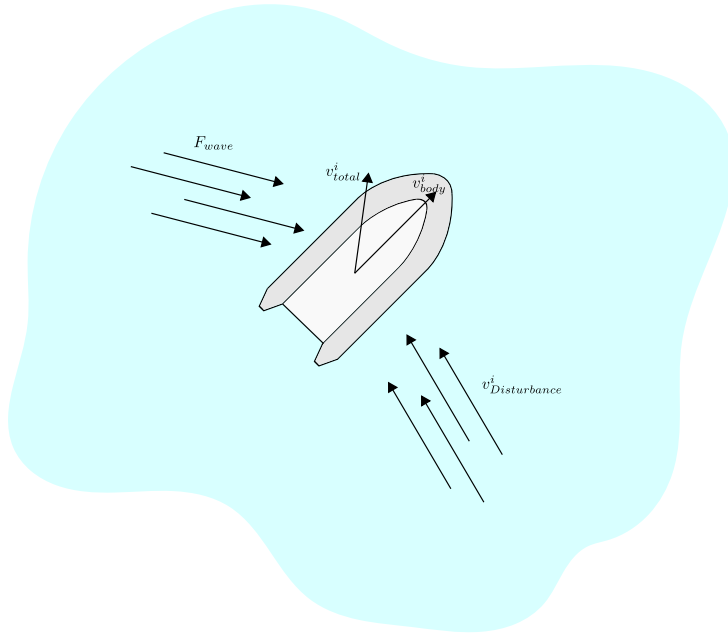


Figure 1.1: Illustration of external disturbances experienced by the vessel

The constant disturbances are a combination of the wind and the velocity of the water. These disturbances are assumed to primarily originate from the velocity of the water, which drags the vessel with it, resulting in an altered velocity vector, as these impact the vessel when moving through the water. This type of disturbance alters the trajectory, as the velocity vector of the vessel gets altered. This must be compensated for by the controller, for the system to follow the planned path. In the current configuration, the system is not equipped with the sensors

Chapter 1. Preliminary Analysis

necessary to measure these disturbances, however they can possibly be estimated by using the proper techniques.

The wave disturbances are assumed to be sinusoidal torques acting on the system. These are assumed to be zero-mean, as the velocity of the water are already accounted for, thus any potential bias in the waves is included in the velocity. This leads to complications in the mapping, as the beam travels further than needed and measures a different region of the seabed. Ideally the sweeping width would be the width of the sensor, however as the vessel is prone to disturbances, sweeping width must be reduced.

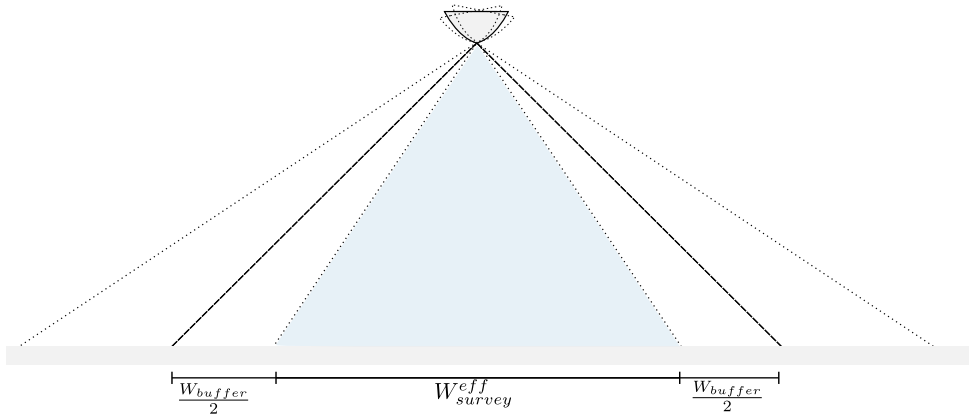


Figure 1.2: Effect of disturbance on survey width W_{survey}

Figure 1.2 illustrates how a deviation in θ_n affect the sweeping width W_{survey} . If the vessel experiences a disturbance in θ_n , the area the sensor covers moves. The effective survey area W_{survey}^{eff} is the area which is covered by the sensor independent of disturbances. From Figure 1.2 it can be seen that this area decreases as the difference in orientation increases. For this project the expected disturbances in θ_n is set to be between $0 - 10^\circ$.

While the disturbances effects the sweep width, The THU is not affected by this as the position and orientation of the vessel is measured, and can thus be accounted for. The THU is dependent on the uncertainty of the measurements. An uncertainty in the position of the vessel of $\pm(x, y)$ meters will correspond to an equal uncertainty in the position of the measurements.

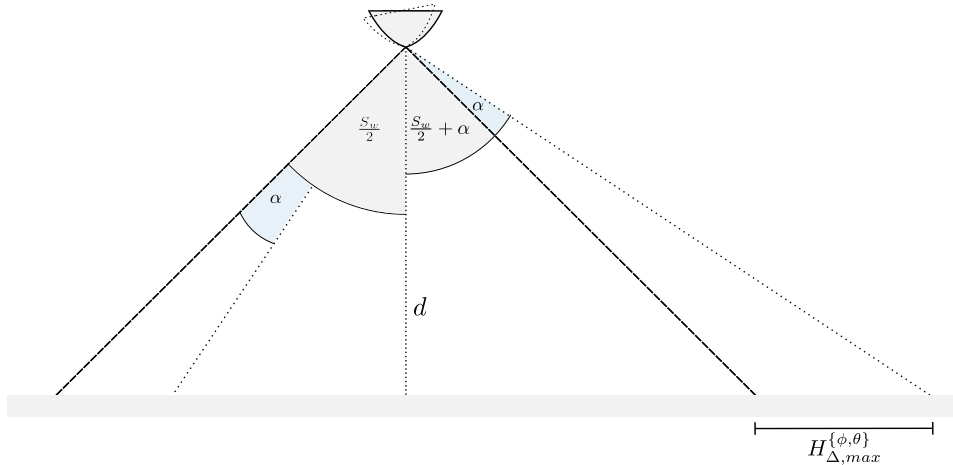


Figure 1.3: Illustration of how uncertainties in orientation affects THU

Figure 1.3 illustrates how an uncertainty in roll and pitch effects the THU. If the system experiences an uncertainty of in θ or ϕ this will contribute to an unknown shift in the position of the measurements, $H_{\Delta}^{\theta,\phi}$, where H_{Δ}^{ϕ} denotes the shift caused by an uncertainty in ϕ and vice versa. The upper bound of this shift can be found by trigonometry to be:

$$H_{\Delta,max}^{\phi,\theta} = d \cdot \tan\left(\frac{S_w}{2} + \alpha^{\{\phi,\theta\}}\right) - d \cdot \tan\left(\frac{S_w}{2}\right) \quad (1.1)$$

Where:

$\alpha^{\{\phi,\theta\}}$	is the uncertainty in ϕ or θ	[rad]
S_w	is the angle at which the sensor is able to measure	[rad]
d	is the depth at which the measurement is taken	[m]

The deviation in ψ also contributes to the THU.

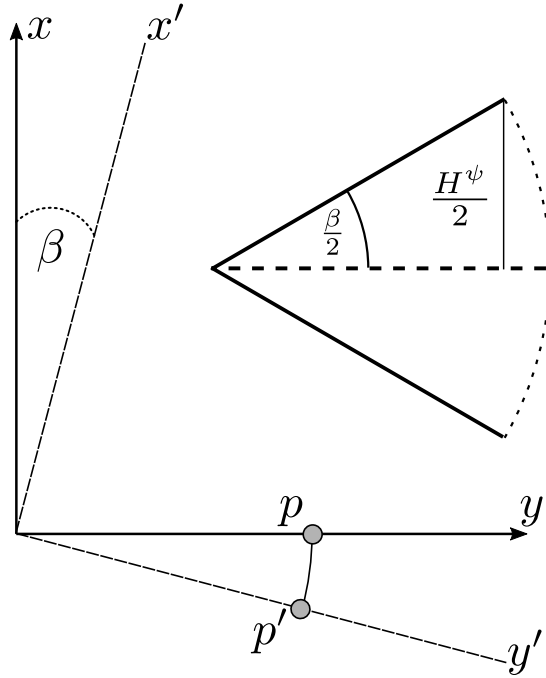


Figure 1.4: Illustration of the contribution from deviations in ψ to THU

Figure 1.4 illustrates how an uncertainty in ψ results in a rotation of point, p to p' . The THU contribution of deviations in ψ is therefore:

$$H_{\Delta,max}^{\psi} = 2\sqrt{p_x^2 + p_y^2} \cdot \tan(\frac{\beta}{2}) \quad (1.2)$$

Where:

$p_{\{x,y\}}$	Is the coordinate of p along the respective axis in {n}	[m]
β	Is the 95% confidence interval of deviations in ψ	[rad]

The uncertainty caused by ψ increases the further p is from the origin of {b}, meaning the largest uncertainty is seen in the edge of the search area.

In addition to the uncertainty in the orientation, the uncertainty in the position of {b} within {n} also influences the THU. While the orientation is dependent on the projection of the hydrographic measurements on the seabed, the GPS positions contribution to the THU is directly proportional to the accuracy of the receiver as it corresponds to an unknown value added of the measured position.

The combined THU for the vessel then becomes:

$$THU = \sqrt{H_{\Delta,max}^{\phi}^2 + H_{\Delta,max}^{\theta}^2} + H_{\Delta}^{\psi} + \sqrt{x_{\Delta,n}^2 + y_{\Delta,n}^2} \quad (1.3)$$

As a result of Equation 1.3, the THU is a combination of uncertainties in x_I , y_I , z_I , ϕ_I , θ_I , ψ_I , which all influence the accuracy of the bathymetric measurement.

1.4 Requirements

From section 1.3.1 it was determined that the maximum allowable THU is $\pm 1m$.

As stated in subsection 2.2.5, the GPS supplied have a horizontal resolution of $< 12mm$, assuming RTK GPS is used. At the current stage in the development of the platform RTK capabilities have not been set up properly, meaning the precision is expected to be significantly worse. As the RTK capabilities of the sensor is unverified, for the sake of this project an assumed horizontal resolution of $< 24mm$ is used.

The max depth of the Limfjord is 24m[6], from this the maximum allowable deviations can be determined using Equation 1.3. The THU is a combination of the uncertainties, meaning the upper limits is found using a combination of knowledge about the sensor capabilities as well as what is estimated to be feasible.

As Equation 1.3 uses the theoretical maximum sweep width of the sensor based on the expected disturbance, the requirements for the precision of the state estimator can be relaxed by further reducing this width, as this would reduce the sensitivity to deviations in the furthest away points. Additionally, it is important to notice that while the total THU is more sensitive to uncertainties of ϕ than θ due to the sweep width being significantly larger in ϕ than θ , the measurements originate from the same sensor, which means the expected obtainable uncertainty is roughly the same. This results in the following functional requirements:

- A:** The system must be able to estimate the orientation and position of the vessel relative to $\{n\}$.
- B:** The total THU must not exceed $1m$ at a 95% confidence level.
- C:** The accuracy of ϕ_n and θ_n must not exceed 0.3438° with a 95% confidence level.
- D:** The accuracy of ψ_n must not exceed 0.25° with a 95% confidence level.

2 | System Analysis

This chapter describes the platform and it's components available for this project as well as the conceptual framework necessary for system design

2.1 Notation

The standard notation used for maritime purposes is defined by the *Society of Naval Architects and Naval Engineers* (SNAME), which can be seen in table 2.1. While the specific notation of the coordinate system is similar, the time derivatives is described by using overdot[7] notation instead of the traditional SNAME notation as this is found to be more intuitively readable. An example of overdot notation is show in Equation 2.1

$$\dot{x} \triangleq \frac{dx}{dt} \quad (2.1)$$

Consecutive time derivations is denoted by increasing the number of dots.

DoF	Force/Moment	Velocity (linear and angular)	position
motion in x direction (surge)	F_x	\dot{x}	x
motion in y direction (sway)	F_y	\dot{y}	y
motion in z direction (heave)	F_z	\dot{z}	z
rotation about x axis (roll)	τ_ϕ	$\dot{\phi}$	ϕ
rotation about y axis (pitch)	τ_θ	$\dot{\theta}$	θ
rotation about z axis (yaw)	τ_ψ	$\dot{\psi}$	ψ

Table 2.1: notation for forces and momentum, velocities and positions

The SNAME convention models the movement of a vessel a 6-DOF translation of a body-fixed frame, ($\{b\}$) within the earth-fixed frame ($\{n\}$), which is assumed to be the inertial frame. Additionally, some parameters is described in relation to a specific frame, such as the translator velocities. The term translational will be used to indicate positional coordinates, meaning translational velocities refer to a rate of change of (x, y, z) while angular velocity refer to rate of change in Euler angles.

To distinguish between the velocities in relation to $\{n\}$ and $\{b\}$, the parameters are denoted by a subindex of $_n$ or $_b$ respectively.

The vectors $v := (\dot{x}, \dot{y}, \dot{z})^T$ and $\omega := (\dot{\phi}, \dot{\theta}, \dot{\psi})^T$ are used to denote the transnational and angular velocities respectively.

The position in $\{n\}$ is denoted $\eta := (n_b, y_n, z_n, \phi, \theta, \psi)^T \in \mathbb{R}^6$, indicating the translational and angular velocities in $\{n\}$. Similarly, velocity vector $\nu := (v_b, \omega_b)^T \in \mathbb{R}^6$ is used when describing both the angular and translational velocities of the body frame in relation the NED frame. These notations is used for convenience when referring to a frame as a whole.

If the velocities is denoted by ν_R it describes the relative speed, meaning the speed of the body frame in relation to the speed of the water. This will mostly be used when related to the dynamic equations.

2.1.1 Reference Frames

In order to describe the dynamics of the vessel, two reference frames are used, the body frame and the North-East-Down (NED) frame.

The body frame is denoted as:

$$\{b\} := (x_b, y_b, z_b) \quad (2.2)$$

Where:

x_b	describes the position relative to surge axis	[m]
y_b	describes the position along sway axis	[m]
z_b	describes the position in the heave direction	[m]

Figure 2.1 illustrates how these frames are located relative to the vessel.

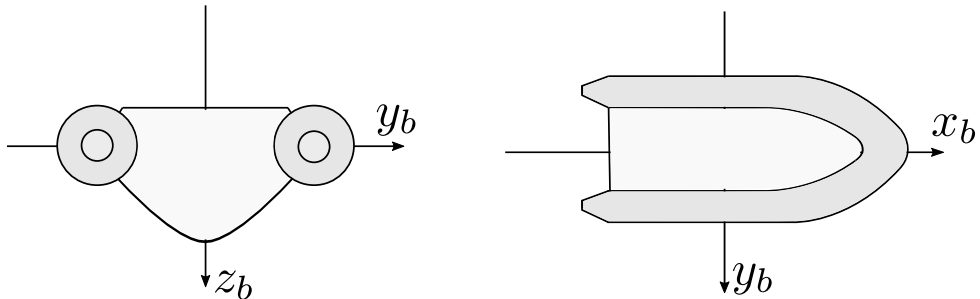


Figure 2.1: Illustration of body frame

This frame describes the forces acting on the vessel relative to the body of the vessel, and will be used when deriving the dynamic equations.

When navigating the system, it is required to know the position relative to the earths surface. This is accomplished using the NED frame. The positional coordinates of the NED frame are defined by:

$$\{n\} := (x_n, y_n, z_n) \quad (2.3)$$

The NED frame is assumed to be the inertial axis.

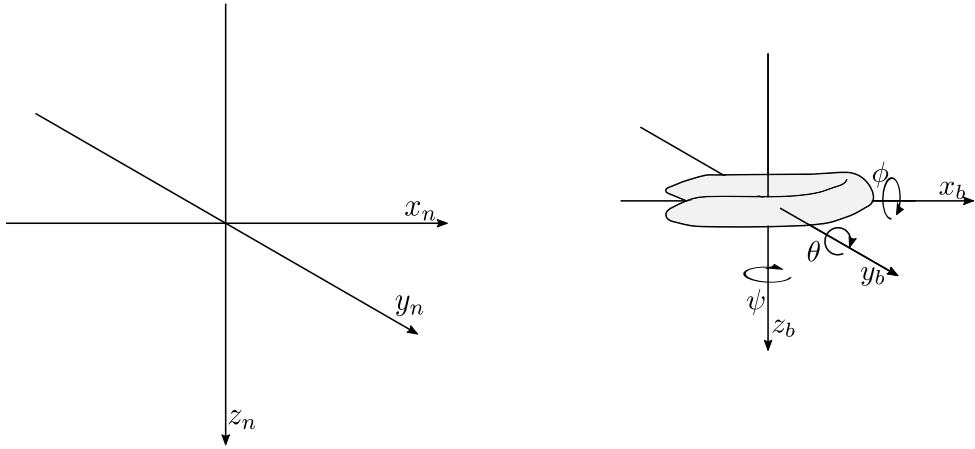


Figure 2.2: Illustration of {b} within {n}

Figure 2.2 illustrates how the two frames relate. The inertial frame {n} is considered stationary, and {b} moves in relation to this. Similarly, the orientation (ϕ, θ, ψ) relates to the orientation of {b} within {n}.

In order to describe movement within the {b} frame in the {n} frame, Equation 2.4 can be used.

$$\frac{^n d}{dt} \vec{a} = \frac{^b d}{dt} \vec{a} + \vec{\omega}_{b/i} \times \vec{a} \quad (2.4)$$

Where:

$\frac{^n d}{dt} \vec{a}$ Is the acceleration of a body in {n} [N]

$\frac{^b d}{dt} \vec{a}$ Is the acceleration of a body in {b} [N]

$\vec{\omega}_{b/n}$ Is the angular velocity of {b} in relation to {n} [N]

This relates acceleration within {b} to an acceleration in {n}.

2.1.2 Rotation between frames

As {b} is related to {n} through a position and orientation within {n}, vectors and points locally in {b} must be rotated accordingly when evaluated in {n}. The relationship between {b} and {n} can be described through a Rotation matrix. This rotation matrix comprises of three consecutive rotations to obtain the final rotation. For this project the z-y-x convention is used, meaning the coordinates are first rotated by ϕ around x_b then θ around y_b and finally by ψ around z_b

$$R_{x,\phi} = \begin{bmatrix} 1 & 0 & 0 \\ 0 & c\phi & -s\phi \\ 0 & s\phi & c\phi \end{bmatrix}, R_{y,\theta} = \begin{bmatrix} c\theta & 0 & s\theta \\ 0 & 1 & 0 \\ -s\theta & 0 & c\theta \end{bmatrix}, R_{z,\psi} = \begin{bmatrix} c\psi & -s\psi & 0 \\ s\psi & c\psi & 0 \\ 0 & 0 & 1 \end{bmatrix} \quad (2.5)$$

Equation 2.5 shows the rotation matrices used, where the sub-indices indicate around which axis the given rotation is performed. Furthermore for readability purposes, $\sin(\cdot)$ and $\cos(\cdot)$ is indicated by s and c respectively.

To rotate the velocity vector v^b to it's equivalent in $\{n\}$, the matrix R_b^n shown in Equation 2.6 is used.

$$R_b^n = R_{z,\psi} R_{y,\theta} R_{x,\phi} = \begin{bmatrix} c\theta c\psi & s\phi s\theta c\psi - c\phi s\psi & c\phi s\theta c\psi + s\phi s\psi \\ c\theta s\psi & s\phi s\theta s\psi + c\phi c\psi & c\phi s\theta s\psi - s\phi c\psi \\ -s\theta & s\phi c\theta & c\phi c\theta \end{bmatrix} \quad (2.6)$$

The velocity vector with respect to $\{n\}$ is then obtained by multiplying the velocity vector v^b with R_b^n as shown in Equation 2.7.

$$v^n = R_b^n v^b \quad (2.7)$$

The rotation from $\{n\}$ to $\{b\}$ is done by inverting R_b^n meaning.

$$R_b^{n-1} = R_n^b \quad (2.8)$$

Similarly the angular velocities can be expressed in different frames, through rotation, this matrix can be found to be:

$$T_b^n = T_n^{b-1} = \begin{bmatrix} 1 & \sin(\phi)\tan(\theta) & \cos(\phi)\tan(\theta) \\ 0 & \cos(\phi) & -\sin(\phi) \\ 0 & \frac{\sin(\phi)}{\cos(\theta)} & \frac{\cos(\phi)}{\cos(\theta)} \end{bmatrix} \quad (2.9)$$

An important property of this is the singularity located in $\theta = \pm 90^\circ$. The location of these singularity is assumed to be irrelevant, as the system would not reach this angle under normal operating circumstances.

The 6 DOF rotation matrix, to rotate the body fixed velocity vector ν to the inertial velocities $\dot{\eta}$ is then:

$$J_b^n = \begin{bmatrix} R_b^n & 0^{3x3} \\ 0^{3x3} & T_b^n \end{bmatrix} \quad (2.10)$$

2.2 System Description

For this project, a surface vessel is supplied by Aalborg University (AAU). The supplied platform is a Brig Falcon 360T [8]. Upon this the entire system is mounted, including actuators processing units sensors and user interfaces in addition to the operators.

Figure 2.3 shows an image of the platform.

Chapter 2. System Analysis



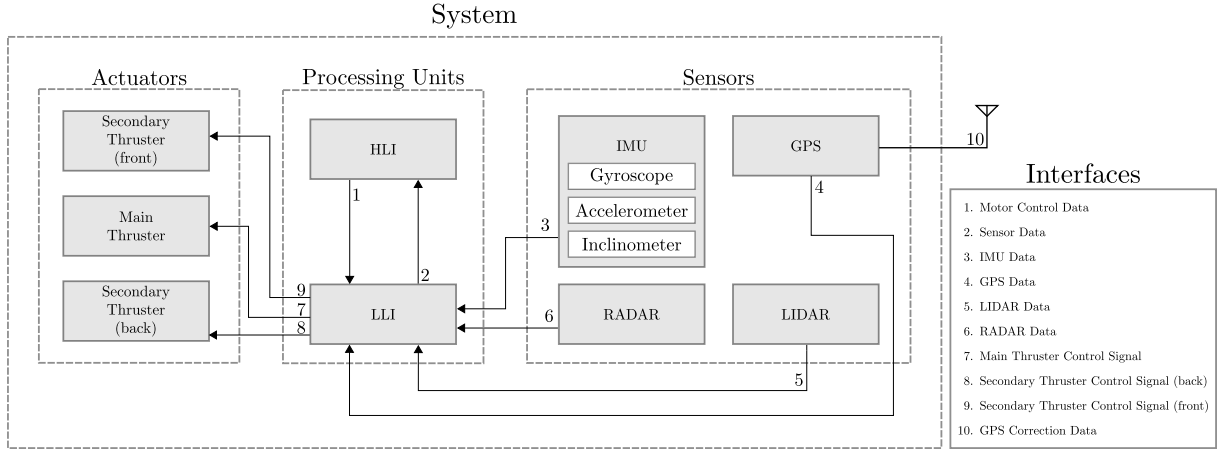
Figure 2.3: Project Platform

Following specs are available by the manufacturer[8]:

Length	350 cm
Width	175 cm
height	85 cm
Weight	225 kg
Max. Capacity	600 kg
Max. Passengers	5

As seen in table 2.2 the amount of passengers can vary from 1 to 5 persons. While the system is designed towards autonomously surveying of the Limfjord, it might find other practical uses, such as performing biological measurements. As a result of this, the payload of the vessel can be assumed to be in the range of 130kg(plus equipment)-600 kg.

This means a potential controller robust towards mass fluctuations, to ensure the stability of the system and security of the crew. The vessel is composed from several subsystems where an overview is seen in figure 2.4.

**Figure 2.4:** System overview of its interfaces

The system can be structured into three main parts, namely the sensors, processing units and actuation system. The processing unit is composed of Two parts, a High level interface (HLI) and a Low level interface (LLI). The High level interface (HLI) is a Intel NUC7i5BNK[nuc] (NUC) shown in Figure 2.5.

**Figure 2.5:** NUC 7i5BNK desktop computer

This is a desktop computer running ubuntu 16.1 LTS[9], with Robot Operating System (ROS) installed[10]. Is is responsible for analyzing and fusing sensor data, path planning, computing actuation output and more.

2.2.1 Robot Operating System

ROS is a software framework which can be used as a communication infrastructure between programs. ROS is a open source project licensed under creative commons v3.0.[11] In addition to a set of software libraries oriented at robotic software development, it provides a platform for developing a modular software structure. When running on a desktop computer, such as the NUC it allows programs running asynchronous on the computer to easily share information. This will be used as a basis for implementing the system on the HLI.

ROS works by structuring individual programs into nodes. A node can be a small python or c++ program which is compiled and linked as a ROS library. Each node is performs a task

Chapter 2. System Analysis

needed for the system, such as interfacing the sensors and runs in parallel with other potential nodes. A master node runs on top, manages the communication between each node, allowing them to share data. The nodes can be launched individually or clustered together into a launch script.

The communication between the nodes is done through topics. A topic is data stream accessible to the nodes. The data contained in a topic is defined by a message, which is a small predefined structure for what to share between each node. Each node can register as a Subscriber or Publisher to a specific topic allowing it to send and receive messages. Multiple nodes can Publish and be subscribed to the same topic, and messages will be stored in the buffer respective to that topic.

2.2.2 Actuation System

The actuation system available for the vessel is a 20 HP Honda diesel engine.

It is a stern engine mounted on the back of the hull and is capable of rotating horizontally to maneuver the vessel. From the measurements described in [Appendix C](#) it is capable of delivering 94N of thrust, and is capable of rotating $\pm 45^\circ$ for steering.

The engine is controlled by a helm to adjust the horizontal rotation, while the throttle is controlled by adjusting a lever. The position of the helm and the throttle is read electronically by a set of encoders which is sent to the HLI.

2.2.3 Sensors

The sensors located on the system is:

- Stim-300 IMU
- Trimble MB-Two Rtk-GPS

The sensors is mounted in a orange box which through a USB connection is connected to the HLI. Additionally Two GPS antennas is mounted on the vessel which is used by the GPS to measure position and orientation.

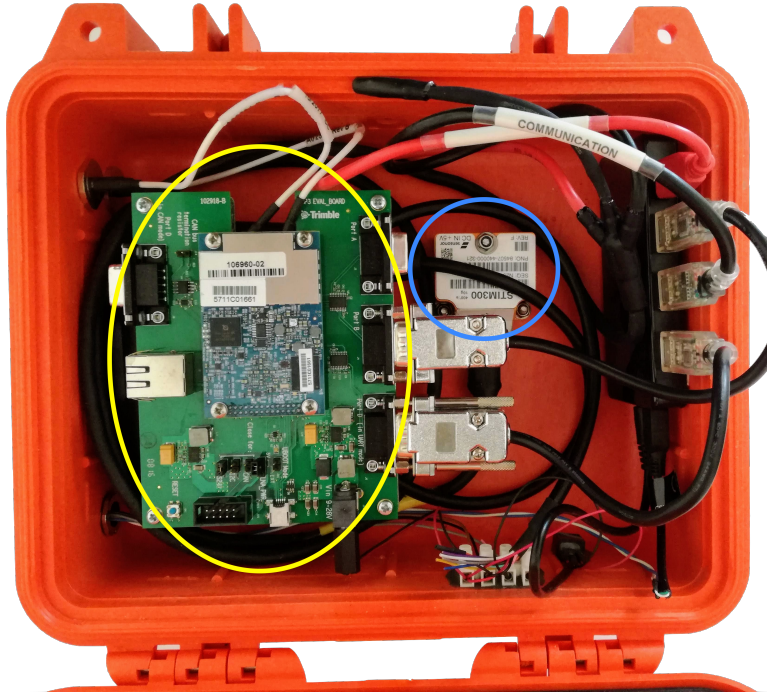


Figure 2.6: Box containing IMU and GPS

Figure 2.6 shows the sensor system used in this project, where the stim300 is shown within the blue circle, and the GPS shown within the yellow.

The vessel is equipped with a compartment beneath the passenger seat, where the box is placed, along with GPS antenna connectors and a power supply which provides power for the sensors and HLI.

2.2.4 IMU

The IMU supplied for this project is a stim-300, which is a Micro Electric Mechanical System (MEMS) sensor containing a 3-axis accelerometer, gyroscope and inclinometer[12].



Figure 2.7: Stim-300 IMU

Chapter 2. System Analysis

To define the characteristics of MEMS sensors, three different characteristics is used, namely Bias Instability, Angular/Velocity Random Walk and Rate/Acceleration Random Walk.

The Bias instability can be seen as a measure of how well a given sensor is able to perform. It describes the maximum noise reduction obtainable through integration. For a pure White Noise signal, this would be zero as integration time tends towards infinity assuming the input is kept constant. This is not the case for MEMS sensors as other noise contributions exists.

Angular/Velocity Random Walk is a measure of the error buildup over time caused by integrating the measurement noise. When a additive WGN source is integrated, it creates a zero mean "random walk", this is known as a Wiener process. This characteristic describes the uncorrelated high frequency measurement noise contribution added each measurement.

The Rate/Acceleration Random walk, also known as Bias Stability is a time dependent bias added to every measurement. This characteristics describes the noise contribution with a frequency much lower than that the measurement frequency, resulting in a slow varying bias added to every sample.

From the manufacturer the following specifications have been supplied. The sensors can provide sample rates up to 2000Hz with a 24-bit resolution. The gyro measures the angular velocities it experiences thus measuring $(\phi_b, \theta_b, \psi_b)$. The gyro have a range of $\pm 400^\circ \cdot s^{-1}$ with a resolution corresponding to $0.22^\circ \cdot s^{-1}$. The Gyro have an rated Angular walk of $0.15^\circ / \sqrt{h}$ and a bias instability of $0.5^\circ / h$.[12, p. 5] The sensor noise has been analyzed and verified in Appendix D to conform with the data supplied by the manufacturer.

The accelerometer is able to measure accelerations in (x_b, y_b, z_b) of $\pm 10g$ with a resolution of $1.9 \mu g$ with a velocity random walk of $0.06 m/s/\sqrt{h}$ and a bias instability of $0.05 mg$.[12, p. 6]

Similarly to the accelerometer, the inclinometer measures the accelerations it experiences. The difference is that an inclinometer is heavily low pass filtered. This results in it measuring the earths gravity represented by an acceleration in (x, y, z) . This vector representation an be transformed into (ψ_b, θ_b) . The inclinometer have a velocity random walk $0.08 m/s/\sqrt{g}$ and a bias instability of $0.06mg$.[12, p. 7] The inclinometer measures a heavily low-pass filtered 3-dimensional acceleration vector, which can be used to obtain ϕ and θ of the vessel.

$$\phi = \text{atan} \frac{I_y}{\sqrt{I_x^2 + I_z^2}} \quad (2.11)$$

$$\theta = \text{atan} \frac{I_x}{\sqrt{I_y^2 + I_z^2}} \quad (2.12)$$

Where:

$I_{\{x,y,z\}}$ Is the measured inclination vector [g]

Equation 2.11 and 2.12 can be used to obtain ϕ and θ of the vessel.

2.2.5 RTK GPS

The Trimble MB-Two is a RTK GPS, able to provide high precision GPS measurements. The manufacturer specifies the system to have a Horizontal Root Mean Square (HRMS) of $< 12mm$ - $8mm$ depending on fix type. This is reliant upon getting correction data from a stationary base station within a 10-40 km range of the system. [13, p.14]

The correction data obtained by the base station contains estimates of the disturbances caused by atmospheric changes, such as weather patterns etc. which is used by the GPS receiver (Rover) to improve it's measurements by assuming the disturbances is linked. Generally the precision of the GPS will gradually decline as the system moves further away from the base station, implying the correction data becomes less and less relevant. While the GPS sensor contains RTK capabilities, the system is currently not configured to obtain correction data, meaning this functionality is not utilized but expected to be so in the future.

The GPS measurements is received in the Wold Geodetic System (WGS84) coordinates, meaning the data is supplied in latitude and longitudinal coordinate system. While this system is convenient for positioning the system in the earth-fixed frame, it is inconvenient when evaluating the dynamics of the system.

The Swiss grid coordinates system is a more convenient representation for this. This representation utilizes meters north and east as opposed to the latitude longitude representation of WGS84. This enables the dynamic equations to be used in conjunction with the coordinate measurements directly.

To compute the WGS84 into distance distance between points the haversine equation is used [14].

$$\Delta_\lambda = \lambda_{st} - \lambda_n$$

$$\Delta_\varphi = \varphi_{st} - \varphi_n$$

$$a = \sin^2\left(\frac{\Delta_\lambda}{2}\right) + \cos(\varphi_{st}) \cdot \cos(\varphi_n) \cdot \sin^2\left(\frac{\Delta_\varphi}{2}\right) \quad (2.13)$$

$$c = 2 \cdot \text{atan2}(\sqrt{a}, \sqrt{1-a}) \quad (2.14)$$

$$d = R \cdot c \quad (2.15)$$

Where:

$\varphi\{st, n\}$ Is the latitudinal coordinate for the center of the system and [deg]
the measurement respectively

$\lambda\{st, n\}$ Is the longitudinal coordinate for the center of the system and [deg]
the measurement respectively

Δ_λ Is longitudinal difference between the two points [deg]

Δ_φ Is the latitudinal difference between the two points [deg]

R Is radius of the Earth [m]

The representation describes the measured position, relative to a fixed point denoted by $(\varphi_{st}, \lambda_{st})$ this can be chosen as a fixed reference point, such as position of the base station or simply the first measurement when the system is started.

2.2.6 Sensor Misalignment Compensation

When the sensors are mounted on the vessel, they're not expected to be perfectly aligned with the axis of $\{b\}$. Under the assumption that $\{b\}$ is centered at the center of buoyancy, it may not be practically possible to align the sensors axis with this exact spot.

This results in a situation where the dynamic equations are evaluated at the center of $\{b\}$ based on the measurements taken at another point in $\{b\}$. Under the assumption that C_g is stationary, this can be modeled as a stationary frame within $\{b\}$, denoted as $\{b_{imu}\}$ and $\{b_{GPS}\}$ respectively.

This effectively means that the measurements are taken in a different frame than they are evaluated in, meaning the measurements have to be rotated such that they align with $\{b\}$ before they can be used by the system. As the measurement box can be expected to be moved between operations, as well as C_g and C_b to change as equipment is moved, added or as personnel changes from time to time, the placement of said frame cannot be considered a constant.

While the magnitude and influence of the above mentioned changes can be discussed, the placement of the IMU relative to the orange box is expected to be constant, meaning if a misalignment of the box can be found, the system might be easier to align in the future by comparing the measured inclination relative to a fixed point on the vessel. This could potentially be done using a calibrated instrument.

The misalignment of the inclinometer is obtained in Appendix F to be:

$$b_{\phi,rad} = -0.0044 \text{ rad} \quad (2.16)$$

$$b_{\phi,rad} = -0.007 \text{ rad} \quad (2.17)$$

These two measurements can be used to compensate for the inclinometer, misalignment relative to the gravity vector, however this only describes the constant altitude bias, and does not contain information of position relative to the compass heading.

Gyroscope Misalignment compensation

The effect of the misalignment upon the gyroscope can be modeled as a misalignment error matrix multiplied with the real rotational velocity as shown in Equation 2.18.[15]

$$z_g = M_{gyro} \times \omega \quad (2.18)$$

$$\omega = M_{gyro}^{-1} \times z_g \quad (2.19)$$

Where:

z_g Is the angular rate measured by the gyroscope $[\frac{\text{rad}}{\text{s}}]$

ω	Is the angular rate as observed by $\{n\}$	$[\frac{\text{rad}}{\text{s}}]$
M_{gyro}	Is the misalignment error matrix for the gyroscope	

The misalignment matrix M models the rotation from $\{b\}$ to the measurement frame $\{b_{imu}\}$, meaning the inverse, M^{-1} models the rotation from $\{b_{imu}\}$ to $\{b\}$.

Accelerometer Misalignment Compensation

In addition to the angular misalignment sensor, the displacement from CG affects the measurements of the accelerometer. When the IMU is not placed at CG, the accelerometer experiences additional contributions in form of the coriolis effect. This leads to the following model describing the behavior of relating measurements observed in $\{b_{imu}\}$ to $\{b\}$:

$$a^m = M_{accel} \times (a^b + a^{cor}) \quad (2.20)$$

$$a^{cor} = \dot{\omega} \times r_b^m + \omega \times \omega \times r_b^m \quad (2.21)$$

Where:

M_{accel}	Is the misalignment error matrix for the accelerometer	
a^m	Is the acceleration measured by the gyroscope	$[\frac{\text{m}}{\text{s}^2}]$
a^b	Is the acceleration experienced at the center of $\{b\}$	$[\frac{\text{m}}{\text{s}^2}]$
a^{cor}	Acceleration caused by the coriolis force	$[\frac{\text{m}}{\text{s}^2}]$
r_b^m	Is the distance vector from $\{b\}$ to $\{b_{imu}\}$	[m]

As shown in Equation 3.13 the coriolis effect appears when rotating a body observed away from the center of rotation.

While the mentioned calibrations would be required to obtain the best possible measurements, constructing a method of obtaining these is deemed out of scope of this project, meaning that their impact is assumed negligible during this project, meaning $\{b_{imu}\} \approx \{b\}$ is assumed.

3 | Model Derivation

This Chapter Describes the model based on Fossen's Vectorial Model for marine craft[16]. Each force contribution will be derived and explained along with the underlying assumptions, and physical meanings. Eventually this leads into the model verification

Using the model presented by flossen, the system can be described as:

$$M\ddot{\nu}_r = -C_A(\nu_r)\nu_r - M_A\dot{\nu}_r - D(\nu_r)\nu_r + g(\eta) + \tau_{thrust} + \tau_{dist} \quad (3.1)$$

Where:

- M_{RB} Is the rigidbody mass matrix
- M_A Is the Added mass matrix
- C_A Is the Coriolis and centripetal force matrix
- $D(\nu_r)$ Is the dampening force matrix
- $g(\eta)$ Is the restoring forces
- τ_{thrust} Is the thrust supplied by the thrusters
- τ_{dist} Is the external forces acting upon the vessel.

This nonlinear model gives a full descriptions of the accelerations in {b}. The model is a combination of hydrostatic, hydrodynamic and rigidbody forces, all of which will be derives in the following sections.

3.1 Hydrodynamic Forces

The hydrodynamic forces are the forces occurring when a rigidbody moves relative to a liquid. The derivation of the hydrodynamic forces is based upon *Morrison's equation*, shown in Equation 3.2. This separates the hydrodynamic forces into two contributions, the added mass and the drag force.

$$F = \underbrace{\rho C_m V \dot{u}}_{\text{Added Mass}} + \underbrace{\frac{1}{2} \rho C_d A |u| u}_{\text{Drag force}} \quad (3.2)$$

The derivation of the Added masses is shown in subsection 3.1.1, while the basis for drag force is derived in subsection 3.1.2

3.1.1 Added Mass

The added mass can be seen as the inertia of the surrounding fluid. When the vessel moves through water, it have to move an amount of water equal to the space it is occupying in the water. The mass of said water, can be seen as an virtual mass added to the mass of the rigidbody. This results in a contribution, which acts as mass added upon the existing mass of the vessel, acting upon the axis of acceleration, which can be seen in Equation 3.2 as the acceleration dependent contribution. A derivation of the added mass is shown in subsection 3.1.1.

The total mass matrix of the system, is a simple summation of the rigidbody mass and the

Chapter 3. Model Derivation

added mass, such that:

$$M = M_{RB} + M_A \quad (3.3)$$

Where:

M_{RB} is the rigid body mass matrix

M_A is the added mass matrix

The Rigidbody mass matrix evaluated at center of gravity is expressed as:

$$M_{RB} = \begin{bmatrix} mI_{3x3} & 0_{3x3} \\ 0_{3x3} & I_g \end{bmatrix} \quad (3.4)$$

Where I_g is the inertia matrix defined as:

$$I_g = \begin{bmatrix} I_x & -I_{xy} & -I_{xz} \\ -I_{xy} & I_y & -I_{yz} \\ -I_{xz} & -I_{yz} & I_z \end{bmatrix} \quad (3.5)$$

and m is the total mass of the system including passengers. The fully parameterized added mass matrix, $M_A \in \mathbb{R}^{6x6}$ is defined as:

$$M_A \triangleq \begin{bmatrix} m_{xx} & m_{xy} & m_{xz} & m_{x\phi} & m_{x\theta} & m_{x\psi} \\ m_{yx} & m_{yy} & m_{yz} & m_{y\phi} & m_{y\theta} & m_{y\psi} \\ m_{zx} & m_{zy} & m_{zz} & m_{z\phi} & m_{z\theta} & m_{z\psi} \\ m_{\phi x} & m_{\phi y} & m_{\phi z} & I_{xx} & I_{xy} & I_{xz} \\ m_{\theta x} & m_{\theta y} & m_{\theta z} & I_{yx} & I_{yy} & I_{yz} \\ m_{\psi x} & m_{\psi y} & m_{\psi z} & I_{zx} & I_{zy} & I_{zz} \end{bmatrix} \quad (3.6)$$

This description contains 36 unknown parameters, which have to be determined for the system. This can be reduced by analyzing the vessels planes of symmetry. The vessel is through inspection said to have xz symmetry, which is the most common form of symmetry for surface vessels. [16, p. 178] This is based upon the observation that the vessel have symmetrical port and starboard. This results in the following parameter reduction of the added mass matrix:

$$M_A = \begin{bmatrix} m_{xx} & 0 & m_{xz} & 0 & m_{x\theta} & 0 \\ 0 & m_{yy} & 0 & m_{y\phi} & 0 & m_{y\psi} \\ m_{zx} & 0 & m_{zz} & 0 & m_{z\theta} & 0 \\ 0 & m_{\phi y} & 0 & I_{xx} & 0 & I_{xz} \\ m_{\theta x} & 0 & m_{\theta z} & 0 & I_{yy} & 0 \\ 0 & m_{\psi y} & 0 & I_{zx} & 0 & I_{zz} \end{bmatrix} \quad (3.7)$$

The Matrix shown in 3.7 shows the intended added mass matrix for the system, which contains 12 unique parameters, which have to be determined empirically. The off-diagonal elements are significantly smaller than the diagonal elements. Due to this and the impracticality of obtaining these, the system have been further reduced to only include the diagonal elements of the matrix , such that the final added mass matrix becomes:

$$M_A = \text{diag}\{m_{xx}, m_{yy}, m_{zz}, I_{xx}, I_{yy}, I_{zz}, \} \quad (3.8)$$

3.1.2 Drag Force

The velocity dependent contribution in Equation 3.2 is known as the drag force. Specifically the drag force is a collection of several terms, namely Potential dampening, skin friction, wave drift dampening and dampening due to vortex shredding. These forces have proven to be difficult to separate and is therefore collected into a single contribution for simplicity, shown in Equation 3.9. [16, p. 122]

$$D(\nu_r) = D + D_n(\nu_r) \quad (3.9)$$

This separates the forces into a linear and nonlinear contribution. The basis for this separation is founded in Boundary layer Theory. Drag appears when an object moves through a fluid, as the molecules previously occupying the area have to be distributed to the surroundings, creating a flow of particles away from the object. This creates a force acting opposite to the direction of travel, which is a complex combination of the shape and size of the object, viscosity and mass of the fluid and relative speed between the object and the fluid. [17]

Generally speaking when the vessel moves through the water, it experiences two types flow, laminar and turbulent.

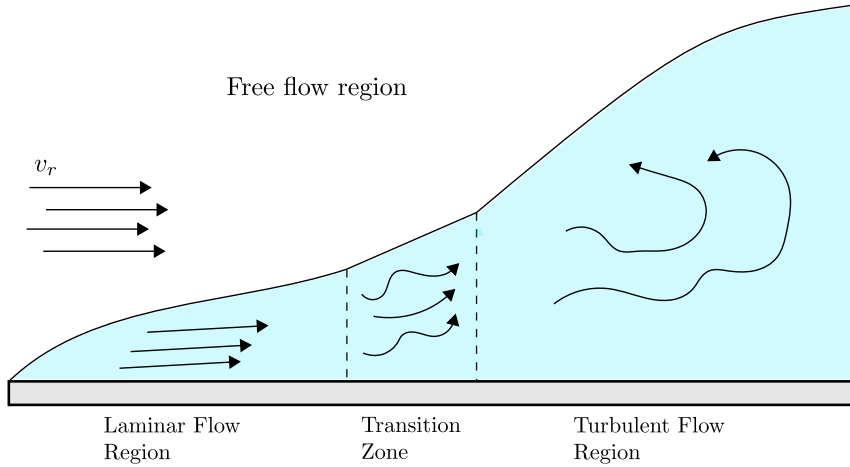


Figure 3.1: Illustration of laminar and turbulent flow regions

Figure 3.1 illustrates how the water flows when water hits a surface with a relative velocity v_r . The free flow region is the region of the water where the flow is unaffected by the surface, and will have little impact on the surface.

The laminar flow region is where the water flows in a orderly fashion, which results in a linear

Chapter 3. Model Derivation

relation between the drag and velocity.

In the turbulent flow region the water pressure becomes too high for the water flow to behave in an orderly fashion, resulting in vortices forming within this region. This results in a quadratic relationship between the speed and drag force meaning a nonlinear contribution. The distinction between these regions is determined by Reynolds number, the higher the more turbulent the flow is. Reynolds number is found by:[16, p. 122]

$$R_e = \frac{v \cdot D}{\nu} \quad (3.10)$$

Where:

v	Is the relative velocity of the water	[m]
D	Is the length of the surface	[m]
ν	Is the kinematic viscosity coefficient	

At low values of Reynolds number, the water flow is laminar, while high values indicate turbulent flow. As shown in Equation 3.10 Reynolds number increases with the velocity, meaning the size of the laminar and turbulent flow regions are a function of velocity. As a result of this Equation 3.9 is not a good description for the drag force at higher velocities, but can be seen as a description around point of interest. [16, p. 138] Due to the expected use case of the system, it is not assumed to experience large deviations in velocities, meaning this model is deemed acceptable.

Similarly to the added mass, determining the off diagonal elements of the drag matrix is impractical without access to advanced simulation software, meaning only the diagonal terms are considered, giving the following structure:

$$D = \{d_{L11}, d_{L22}, d_{L33}, d_{L44}, d_{L55}, d_{L66}\} \quad (3.11)$$

$$D_N(\nu) = \{d_{N11}|\dot{x}|, d_{N22}|\dot{y}|, d_{N33}|\dot{z}|, d_{N44}|\dot{\phi}|, d_{N55}|\dot{\theta}|, d_{N66}|\dot{\psi}|\} \quad (3.12)$$

Where:

d_{Lii}	is the linear drag coefficients
d_{Nii}	is the non linear drag coefficients

Obtaining the nonlinear diagonal elements requires a reliable method of obtaining different velocities isolated to that given axis. This is required as at higher velocities cross axis terms, such as the coriolis and centripetal effects influence the measurements meaning the drag is not isolated. As the use case of the system involves sailing in straight lines, the benefit of obtaining models for nonlinear drag in the other axis is considered to negligible. Therefore the only axis containing nonlinear drag coefficients is the x-axis, while the other coefficient is modeled as linear drag.

The drag coefficients have been found in Appendix B to be:

Axis	Coefficient
x_b	$D_x = 0.11, D_{nx} = 0.0005$
y_b	$D_y = 0.28$
z_b	$D_z = N/A$
ϕ	$D_\phi = 1.14$
θ	$D_\theta = 1.38$
ψ	$D_\psi = 0.27$

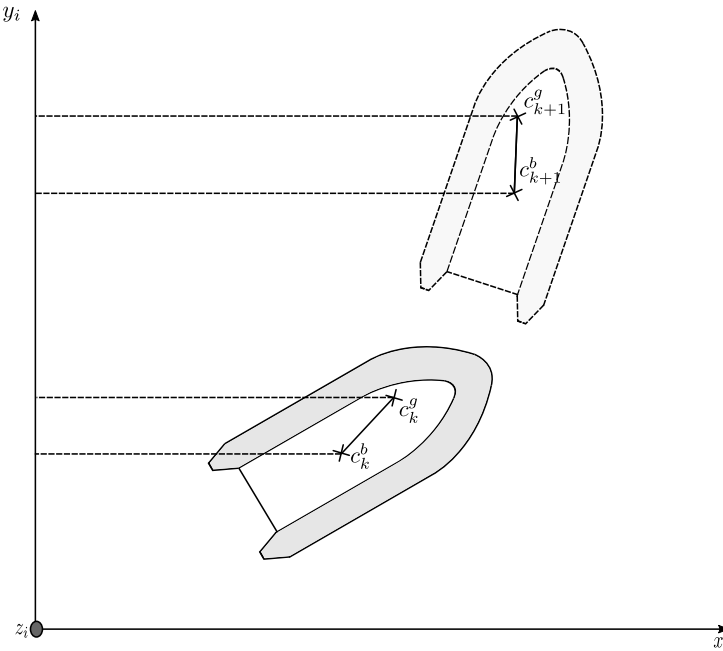
Table 3.1: Table of drag coefficients

As shown in Table 3.1 it have not been possible to obtain the coefficient for D_z , as it was not possible to oscillate that axis to a satisfying degree, meaning a more reliable method of obtaining this must be found.

3.2 Rigidbody Dynamics

3.2.1 Coriolis and Centripetal Matrix

The Coriolis and centripetal forces occurs when rotating $\{b\}$ within $\{n\}$. This force appears when the Newtonian forces are derived from a center of origin (c_o) that is not the center of gravity (c_g).

**Figure 3.2:** movement of c_g when rotating $\{b\}$ within $\{n\}$

Chapter 3. Model Derivation

When $\{b\}$ rotates relative to $\{n\}$ c_g rotates with it, under the assumption it maintains a constant distance to c_o . Figure 3.2 illustrates what causes this effect. When the vessel rotates, every point off-center moves in some direction, resulting in it having a velocity, increasing proportionally of the distance away from the center. The force resulting in accelerating the mass and inertia experienced at the center of gravity, meaning a off-center rotation must also account for the velocity experienced at c_g . This results in the movement of c_g being a combination of the translational and angular velocities of $\{b\}$, giving the nonlinear force matrix shown in equation 3.13.

$$C_a(\nu) = \begin{bmatrix} 0 & 0 & 0 & 0 & -m_z \dot{z} & m_y \dot{y} \\ 0 & 0 & 0 & m_z \dot{z} & 0 & -m_x \dot{x} \\ 0 & 0 & 0 & -m_y \dot{y} & m_x \dot{x} & 0 \\ 0 & -m_z \dot{z} & -m_y \dot{y} & 0 & -I_z \dot{\phi} & I_y \dot{\theta} \\ m_z \dot{z} & 0 & -m_x \dot{x} & I_z \dot{\psi} & 0 & -I_x \dot{\phi} \\ -m_y \dot{y} & m_x \dot{x} & 0 & I_y \dot{\theta} & I_x \dot{\phi} & 0 \end{bmatrix} \quad (3.13)$$

A derivation of the centripetal and coriolis force see Appendix G.

3.3 Hydrostatic Forces

The restoring forces are the forces acting upon the vessel by the displacement of the water it causes. These forces provide stability for the vessel, as they acts towards disturbances from the equilibrium point in heave, roll and pitch. The stability of the vessel depends on the placement of the meta center in relation to the center of gravity. As long as the vessel does not rotate past a certain boundary this will provide an asymptotically stable equilibrium point.

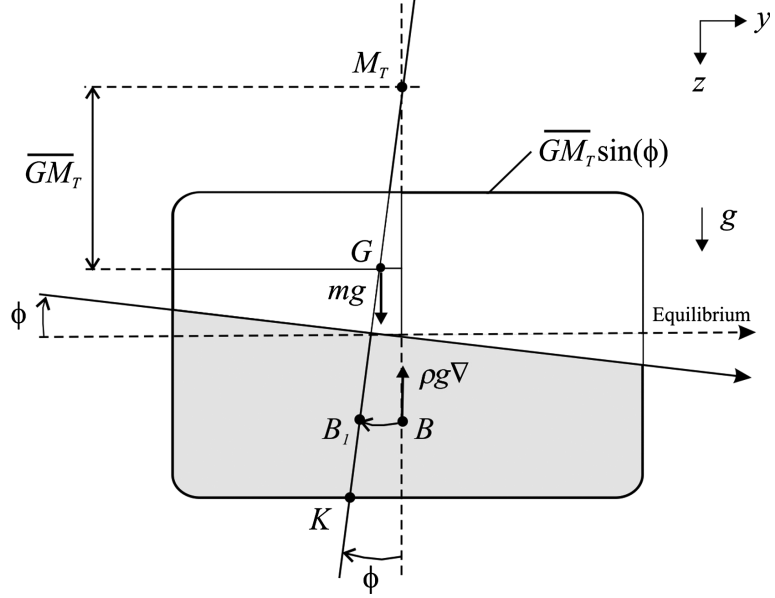


Figure 3.3: illustration of metacentric height

Figure 3.3 illustrates the transverse metacentric stability. The metacenter is the point where a line from c_b at equilibrium intersects the line c_b with a displacement ϕ or θ for the transverse or longitudinal metacenter respectively. The metacenter is used to determine the metacentric stability of the vessel. The larger the metacentric height, the more stable the vessel becomes.[16, p. 67] Additionally the metacentric heights determines the magnitude of the restoring torques. The metacentric heights can be found to have following relationship:

$$\overline{GM}_T := \overline{BM}_T - \overline{BG} \quad (3.14)$$

$$\overline{GM}_L := \overline{BM}_L - \overline{BG} \quad (3.15)$$

where:

$$\overline{BM}_T := \frac{I_T}{\Delta} \quad (3.16)$$

$$\overline{BM}_L := \frac{I_L}{\Delta} \quad (3.17)$$

where I_T and I_L can be determined by their upper bound:[16, p. 66]

$$I_L < \frac{1}{12} L^3 B = 75.03 \quad (3.18)$$

$$I_T < \frac{1}{12} B^3 L = 18.76 \quad (3.19)$$

Where:

B Is the width of the vessel [m]

L Is the length of the vessel [m]

Chapter 3. Model Derivation

$$\Delta \quad \text{Is the nominally displaced water volume} \quad [\text{m}^3]$$

Based on Archimedes principle, the water displaced by the vessel results in an upwards force equal to the volume of displaced water times the gravitational constant. Formally, this is expressed as:

$$F_{disp} = V\rho g \quad (3.20)$$

Where:

F_{disp}	Is the upwards force acted upon the vessel caused by the displaced water	[N]
V	Is the volume caused by the displaced water	$[\text{m}^3]$
ρ	is the density of the water	$[\text{kg}/\text{m}^3]$
g	Is the gravitational constant	$[\text{m}/\text{s}^2]$

This force is in relation to the earth-fixed frame, meaning the vessel's orientation determines how these forces are translated to the body-frame. Taking orientation of the vessel into account the buoyancy force results in the following vector in the body frame:

$$F_{boy} = F_{disp} \cdot \begin{bmatrix} -\sin \theta \\ \cos \theta \sin \phi \\ \cos \theta \cos \phi \end{bmatrix} \quad (3.21)$$

In addition to restoring forces, the buoyancy force also delivers restoring torques. This results in the following torque equations:

$$\tau_{boy} = F_{disp} \cdot \begin{bmatrix} G\bar{M}_t \sin \phi \cos \theta \cos \phi \\ G\bar{M}_l \sin \theta \cos \theta \cos \phi \\ (-G\bar{M}_t \cos \theta + G\bar{M}_l) \sin \phi \sin \theta \end{bmatrix} \quad (3.22)$$

The final expression for the buoyancy force then becomes:

$$g(\eta) = \begin{bmatrix} F_{boy} \\ \tau_{boy} \end{bmatrix} \quad (3.23)$$

This representation of the buoyancy force raises some sensitivity concerns. By approximating the vessel to be roughly box shaped, the sensitivity for the vessel in z_n can be found to be:

$$S_z \approx L * W * \rho * 10^{-3} = 61.87 \frac{N}{m \cdot 10^{-3}} \quad (3.24)$$

As a result, a small noise on z_n will lead to a large noise in the buoyancy force, as the error in z_n is multiplied. Additionally to compute the buoyancy force, the sea level must be known. This will be a time varying parameter, due to tides, and small deviations between the known and actual sea level will lead to a large error in the computed buoyancy force. While sea-level measurements are available for the limfjord, [18] the sensitivity towards errors is so high that this method is not feasible to use in p. A better approach might be to estimate the buoyancy force directly, using the dynamics of the system. This approach removes the multiplicative dependency of z_n such that the noise wont be multiplied. Additionally by estimating the buoyancy force directly, the system does not require knowledge of the sea-level.

3.4 Actuation Model

The Thruster is located at the back of the vessel, and maneuvering is done by manipulating the angle of the thruster with respect to the vessel. This results in Force contributions in x_b and y_b and torque contributions in the three rotational axis $\tau_\phi, \tau_\theta, \tau_\psi$.

$$F = \begin{bmatrix} F_x \\ F_y \\ F_z \end{bmatrix} = \begin{bmatrix} f \cdot \cos \alpha \\ f \cdot \sin \alpha \\ 0 \end{bmatrix} \quad (3.25)$$

Where:

f is the thrust produced by the propeller

α is the angle of the propeller

The torque contributions is found by multiplying the forces upon the moments of the vessel. This results in the following equation:

$$\tau = \begin{bmatrix} \tau_\phi \\ \tau_\theta \\ \tau_\psi \end{bmatrix} = \begin{bmatrix} F_z l_y - F_y l_z \\ F_x l_z - F_z l_x \\ F_y l_x - F_x l_y \end{bmatrix} = \begin{bmatrix} -F_y l_z \\ F_x l_z \\ F_y l_x - F_x l_y \end{bmatrix} \quad (3.26)$$

Where:

$l_{x,y,z}$ denotes the length from the force vector to the center of gravity in the respective axis.

External Disturbances In addition to modeling the physical behavior of the system, a disturbance model is needed. The disturbances model can be seen as a combination of two factors, the measurement noise and the external forces. These disturbances are assumed to be stochastic by nature, meaning they are a collection of random variables.

The Forces will not be included into the model directly, but will be applied in the simulation to test the robustness of the controller towards the described disturbances. The external forces are a combination of the different forces acting upon the system. These have been further split into the constant disturbance and the wave disturbances. The constant forces are caused by the difference of speed between the water and the vessel. By assuming the effect of the wind to be negligible this effect can be simulated by subtracting the velocity of the water from the vessel,

Chapter 3. Model Derivation

to get the relative velocity ν_r of the vessel through the water such that.

$$\nu_r = \nu - \nu_{dist} \quad (3.27)$$

Where:

- | | |
|--------------|---|
| ν_r | Is the relative speed of the vessel through the water |
| ν | Is the speed of the system in the $\{n\}$ frame |
| ν_{dist} | Is the speed of the water |

By using ν_r instead of ν in the dynamic equation, it is easily seen that the drag the system experiences changes. The intuition behind this is comes from the drag forces which are caused by friction between the vessel and the water. This results in a force which is not dependent on the speed in $\{n\}$ but speed through the water.

Similar to the constant forces the wave disturbances have to be estimated through the states. This kind of disturbance is assumed to be zero summing, meaning an integrator wont work as well as on the constant forces. The wave disturbances are modeled as a sinusoidal torque added onto the system with randomized frequency amplitude, and direction.

3.5 Sensor Noise

The measurement noise does not represent a force added upon the vessel, but rather a misrepresentation of the states of the vessel. Every sensor is considered subject to measurement noise, however the type and magnitude differs between the type of sensor implemented.

3.5.1 MEMS sensor model

3.5.2 Accelerometer Model

As stated in subsection 2.2.4, the IMU is subject different noise terms. The origin of these terms can be found by studying the basic concept behind the sensors, even though the specific design may vary slightly from the stim300.

The basic principle behind a MEMS-based accelerometer works by suspending a mass by springs, allowing the mass to move in one direction, an illustration of this is shown in Figure 3.4. When the mass experiences an acceleration in that direction, this will translate into a displacement of the mass opposite to the acceleration.

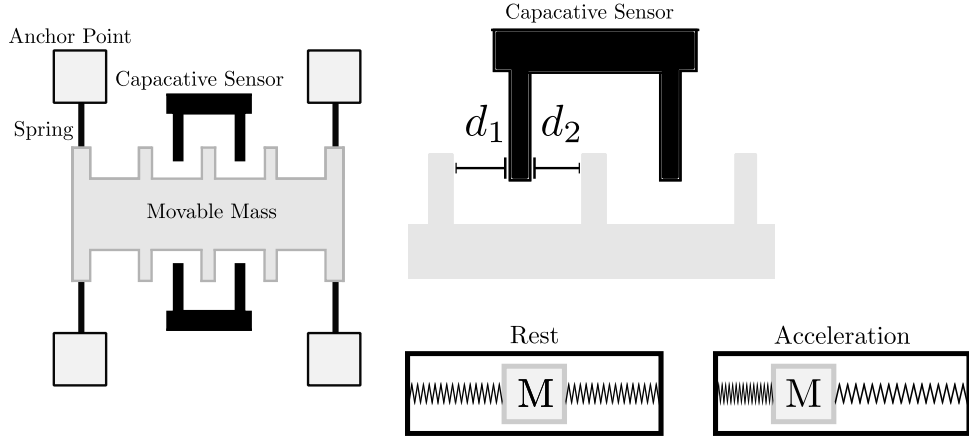


Figure 3.4: Mechanical principle behind MEMS accelerometer

By comparing the position of the mass when at rest to when it experiences an acceleration, the acceleration can be found. Practically this displacement can be measured using capacitive sensors, which is placed such that they measure the displacement along the desired axis. A 3-axis accelerometer is archived by placing a accelerometer facing each axis, however some designs allow the measurement of multiple axes at once.

The accelerometer have no internal way of separating the acceleration induced by gravity from the acceleration induced by other sources acting on the system.

$$a_b = a_{IMU} R_n^b \ a_g \quad (3.28)$$

Where:

a_b Is the acceleration measured in $\{b\}$ [g]

a_{IMU} Is the acceleration measured by the IMU [g]

g is the gravitational vector defined as $[0 \ 0 \ 9.81]^T$ [g]

3.5.3 Gyroscope Model

A MEMS based gyroscope is able to measure the angular velocities through the coriolis force. The coriolis force is described in further detail in section 3.2.1 and G , describes the movement of an object rotating relative to an inertial frame. Generally it can be found to be:

$$\vec{c} \sim \vec{\Omega} \times \vec{v} \quad (3.29)$$

Where:

\vec{c} Is the coriolis force vector [N]

Chapter 3. Model Derivation

$\vec{\Omega}$	Is angular rate vector	[rad/s]
\vec{v}	Is the velocity vector	[m/s]

By keeping a mass at a constant velocity, and measuring the resulting coriolis force, the angular rate is found.

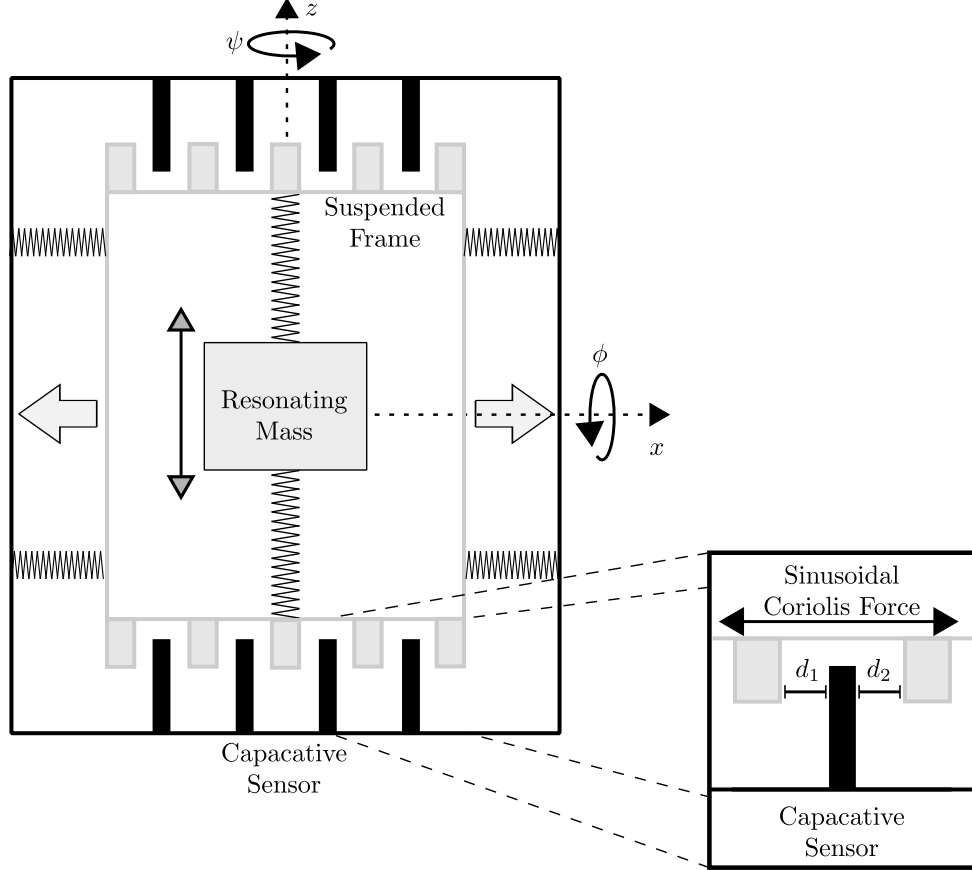


Figure 3.5: Mechanical principle behind MEMS Gyroscope

This is archived by vibrating a mass at a linear constant velocity suspended on a frame. The frame containing the mass is the further suspended via springs to a casing. The displacement of the frame relative to the casing is then measured in a similar fashion to the accelerometer. An Angular rate induced on an axis will result in a sinusoidal coriolis force on the perpendicular axes.

During operation, the temperature of the sensors tend to fluctuate due to electronic induced heat and mechanical friction. This causes changes in in the properties of the capacitative sensors which causes the measurement of the displacement to develop a bias. The bias of the gyroscope is furthermore effected by the vibratory stability of the resonating mass. If the vibratory velocity of the resonating mass changes, so does the coriolis force induced b rotation resulting in a increased bias.

As established, while it is often convenient to assume the noise is white Gaussian noise (WGN), this assumption does not always hold. MEMS sensors, is subject lower frequency noise terms in addition to the high frequency additive Gaussian noise terms usually associated with measurement noise. A common way of modeling the lower frequency noise terms is as a Random walk process, also known as a wiener process. A wiener process is archived by integrating a WGN source, which results in a zero mean process which slowly drifts around zero. While this description is a basic approach which does not bound the bias, it have been found to be a good description in most cases. This results in the following model for the gyroscope sensor noise:

$$\omega_{meas}(t) = \omega_{true}(t) + b(t) + w(t) \quad (3.30)$$

Where:

- $\omega_{meas}(t)$ Is the measured angular velocity at time t
- $\omega_{true}(t)$ Is the true angular velocity at time t
- $b(t)$ Is Measurement bias as time t
- $w(t)$ Is Measurement noise as time t

In Appendix E the measurement noise of the gyroscope have been verified to be approximately white and normally distributed. The measurement noise is modeled as a Additive White Gaussian Noise (AWGN) term, described by covariances specified by $\sigma_{w,\{\phi,\theta,\psi\}}$.

The bias term is a combination of stationary, mechanical errors and time varying processes. While the stationary bias terms can be calibrated offline, the time varying processes must be estimated online. To do so, the time dependent bias drift is modeled as a Wiener process, such that:

$$\begin{aligned} b_{\{\phi,\theta,\psi\}}(0) &= 0 \\ \dot{b}_{\{\phi,\theta,\psi\}}(t) &= b(t) + w(t) \end{aligned} \quad (3.31)$$

The zero mean assumption only holds if the constant biases are considered negligible or otherwise accounted for prior to estimation. The described model of a gyroscope have previously shown to be a good model of a MEMS-based gyroscope.[19][20]

3.5.4 Inclinometer Model

The gravitational vector measured by the Inclinometer is a result of low pass filtering the accelerations. The low pass filtering can be done by electronic or mechanical means, or a combination thereof, and filters cuts off the higher frequency effects, such as external disturbances and some dynamic terms. Equation 3.32 show the sensor model of the inclinometer.

$$z^{\{\phi,\theta\}} = L(t)\Theta(t)^{\{\phi,\theta\}} + w(t) \quad (3.32)$$

Where:

- $z^{\{\phi,\theta\}}(t)$ Is the measured ϕ and θ respectively at time t [rad]

Chapter 3. Model Derivation

$L(t)$	Is a equivalent low-pass filter	
$\Theta^{\{\phi,\theta\}}(t)$	Is the attitude of the sensor with respect to $\{n\}$ at time t	[rad]
$w(t)$	Is measurement noise at time t	[rad]

While some of the dynamics might momentarily introduce a disturbance to the measurements, such as then the vessel is changing speeds, the effect of this is assumed to be negligible.

A side effect of the filtering is that it introduces a time constant into the measurement. This means the sensor needs time to converge to changes in attitude of the system. As the relevant axis is known to have oscillatory behavior, caused by the mass-damper effect of the hydro dynamic forces, these oscillations might be higher than the cut-off frequency of the low pass filter. This introduces a uncertainty term as the THU of the system is shown to be sensitive to deviations in the attitude.

Another side effect is the filtering effect is that the noise becomes correlated, as the time constant of the sensor is much lower than the sample time. This means the noise is not AWGN as shown in Appendix E.

4 | Sensor Fusion Design

4.1 Sensor Fusion

In order to reduce the measurement noise, sensor fusion is utilized. Essentially sensor fusion is the process of utilizing measurements from different sensors such that it improves the overall precision of the measurements.

A verity of different techniques exists for this purpose, such as the Madgwick[21], Mahony[22] and the kalman filters[23]. The first two approach is types of complementary filters, which uses different noise characteristics of different sensors to reduce the noise of the measurements.[21] A simple complementary approach is presented in subsection 4.1.1.

The kalman filter is a linear quadratic estimator, which relies on Bayesian theory for noise reduction. This is a widely used technique, which relies on a deterministic model, which improves performance at the cost of computational complexity. The classical kalman filter relies on a linear model, however it is possible to extend this to also include nonlinear parameters, this is known as the extended kalman filter (EKF).[23]

4.1.1 Complementary Filter

The theory behind a complementary filter is to combine measurements of the same state, with different noise characteristics, to improve the overall performance.

A often used approach is to combine the high frequency characteristics of a gyroscope and combining it with the low frequency characteristics of a accelerometer to find the attitude. Where the accelerometer could be replaced by an inclinometer, due to their similarities.

By comparing the two sensor models, the basis for this can be found.

$$z_i = L(\Theta) + \mu_i \quad (4.1)$$

$$z_g = \dot{\Theta} + \mu_g + b_k \quad (4.2)$$

Where:

Θ Is angle of the sensor with respect to $\{n\}$ [rad]

$L(\cdot)$ Is a low pass filter

z_i Is the measurement supplied by the inclinometer [rad]

μ_i Is the AWGN experienced by the inclinometer at time of measurement [rad]

z_g Is the measurement supplied by the gyroscope [rad/s]

μ_g Is the AWGN experienced by the gyroscope at time of measurement [rad]

b_k Is the bias of the gyroscope at time k [rad/s]

The low pass filter in Equation 4.1 modeling the low pass characteristics of the inclinometer,

meaning $L(s) \approx 1$ when the inclinometer data is relevant. This filters away fast changes to the state, meaning it becomes noisy at rates of change. This results in a signal with low noise for lower frequencies, but with a relatively large time constant, making it unreliable at higher frequencies.

In contrast the gyroscope works best for shorter intervals by integrating the rate measurements to estimate attitude. The wiener process generated when integrating the noise of the gyroscope measurement in conjunction with the bias makes the angle drift increase with integration times. This makes the angle estimated from the gyroscope drift with time, giving unreliable readings for larger intervals.

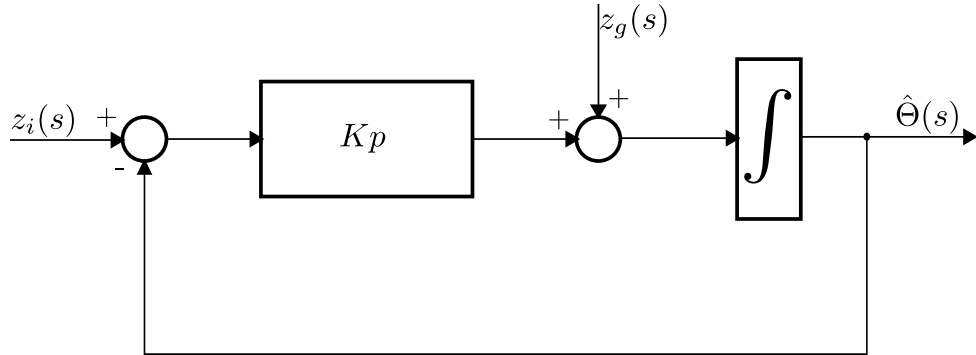


Figure 4.1: Classical Complementary filter

A example of a classical complementary filter is shown in Figure 4.1. The filter works by applying a low pass filter to the accelerometer estimate of the attitude wile applying a high pass filter to a integrated gyroscope output with the same cutoff frequency the beneficial properties of each sensor is utilized. Specifically this is shown in Equation 4.3 with Equation 4.4 and Equation 4.5 being the filter coefficients.

$$\hat{\Theta}(s) = F_1(s)z_i(s) + F_2\frac{z_g(s)}{s} \quad (4.3)$$

$$F_1 = \frac{kp}{kp + s} \quad (4.4)$$

$$F_2 = \frac{s}{kp + s} \quad (4.5)$$

The crossover frequency for both filters is determined by kp , such that the high pass filter of the gyroscope data and low pass filter shares cutoff frequency shown by $F_1 + F_2 = 1$. Using this knowledge Equation 4.3 can be simplified to.

$$\hat{\Theta}(s) = F(s)z_i(s) + (1 - F(s))\frac{z_g(s)}{s} \quad (4.6)$$

The shared cutoff frequency is chosen a trade off between minimizing the impact of the slow dynamics of the inclinometer and the low frequency noise contributions of the gyroscope. The

discrete time realization of Equation 4.6 is found to be:

$$\hat{\Theta}_k = \alpha(\hat{\Theta}_{k-1} + z_{g,k} \cdot Ts) + (1 - \alpha)z_{i,k} \quad (4.7)$$

$$\alpha = \frac{kp}{Ts + kp} \quad (4.8)$$

By observing Equation 4.7 it can be see that the estimate of the angle, $\hat{\Theta} \rightarrow z_i$, as $z_g \rightarrow 0$.

Even with more complex implementations of a complementary filter, such as the before mentioned Mahony and Madgwick filters, this approach is shown to be comparatively light regarding computational requirements, meaning it's a good solution for implementations with such constraints.

4.1.2 Extended Kalman Filter

The extended Kalman filter is an generalization of the kalman to include nonlinear systems. During this, the filter looses it's guaranteed optimally, as the system is no longer linear. The generalization is archived by linearizing the state propagation and measurement matrices along the predicted trajectory, which is repeated for each iteration.[23]

The linearization is archived through partial derivation of the state matrices, resulting in the following set of equations:

$$F_{k-1} = \left. \frac{\partial f(x)}{\partial x} \right|_{x=\hat{x}_{k-1|k-1}} \quad (4.9)$$

$$H_k = \left. \frac{\partial h(x)}{\partial x} \right|_{x=\hat{x}_{k-1|k-1}} \quad (4.10)$$

As the linearization have to be done online, this comes with increased computational complexity.

This linearization can be simplified under the assumption that the system does not change during operation, the meaning derivative only changes with the prediction and not time.

Similar to the Kalman filter, the algorithm consists of the following 3 steps: initialization, prediction and update.

The initialization step will only be run once, and is used to initializes the state and state covariance to their initial values.

The Prediction step, predicts the next measurement based upon available information at time k-1. This results in the following set of equations:

$$\hat{x}_{k|k-1} = f(\hat{x}_{k-1|k-1}) + B(x)u_{k-1} \quad (4.11)$$

$$P_{k|k-1} = F_{k-1}P_{k-1|k-1}F_{k-1}^T + Q_{k-1} \quad (4.12)$$

Where:

Q_{k-1} Is the process noise covariance matrix

F_{k-1} Is the linearized propagation matrix shown in Equation 4.9

The update step corrects the predictions based upon measurements received at time k. Equation 4.11 predicts the state at time k, given the state vector and input vector at time k-1. Similarly to the state vector, the covariance matrix is predicted using Equation 4.12.

The Update step is as follows:

$$\tilde{y}_k = z_k - h(\hat{x}_{k|k-1}) \quad (4.13)$$

$$S_k = H_k P_{k|k-1} H_k^T + R_k \quad (4.14)$$

$$K_k = P_{k|k-1} H_k^T S_k^{-1} \quad (4.15)$$

$$\hat{x}_{k|k} = \hat{x}_{k|k-1} + K_k \tilde{y}_k \quad (4.16)$$

$$P_{k|k} = (I - K_k H_k) P_{k|k-1} \quad (4.17)$$

Where:

H_k Is the linearized measurement matrix shown in Equation 4.10

The kalman gain shown in Equation 4.15 is used to improve the state and covariance prediction based on the measurement z_k . When the update step is completed, the time is updated and a new prediction is made.

The measurement residual shown in Equation 4.13 is an expression of the difference between the measured and predicted output. When verifying the filter, this can be used to check for biases and ensure the output is White Gaussian. If the measurement residuals is not WGN, this could be a indication of modeling errors, either of the dynamic system or of the sensors.

As shown the kalman filter is capable of utilizing a dynamic model when proper gating the state vector to next time step. While this is known to be a computational expensive procedure, especially as the number of states increases, it generally considered to perform better than the complementary filters.

4.2 System Design

Due to the availability of computational resources and high demand for precise measurements, the kalman filter is chosen as the best solution.

Some approaches such as [24] shows the performance of the kalman filter can be improved by utilizing a complementary filter in conjunction with the EKF, to provide better attitude measurements. The original approach fuses magnetometer and gyroscopic measurements to reduce the measurement noise and reduce the impact of the low pass filter effect of the inclinometer. While this problem needs further investigation, a kalman filter approach to the above is explored in sec:colnoise.

Chapter 4. Sensor Fusion Design

The IMU is capable of delivering measurements of up to 2000Hz, while the GPS delivers a sample with a rate of 5Hz. As a 2kHz update of the system is deemed excessive, it have been chosen to downsample the IMU measurements to 200Hz. As a results, the filter will receive 40 IMU measurements between each GPS sample, which needs compensation as this means the filter will use outdated GPS otherwise.

Between the GPS measurements the states are estimated through dead reckoning, and recalibrated for each measurement. Additionally this structure allows the system to keep estimating the velocity and position in the case of a GPS outage.

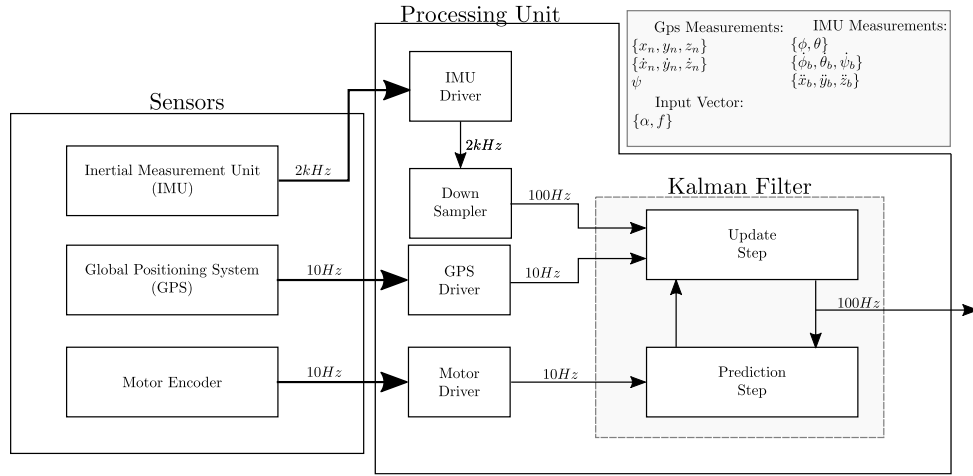


Figure 4.2: System Overview

Figure 4.2 shows the system design. In addition to the mentioned sensor fusion a driver for the sensors and actuator is developed, allowing the HLI and exterior to interface. The IMU driver reads the data from the datagram specified in the manual and converts the inclinometer data to a angle in roll and pitch. The $2kHz$ data is then feed into a filter, which downsamples the data to $200Hz$ and passes it further to the Kalman Filter. The down sampling process includes averaging the data over the last 10 samples to reduce noise. This have been found in app:white and Appendix D to reduce the noise of the data while still keeping it WGN.

The GPS driver reads the NMEA string and heading messages which is passed along to the kalman filter. The NMEA string contains data about validity of the data and fix type, which is also used by the filter, to compensate for a potential GPS outage.

The Motor encoder sends the rudder and thruster values, which represents the u vector of the system.

As described in subsection 3.5.1 the gyroscopes in particular experiences sensor bias during operation, which must be handled by the filter, to improve performance. Specifically this is done by utilizing the measurement model to estimate the biases experienced by the gyroscope during operation. This method extends the states of the system with a bias state for each axis of the gyroscope and will be described in further detail in section 5.4.

4.2.1 Dead Reckoning

Dead reckoning is the process of estimating a position of the vessel using inertial measurements. The process works by estimating the velocity, position and attitude and propagating forward from a known point. This can either be done using a complementary filter such as [25] or using an EKF among other methods.

The estimation is done by relying on integrated accelerometer and gyroscopes data, and thereby also the sensor noises. As a result of this is the estimation errors expected to drift over time, giving increasingly unreliable results. Even for low noise sensors such as the STIM300, this have shown to provide error ranges of $3.981m$ after 1 min. of dead reckoning increasing up to $102.36m$ after 10 min.[25, p. 144]

From this it can be seen that while dead reckoning could allow the system to navigate over shorter times, it should not be relied upon for extended use, as the system start to deviate significantly over longer times. Additionally it shows the importance of receiving GPS measurements when performing hydrographic measurements as even short during short intervals of GPS provides unusable results.

4.3 Implementation

The system is implemented on the MCU, which interfaces with the system. The implementation is done using ROS, where each module runs as a separate node, utilizing topics to send data independently between each other.

The system consists of 2 general functionalities; Hardware interfacing and sensor fusion. The nodes responsible for hardware interface is:

- IMU Initialization (*imu_init_node*)
- IMU Driver (*imu_driver_node*)
- GPS Driver (*gps_driver_node*)
- Thrust Encoder (*thrust_node*)
- Angle Encoder (*angle_node*)

The IMU Initialization node, *imu_init_node*, is run when the system is initialized. Its purpose is the set the correct flags in the IMU, such that it have the correct sample rate, internal filter settings. When the IMU is initialized, the *imu_driver_node* is called, which reads the data sent from the IMU, and calculates roll and pitch from the inclinometer data. The data is then averaged and downsampled to $200Hz$ which is published on the topic `\imu_data`.

The *gps_driver_node* is responsible for reading the NMEA data and publishing it on `\gps_data` topic.

Chapter 4. Sensor Fusion Design

The *thrust_node* and the *angle_node* reads data from the motor encoders and publishes them in \thrust and \angle topics.

5 | Kalman Filter Design

This chapter will present the different techniques used to design and improve the performance of the sensor fusion system. This will lead into a presentation of its simulated performance and eventual evaluation thereof.

5.1 Discretization

The discrete system model is based on the continuous time model derived in chapter 3, and will be used to propagate the state vector upon the next time step. The discrete time model is of the form:

$$x_k = f(x_{k-1}, u_{k-1}) \quad (5.1)$$

$$f(x, u) = A(x) + b(\alpha)u \quad (5.2)$$

Where:

- x_k Is the state vector at time k
- u_{k-1} Is the input vector at time k-1
- $A(x)$ Is the state propagation matrix
- $b(\alpha)$ Is the input propagation matrix
- α Is the orientation of the stern engine

The discretized dynamic model shown in Equation 5.1 relates the state vector, x_{k-1} and u_{k-1} to a propagated state vector. With the state vector, x_k and input vector, u_k being:

$$x_k = \begin{bmatrix} \eta & \nu & \dot{\nu} \end{bmatrix}^t \quad (5.3)$$

$$u_k = f \quad (5.4)$$

The state vector describes the position in $\{n\}$ where the velocities and accelerations is described in $\{b\}$. The design of this state vector is derived from the dynamic equations, and is chosen such that it describes the dynamics relative to $\{b\}$. The actuation model describes the relationship with the input vector u and the induced forces upon the system. The resulting accelerations is

Chapter 5. Kalman Filter Design

induced on $\{b\}$ given input vector u , and is shaped by orientation α to become:

$$b(\alpha) = \begin{bmatrix} 0^9 \\ \frac{\cos(\alpha)}{mx} \\ \frac{\sin(\alpha)}{my} \\ 0 \\ \frac{-lz \cdot \sin(\alpha)}{Ix} \\ \frac{lz \cdot \cos(\alpha)}{Iy} \\ \frac{lx \cdot \sin(\alpha)}{Iz} \end{bmatrix} \quad (5.5)$$

The system have been discretized through forward eulers method, with a sample rate of $Ts = 200Hz$, which is deemed a fitting compromise between resolution and computational requirements.

The state propagation matrix shown in Equation 5.6 is based on the presented state vector.

$$A(x) = \begin{bmatrix} I^{6x6} & J \cdot Ts & 0^{6x6} \\ 0^{6x6} & I^{6x6} & Ts \cdot I^{6x6} \\ G & D(\nu) & 0^{6x6} \end{bmatrix} \quad (5.6)$$

$$J = \begin{bmatrix} R_b^n & 0 \\ 0 & T_b^n \end{bmatrix} \quad (5.7)$$

As shown, J , is the nonlinear rotation matrices, rotating the body fixed velocities to n before being discretized by Forward Euler.

As shown in Equation 5.6 it have been chosen to omit the coriolis effect. The reason for this impact of the coriolis force is considered negligible, as it is dependent on the angular velocities, which given it's use case is not experienced much to a large extent.

The drag matrix contains the drag coefficients for each axis of the vessel. As explained in subsection 3.1.2, these coefficients are a combination of laminar and turbulent flow experienced by the body.

From prior knowledge it have been found that the nonlinear contribution starts to become significant at around $2m/s$.[16] Due to this, it have been chosen only model d_x as a nonlinear

coefficients, resulting in the following drag matrix:

$$D(\nu) = \begin{bmatrix} -d_x + d_{x,nl}|\nu| & 0 & 0 & 0 & 0 & 0 \\ 0 & -d_y & 0 & 0 & 0 & 0 \\ 0 & 0 & -d_z & 0 & 0 & 0 \\ 0 & 0 & 0 & -d_\phi & 0 & 0 \\ 0 & 0 & 0 & 0 & -d_\theta & 0 \\ 0 & 0 & 0 & 0 & 0 & -d_\psi \end{bmatrix} \quad (5.8)$$

The buoyancy forces have been linearized using a small angle approximation, such that:

$$\sin(\phi) \approx \phi, \quad \cos(\phi) \approx 1 \quad (5.9)$$

$$\sin(\theta) \approx \theta, \quad \cos(\theta) \approx 1 \quad (5.10)$$

giving:

$$G = \begin{bmatrix} 0 & 0 & 0 & 0 & 0 & 0 \\ 0 & 0 & 0 & 0 & 0 & 0 \\ 0 & 0 & 0 & 0 & 0 & 0 \\ 0 & 0 & 0 & B_p & 0 & 0 \\ 0 & 0 & 0 & 0 & B_r & 0 \\ 0 & 0 & 0 & 0 & 0 & 0 \end{bmatrix} \quad (5.11)$$

This model will be the basis for the extended kalman filter along with the measurement model presented next.

5.1.1 measurement model

The measurement model relates the state vector to the observation vector, which is defined by the available sensors derived in section 2.2. The observation then becomes:

$$z_k = \begin{bmatrix} z_{k,GPS}^{\{x_n, y_n, z_n\}} & z_{k,incl}^{\{\phi, \theta\}} & z_{k,GPS}^\psi & z_{k,GPS}^{\{\dot{x}_n, \dot{y}_n\}} & z_{k,gyro}^{\{\dot{\phi}, \dot{\theta}, \dot{\psi}\}} & z_{k,accel}^{\{\ddot{x}_b, \ddot{y}_b, \ddot{z}_b\}} \end{bmatrix}^T \quad (5.12)$$

Where the subindexes denotes which sensor the samples originate from in order to distinguish between the different update rates of the IMU and GPS. The observation matrix is based upon the measurement vector, z_k and the state vector, x_k and is found to be:

$$H(x_k) = \begin{bmatrix} I^{6x6} & 0^{6x3} & 0^{6x6} & 0^{6x3} \\ 0^{2x3} & R_b^{n,2x3} & 0^{2x3} & 0^{2x3} \\ 0^{3x6} & 0^{3x3} & I^{3x3} & 0^{3x3} \\ 0^{3x6} & 0^{3x3} & 0^{3x3} & I^{3x3} \end{bmatrix} \quad (5.13)$$

Where $R_b^{n,2x3}$ is the truncated rotation matrix from $\{\text{b}\}$ to $\{\text{n}\}$ such that it rotates $\{x_n, y_n, z_n\}$ to $\{x_b, y_b\}$ as z_b is not measured.

5.2 Verification of Discretization

As the model is discretized using Forward Euler method, it have to be verified that this does not introduce instability into the model. In order to verify the performance of the Discretized model, it is compared to the continuous model. This is done in order to ensure the chosen sample time of 0.005s is sufficient. The simulation is done with a input vector of $u = [\frac{\pi}{4} \ 30]^T$ and initial states set to zero.

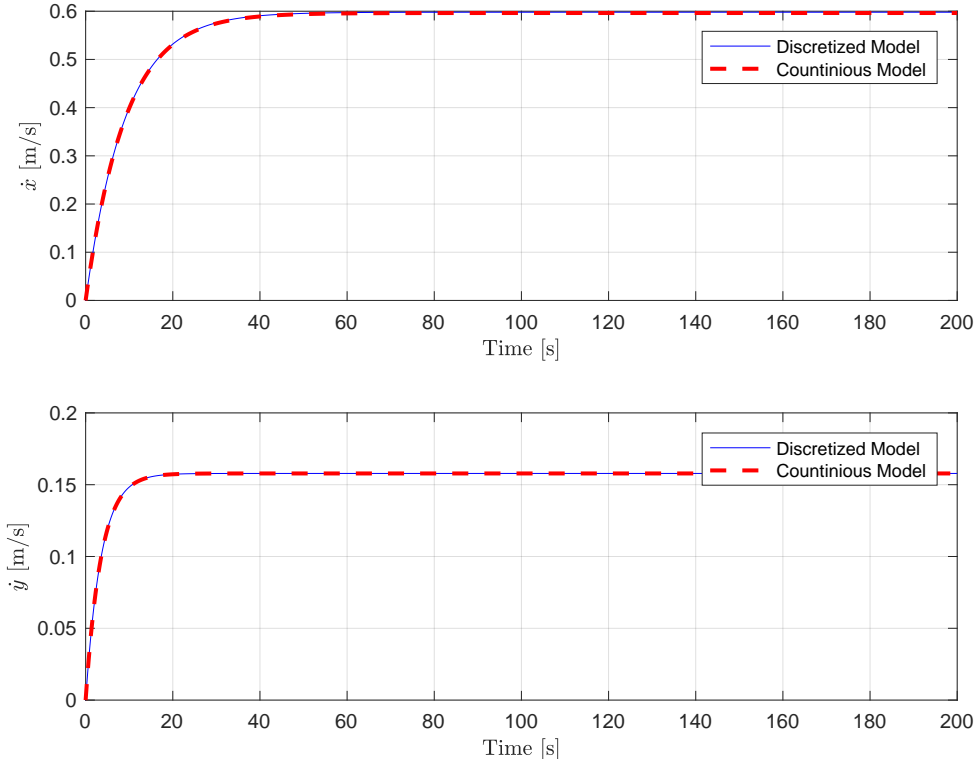


Figure 5.1: Comparison of Translational velocities between The Discrete and continuous model

Figure 5.1 shows the comparison between the Discrete and continuous model. As shown on the graph, the discrete model follows the continuous model without significant deviation.

Figure 5.2 shows the angular accelerations in ϕ and θ . As shown in the figures, the discrete system oscillates with a higher amplitude than the continuous model. From further analysis, this deviation is mainly caused by the small angle approximation of the buoyancy force presented in section 5.1 and is deemed negligible.

Furthermore, the frequency and settling time of the discrete system closely matches the continuous model and the system shows no sign of instability.

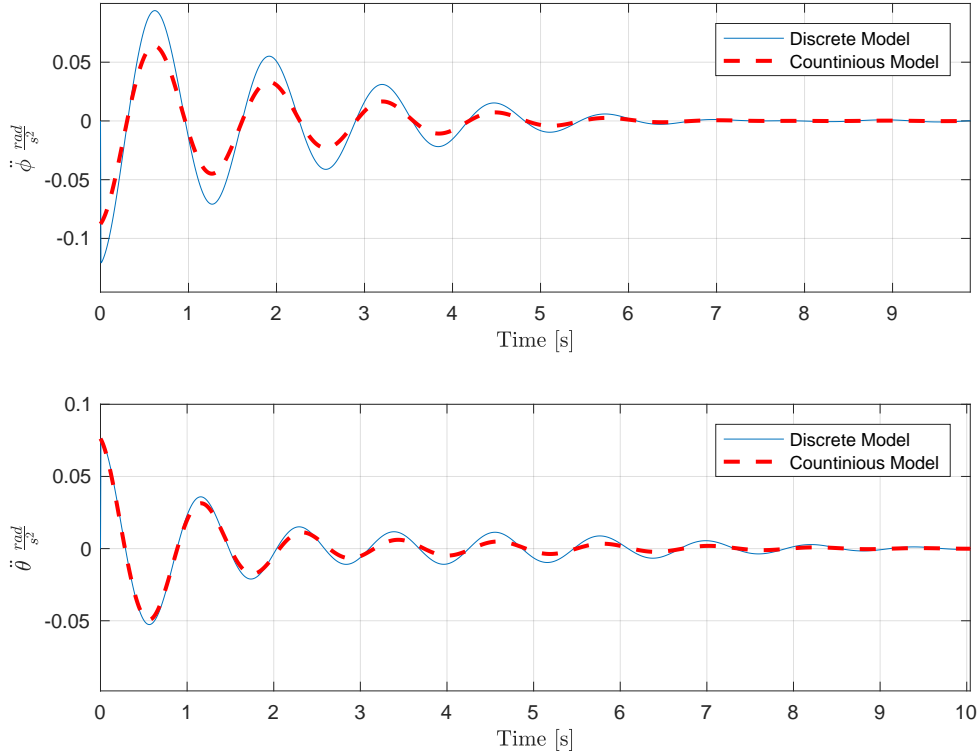


Figure 5.2: Comparison of angular accelerations between the Discrete and continuous model

Finally the discrete model is verified by comparing the simulated positions in $\{n\}$. As expected, the discrete model follows the position of the continuous model.

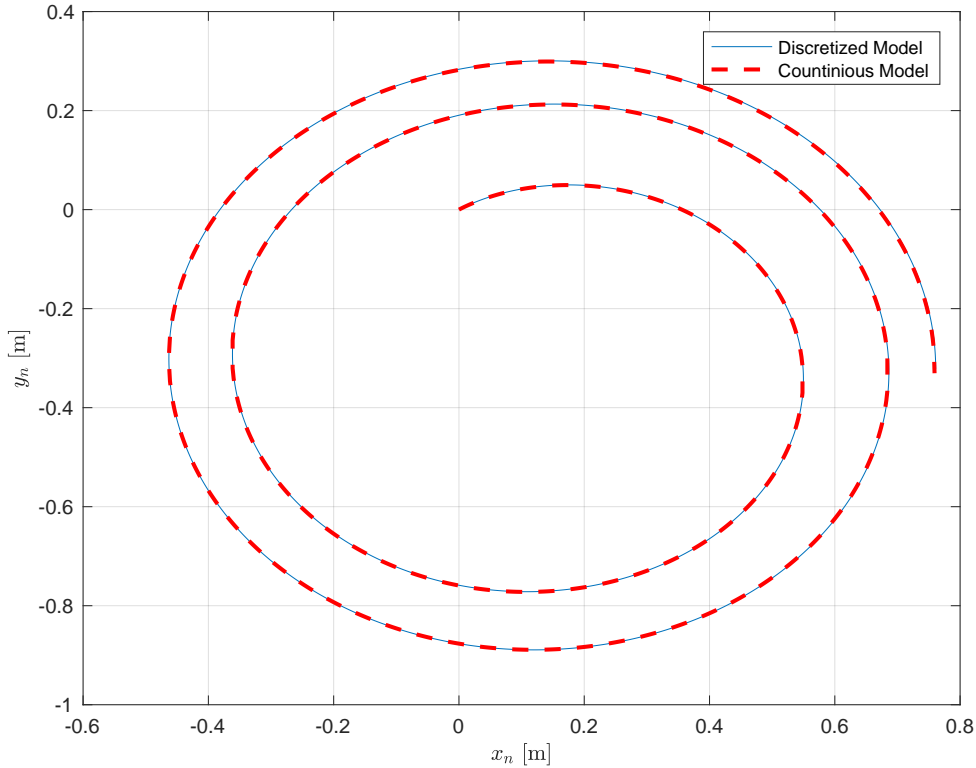


Figure 5.3: Discretization of position

From the above analysis it can be concluded that the discretized model have sufficient

5.3 Kalman Colored Noise Compensation

As the kalman filter is a Bayesian filter, a basic assumption behind it is that the noise sources is white Gaussian. One might encounter normal distributed noise which is correlated. Such noise is generally termed colored noise.

This behavior can be modeled, extending the system with a filtered state of the correlated measurement, as resulting in the following model: [26, p. 148]

$$x_{ext,k} = \begin{bmatrix} x_k \\ x_{lp,k} \end{bmatrix} = \begin{bmatrix} A & 0 \\ 0 & A_{lp} \end{bmatrix} \begin{bmatrix} x_{k-1} \\ x_{lp,k-1} \end{bmatrix} \quad (5.14)$$

$$z_{ext,k} = \begin{bmatrix} h(x_k) & I & x_{ext,k} \end{bmatrix} \quad (5.15)$$

Where:

$x_{ext,k}$ Is the extended state vector

$z_{ext,k}$ Is the extended observation vector

$x_{lp,k}$ Is the low pass filtered state extended to the system

- A Is the discretized dynamic model of the system
 A_{lp} Is the extended dynamic model of a low pass filter

This works as a shaping filter for the noise signal, such that the white Gaussian assumption can be applied to the filtered signal. [26, p. 148]

Specifically it has been shown that for a Gauss-Markov process with autocorrelation function: [27]

$$C(t) = e^{-\alpha t} \quad (5.16)$$

The dynamic system, shown in 5.17 models this behavior.

$$\dot{x}_{lp}(t) = -\alpha \cdot x_{lp}(t) + w_{lp}(t) \quad (5.17)$$

This can be discretized to become: [27]

$$x_{lp}(k) = -e^{-\alpha \Delta t} \cdot x_{lp}(k) + w_{lp}(k) \quad (5.18)$$

Where w_{lp} is a white noise random variable which drives the filter.

As shown in Appendix E the inclinometer was shown to have such behavior, this is further discussed in subsection 3.5.4, where this behavior is attributed to the low pass effect of the inclinometer. This effectively results in the kalman filter receiving a filtered version of the expected measurement. Using 5.16 the time constant can be found to be $\alpha = 0.0025s$. When comparing with the update rate of the kalman filter, which acts as a sample rate of the filter, basic filter theory shows that this is $\frac{1}{4}$ of the Nyquist rate meaning the correlated noise of the inclinometer can be considered negligible.

5.4 Kalman Bias Drift Compensation

The measurement model relates measurements from the sensors to the states of the system. As stated in subsection 2.2.3 the model is equipped with two sensors, a IMU and a RTK GPS. The derived model for the sensors described section 3.5 is used when modeling the sensors available to the system.

The Model for the MEMS gyroscope and accelerometer includes a bias term, while the RTK GPS and the inclinometer is assumed to be unbiased. While the biases of the gyroscope and accelerometer cannot be observed directly, an estimate of the state can be archived by extending the state vector with the bias states.

$$x_{ext} = \begin{bmatrix} x \\ \vdots \\ x_{bias} \end{bmatrix} \quad (5.19)$$

Chapter 5. Kalman Filter Design

Where:

$$x_{ext} \quad \text{Is the extended state vector} \quad [x_{ext} \in \mathbb{R}^{24}]$$

$$x_{bias} \quad \text{Is introduced bias states} \quad [x_{bias} \in \mathbb{R}^6]$$

The bias states introduced by the measurement model must also be introduced into the dynamics of the system. The sensors are modeled as a wiener process, that being a AWGN term integrated over time such that

$$x_{bias,0} = \mu_{bias} \quad (5.20)$$

$$x_{bias,k} = x_{bias,k-1} + w_k \quad (5.21)$$

By initializing the bias states to the stationary bias of the sensors, the resulting bias model is a noise driven bias, which take random walk around a known mean. This model is introduced into the dynamics of the system, such that the extended dynamics becomes:

$$A_{ext} = \begin{bmatrix} A^{18 \times 18} & 0^{18 \times 6} \\ 0^{6 \times 18} & I^{6 \times 6} \end{bmatrix} \quad (5.22)$$

$$z_k = \begin{bmatrix} H^{14 \times 18} & H_{ext}^{14 \times 6} \end{bmatrix} x_{ext} \quad (5.23)$$

Where:

$$z_k \quad \text{Is the measurement vector}$$

$$h(x_k) \quad \text{Is the nonlinear observation matrix}$$

$$b \quad \text{Is the bias vector}$$

$$n_k \quad \text{Is the measurement noise experienced at time k}$$

Equation 5.23 Shows the extended measurement model for the system.

5.5 Multi Rate Kalman Filtering

The system attempts to fuse two sensors with different sample rates together. This results in the filter experiences $k = \frac{T_{s_{imu}}}{T_{s_{GPS}}}$ consecutive samples where only a IMU sample is available. In order to prevent the filter discarding the IMU measurements, a multi-staged kalman filter is implemented. By implementing multiple stages into the filter, a stage where the GPS and IMU measurements are merged, and a state where the position and velocity is estimated.

This is done by increasing the covariance of the measurements from the GPS, indicating that no information is available, thus relying more on the IMU data than the outdated GPS position such that:

$$R_{GPS}(t) = \begin{cases} \Rightarrow \infty & \text{ift } \neq k \cdot T_{s_{imu}} \\ \sigma_{GPS} & \text{if } = k \cdot T_{s_{imu}} \end{cases} \quad (5.24)$$

Where:

R_{GPS} Is the covariance sub matrix associated with the GPS measurements

σ_{GPS} Is the known variation associated with the GPS measurements

Ts_{GPS} Is sample rate of the GPS

Ts_{IMU} Is the sample rate of the IMU

k Is the amount of IMU samples in between GPS measurements

Additionally, this technique allows the system to perform Dead Reckoning in case of a GPS outage, such that the system could still be operational.

5.6 Simulation Results

The following section presents the results when evaluating the performance of the sensor fusion algorithm presented in section 4.1. The simulation presents two scenarios, one where no external disturbances are induced upon the system, and one where external forces are added as described in Equation 3.4. The first scenario is intended to get a baseline result of how the filter performs under ideal circumstances to get a baseline for comparison, and the second how well the system handles disturbances.

5.6.1 Method

The system is modeled with the sensor noises found in Appendix D and Equation F.0.4 as well as the coefficients found in Appendix B with initial states of $x_{2,i} = 0 \forall x_0$. The simulation is performed with an input vector of $u = [\pi 5, 30]^T$ for the first 50 seconds, and then $u = [\pi 5, 0]^T$ for the rest of the simulation. The system is simulated for 120 seconds.

In addition to the Gaussian noise, a wiener process is generated to simulate the bias drift of the gyroscope and the accelerometer. The following values have been used to generate the biases:

$$\sigma_{gyro,walk} = Ts \cdot 2.4207 \cdot 10^{-6} \frac{rad}{s} \quad (5.25)$$

$$\sigma_{accel,walk} = Ts \cdot 1.3639 \cdot 10^{-7} \frac{m}{s^2} \quad (5.26)$$

These values are based on the data sheet for the IMU. [12] One process is generated for each axis on each sensor, resulting in a total of 6 unique wiener processes, 3 for each sensor.

5.6.2 Results

Below is the results of of a Monte Carlo simulations with a total of 200 iterations. This is done to test the robustness of the filter towards measurement noise, as well as to reveal overall trends in the estimations. An error bound is generated at 1 and 3 standard deviations with respect to the simulated value, indicating how much the estimator is expected deviate from the actual value. The resulting THU of the filter is then computed, which will be compared to the noise from the sensors alone to evaluate the fulfillment of the requirements described in section 1.4.

accelerations

Figure 5.4 show the resulting error bounds of the translatory accelerations.

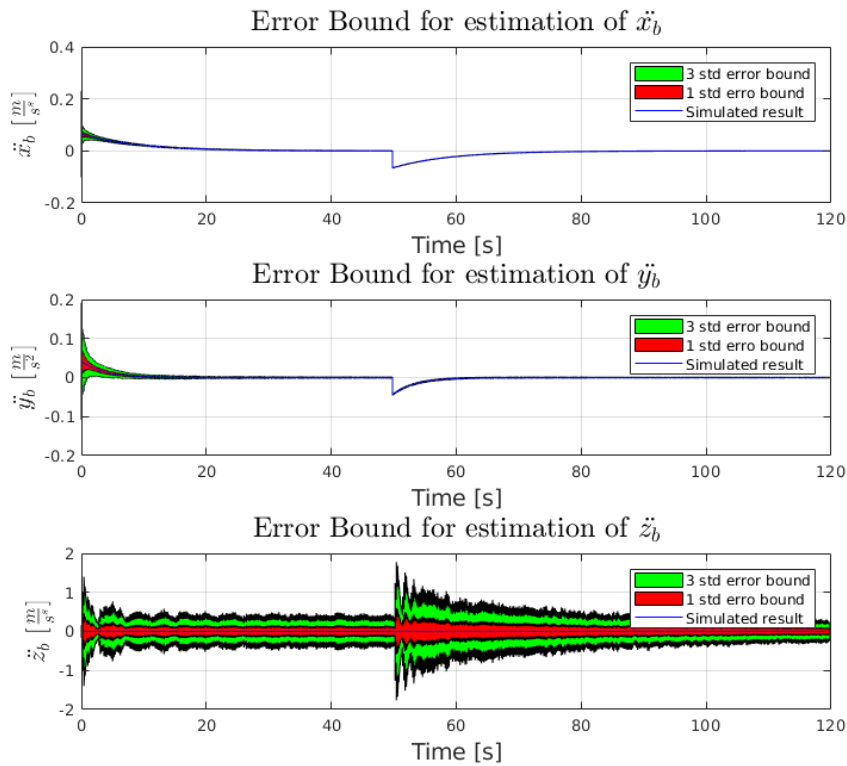


Figure 5.4: Error bounds for translatory accelerations

Here, it can be seen that the estimate of \ddot{x}_b and \ddot{y}_b is very similar to the simulated, while the error bound of \ddot{z}_b is significantly larger.

Figure 5.4 show the resulting error bounds of the translatory accelerations.

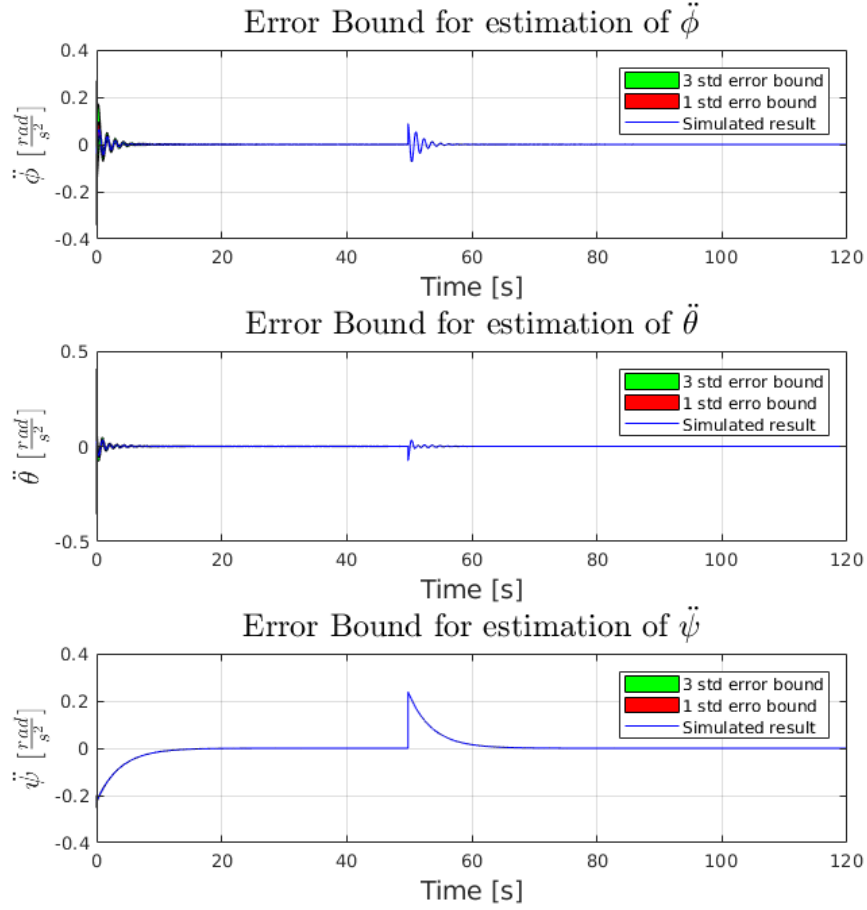


Figure 5.5: Error bounds for angular accelerations

velocities

Figure 5.6 shows the translatory velocities. From the figures it is shown that the estimate of the translatory velocities \dot{x}_b and \dot{y}_b is estimated close to the real value. While some deviation exists within the first 5 seconds of the simulation, they eventually converge close to the simulated value. The estimate of \dot{z}_b is expected to deviate more than \dot{x}_b and \dot{y}_b as there is no measurement of \dot{z}_n , meaning the estimate relies on z_n and \ddot{z}_b , which is seen on the graph.

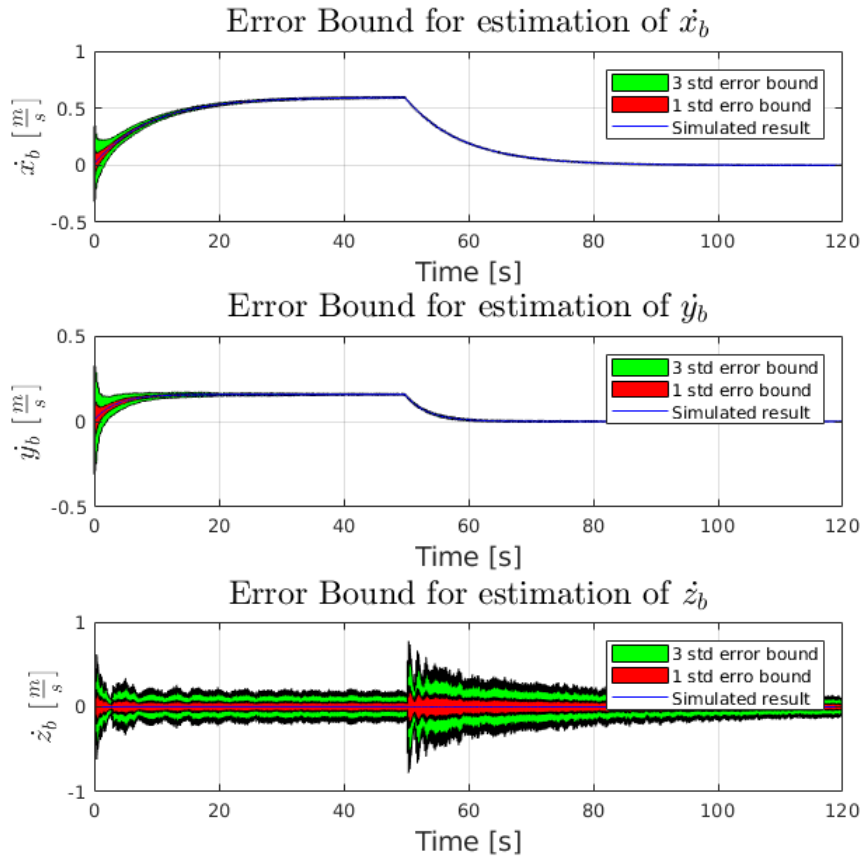


Figure 5.6: Error bounds for the translatory velocities

The estimation of angular rates is shown in Figure 5.7.

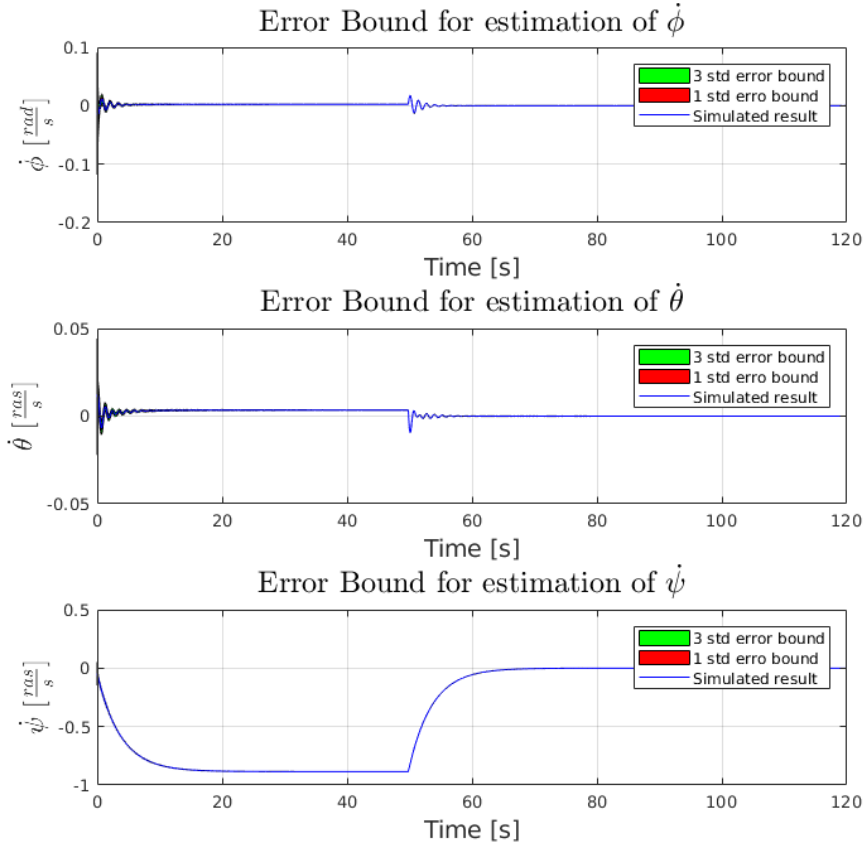


Figure 5.7: Error bounds for the angular rates

While the small angle approximation have a noticeable impact upon the estimation, this is mostly noticeable when the system oscillates.

Position and Orientations

The estimation of the position of the vessel within $\{n\}$ is shown in Figure 5.8. The x and y axis shows some increased initial deviation, which then converges after 10-20 seconds. Significant deviations is shown in z, which increases to $\pm 1m$ after 50 seconds when the motor is turned off.

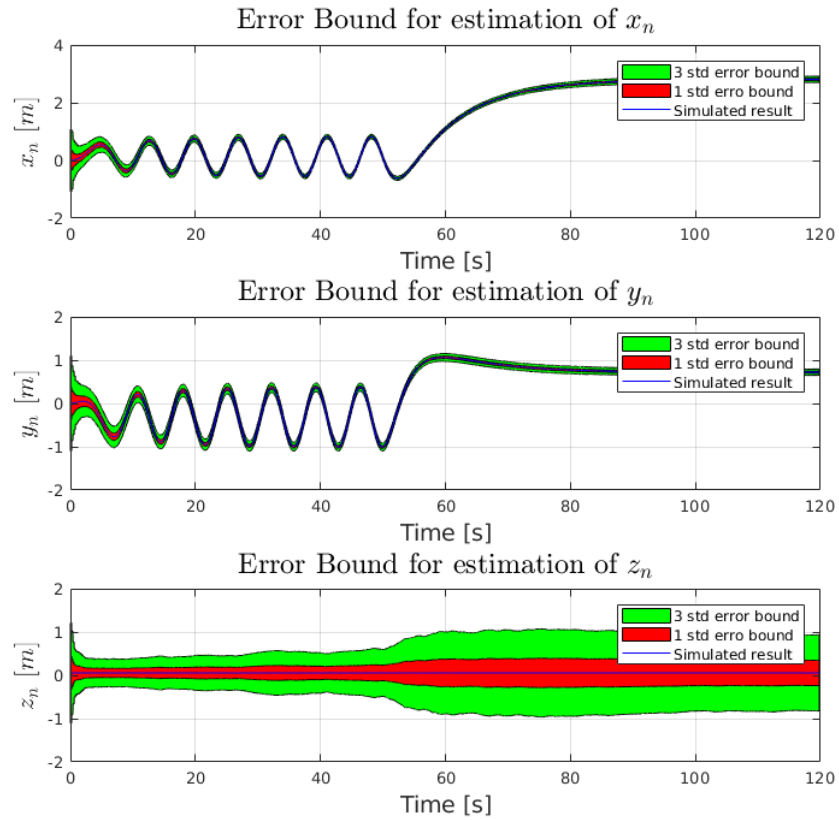


Figure 5.8: Error bounds for the Position in $\{n\}$

The error bounds for the orientation is shown in Figure 5.9. From inspection it can be seen that at crossover points, ψ shows significant deviations momentarily.

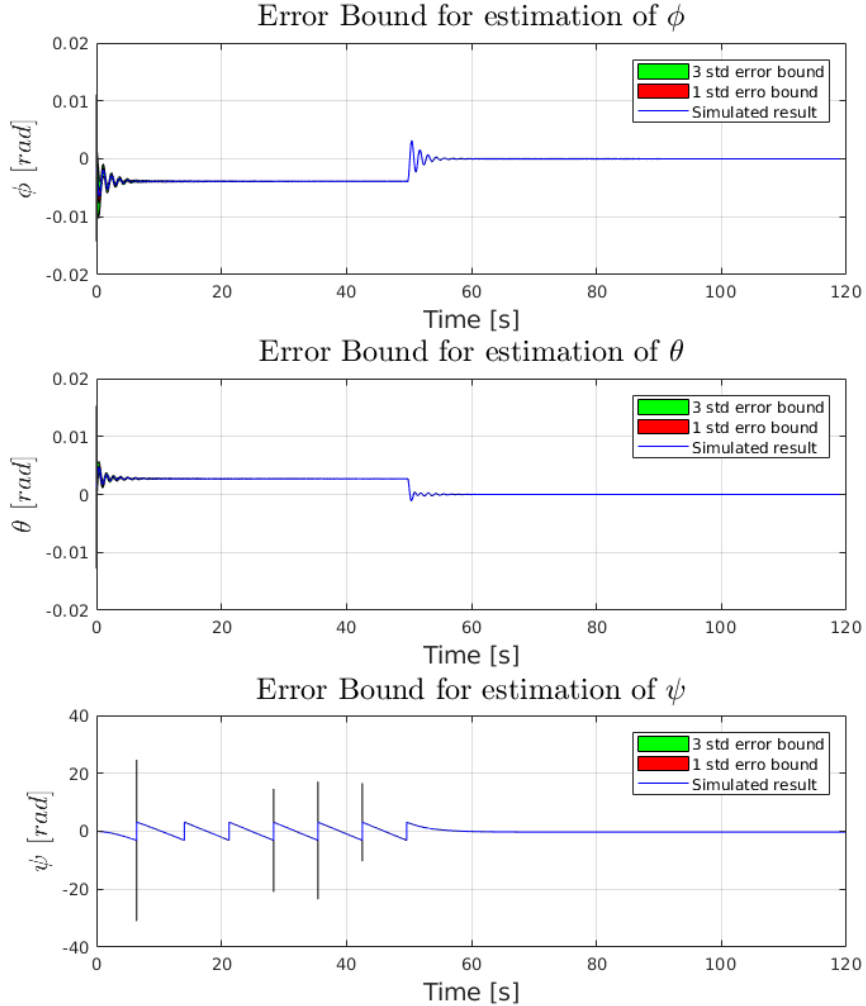


Figure 5.9: Error bounds for the orientation of the system

5.6.3 Evaluation

The above data shows a good noise rejection for the axis relevant to the THU. As a result, the THU_{99} have been found to be $0.2892m$ for the filtered data while the THU_{99} was found to be $4.8212m$ using the generated noises for the sensors. This suggests that the filter is capable of reducing the noise to a degree where hydrographic measurements is possible in shallow waters, fulfilling the requirements stated in section 1.4.

However when looking at the deviations experienced in z_n , some concerns arises. The system experiences a deviation of $\pm m$ within this axis at rest and $\pm .5m$ during operation. While estimation errors in this axis does not have a effect on the Horizontal uncertainty, this error increases the vertical uncertainties, also specified in the hydrostatic standards. From the whiteness anal-

Chapter 5. Kalman Filter Design

ysis in ?? this further shows that the data is neater normally distributed or uncorrelated. This indicates that there is some modeled processes in \ddot{z} which is needed in the discretized model.

6 | Conclusion

In this project the basis for a system capable of performing hydrographic measurements is presented. Requirements for such system have been investigated and from that design criterion for such system have been presented.

A dynamic model for the system have been derived, as well as a description of the sensor system. Methods have been presented for deriving the system coefficients, and most have been determined. Based on this model a extended kalman filter have been designed capable of meeting the criterion in a simulated environment using the determined coefficients for the sensor as well as the dynamic model.

While the system haven't been successfully implemented on a real application, the basis for this have been investigated and a estimation filter proposed. The simulations have shown to deliver a significant measurement noise reduction in a disturbance free environment.

7 | Future Work

While the simulation of the system have shown to fulfill the requirements, this haven't been Donn on a real application. The presented model for the system used coefficients obtained from testing of the system, however not all were determined successfully. Another test method for obtaining better oscillation in heave is required before the dynamic model of the system is acquired. Additionally, the tests should be redone with the sensors correct configured to give the desired sample rate, which could provide a better performance.

As the system is designed and tested in a simulated environment, which means some piratical problems is avoided. A test of the impact of sensor misalignment should be estimated, and a proper method of calibration should be developed. This could be as low piratical as mounting a strap for the measurement, such it is always mounted the same place with the same orientation.

Another practical problem is estimating the center of buoyancy for the vessel, as this would otherwise introduce biases to the inclinometer measurements as the restoring forces drives the error toward zero. This is potentially problem as even comparatively small deviations can have a big impact on the THU.

Additionally, for the system to function with the computed THU, the RTK capabilities of the GPS must be enabled and it's performance verified. This requires the platform to be equipped with a communication device capable of receiving the correction data.

Finally for the system to function autonomously, a control system must be added. This could build upon the presented system, as this supplies all the necessary states for a control system to function.

A | Appendix

B | Determination of Hydrodynamic and hydrostatic coefficients

Date: 2018-19-4

B.0.1 Objective

The purpose of this test is to determine to determine the hydrodynamic and hydrostatic coefficients used in the model of the vessel. The 6 DOF model contains the following hydrodynamic coefficients:

- Translational Drag Coefficients (d_x, d_y, d_z)
- Angular Drag Coefficients (d_ϕ, d_θ, d_ψ)
- Added mass coefficients: (m_x, m_y, m_z)
- Inertia coefficients: (I_x, I_y, I_z)

These parameters is to be determined imperially and will be used in the model for the system.

B.0.2 Theory: Surge, Sway and Yaw tests

The coefficients can be derived using a simplified version of the system model shown below:

$$M\dot{\nu} + D\nu + G\eta = \tau \quad (\text{B.1})$$

$$(\text{B.2})$$

This equation assumes the coriolis and centripetal forces are negligible, which can be achieved by minimizing the angular velocities. The τ vector is the input into the system, by knowing this, the coefficients can be derived. The Hydrodynamic coefficients can be estimated through obtaining a constant velocity in their respective axis, then turning off the input. By observing the resulting curve from a constant velocity to zero velocity, the drag coefficients can be estimated. The system is assumed to be a critically damped system, meaning the velocity is decay at a rate corresponding to:

$$\nu = k \cdot e^{-st} \quad (\text{B.3})$$

The resulting dynamic equation becomes:

$$M\dot{\nu} + D\nu = 0 \quad (\text{B.4})$$

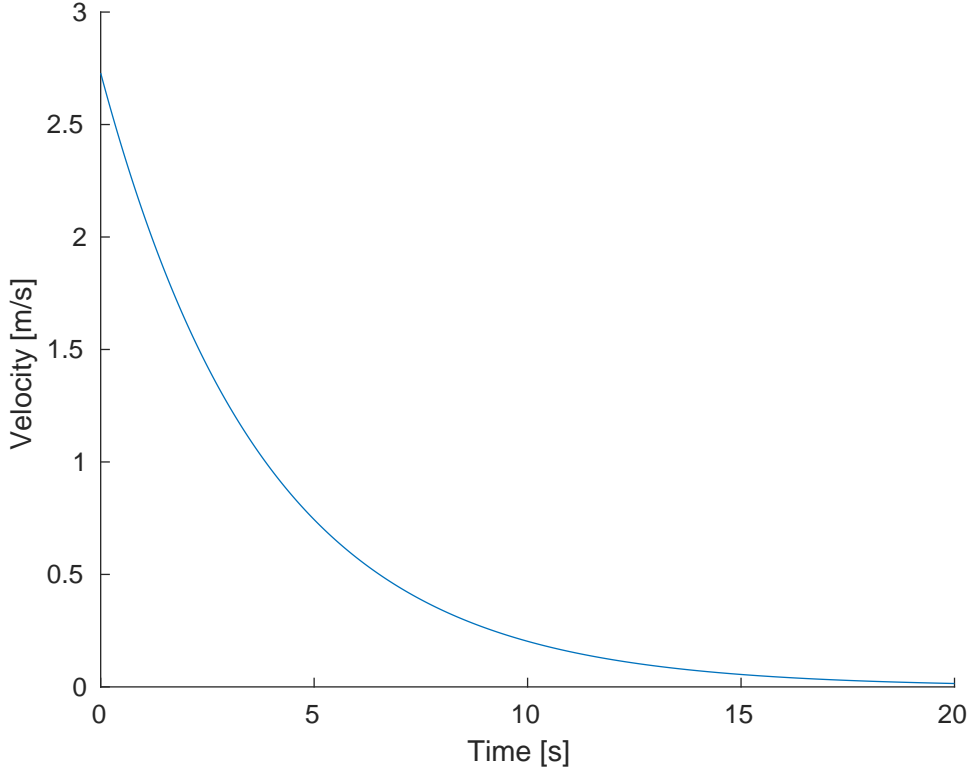


Figure B.1: Velocity curve with zero input

such that:

$$M\nu + D\nu = 0 \quad (\text{B.5})$$

$$M(-ks \cdot e^{-st}) + D(k \cdot e^{-st}) = 0 \quad (\text{B.6})$$

$$-Ms0D = 0 \quad (\text{B.7})$$

$$s = \frac{D}{M} \quad (\text{B.8})$$

$$\nu = k \cdot e^{-\frac{D}{M}t} \quad (\text{B.9})$$

The parameter k can be found to be the velocity at time 0 as:

$$\nu_0 = k \cdot e^{-\frac{D}{M}0} \quad (\text{B.10})$$

$$\nu_0 = k \quad (\text{B.11})$$

While this method can be used to determine the linear drag coefficients, it does not fully describe the dynamics of a nonlinear drag coefficient. As described in subsection 3.1.2, the system including nonlinear drag is modeled as:

$$M\ddot{x} = -d\dot{x} - d_n|\dot{x}| \cdot \dot{x} \quad (\text{B.12})$$

This equation will be used to fit the curve showing surge damping.

Appendix B. Determination of Hydrodynamic and hydrostatic coefficients

B.0.3 Theory: Roll, Pitch and Heave tests

Similarly to the sway surge and yaw tests, the coefficients are estimated by providing an excitation on the respective axis and then suddenly stopping, emulating an impulse. By measuring the behavior of the system until at rest, giving it no input, the hydrodynamic coefficients can be found. The following models are used for deriving the coefficients:

$$I_\phi \ddot{\phi} + D_\phi \dot{\phi} + B_\phi \phi = 0 \quad (\text{B.13})$$

$$I_\theta \ddot{\theta} + D_\theta \dot{\theta} + B_\theta \theta = 0 \quad (\text{B.14})$$

$$I_x \ddot{z} + D_z \dot{z} + B_z z = 0 \quad (\text{B.15})$$

These models are derived from the system model, and are second order homogeneous differential equations of the form:

$$a\ddot{\phi} + b\dot{\phi} + c\phi = 0 \quad (\text{B.16})$$

These systems are known to behave like a underdamped mass spring oscillator, such that the damping over time can be described by Equation B.17.

$$\phi(t) = k e^{-\sigma \cdot t} \cdot \cos(\omega_d t) \quad (\text{B.17})$$

Resulting in the curve shown in Figure B.2.

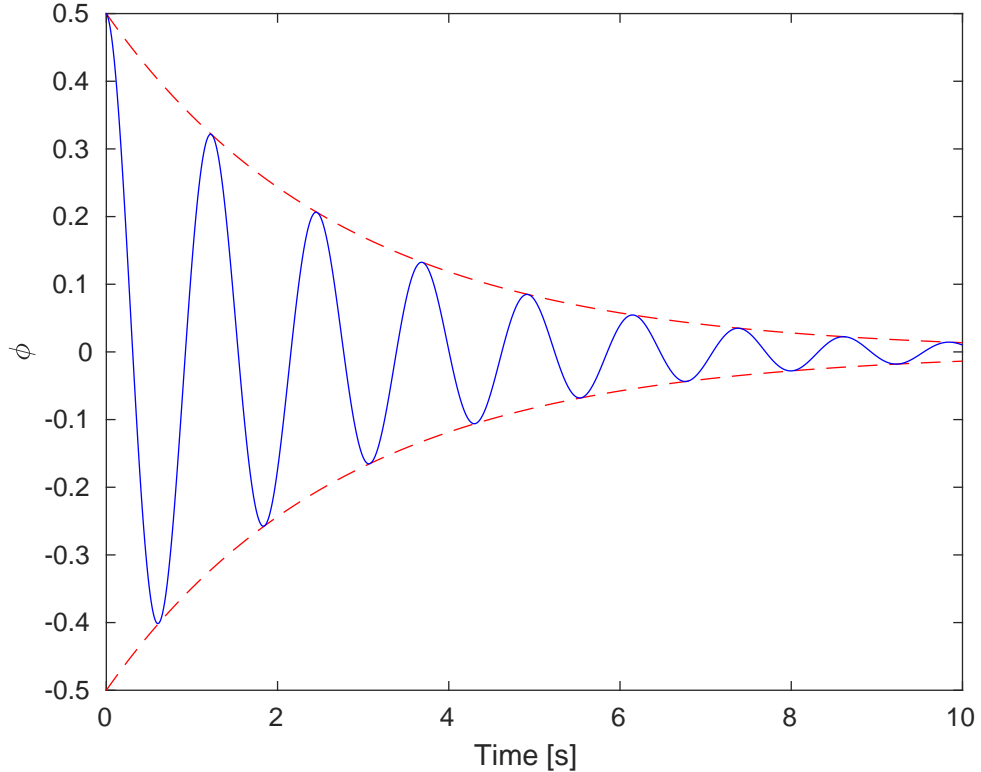


Figure B.2: illustration of a underdamped system

Here, the blue line shows the expected movement of the system experiencing an impulse in ϕ .

Appendix B. Determination of Hydrodynamic and hydrostatic coefficients

The red dotted lines shows how the amplitude of the oscillations is being damped as the energy of the system dissipates.

From Equation B.17 this can be found to be:

$$\phi(t) = ke^{-\sigma t} \quad (\text{B.18})$$

Which is a guessed solution to the homogeneous second order equation.

$$a\ddot{x} + b\dot{x} + cx = 0 \quad (\text{B.19})$$

$$\ddot{x} + \frac{b}{a}\dot{x} + \frac{c}{a}x = 0 \quad (\text{B.20})$$

$$\ddot{x} + 2\zeta\omega_0\dot{x} + \omega_0^2x = 0 \quad (\text{B.21})$$

Where:

ζ Is the exponential dampening ratio

ω_0 Is the undamped natural frequency

Substituting the guessed solution for ϕ into the second order homogeneous equation yields:

$$\sigma^2ke^{-\sigma t} - 2\zeta\omega_0\sigma ke^{-\sigma t} + \omega_0^2ke^{-\sigma t} = 0 \quad (\text{B.22})$$

$$\sigma^2 - 2\zeta\omega_0\sigma + \omega_0^2 = 0 \quad (\text{B.23})$$

which can then be solved by:

$$\sigma = \frac{-2\zeta\omega_0 \pm \sqrt{4\zeta^2\omega_0^2 - 4\omega_0^2}}{2} = -\zeta\omega_0 \pm \omega_0\sqrt{1 - \zeta^2} \quad (\text{B.24})$$

Through fitting Equation B.17 to the measurements, the following is known:

$$\sigma = \zeta\omega_0 \quad (\text{B.25})$$

$$\omega_d = \omega_0\sqrt{1 - \zeta^2} \quad (\text{B.26})$$

The drag coefficient can the be found to be:

$$b = 2\sigma = \frac{d}{m} \quad (\text{B.27})$$

And the hydrostatic coefficients can be found to be:

$$c = \frac{\omega_d^2 + \sigma^2}{a} = \frac{B}{m} \quad (\text{B.28})$$

Appendix B. Determination of Hydrodynamic and hydrostatic coefficients

B.0.4 List of equipment

The tests assumes access to a system similar to the ones described in section 2.2.

- RTK GPS - Timble-MB-Two
- IMU - Stim300
- Intel Nuc
- Rudder

B.0.5 Procedure

The Following sections describe the procedure for each test

Surge Test

The test will be performed by accelerating the vessel to a constant velocity, then turning off the motor. This will be done through multiple iterations, at different velocities by change the values with each iteration.

The test procedure is as follows:

1. Position the vessel perpendicular to the coast.
2. Through SSH Run The command: "rosrun core system.launch" on The Intel Nuc
3. Set motor input to a constant velocity.
4. Wait for the system to obtain constant velocity.
5. Turn off the motor.
6. Wait for the system to settle.
7. Repeat from step 2 until two iterations is made.
8. Through SSH stop the command from step 1.
9. Turn the vessel around facing opposite direction.
10. Repeat from step 1 for both directions.
11. Repeat from step 1 with new motor input until 4 iterations is made.

Sway Test

1. Secure line to the vessel.
2. Position the vessel perpendicular to the coast.
3. Through SSH Run The command: "rosrun core system.launch" on The Intel Nuc
4. Pull the line slowly towards the coast.
5. When the Vessel is moving at a constant velocity stop pulling the line
6. Wait for the system to settle.
7. Through a SSH connection stop command from step 3
8. Repeat from step 2 until 4 iterations are made.

B.0.6 Heave, Pitch and Roll Test

These test will be performed by oscillating the vessel on a given axis, then stopping. As there is not direct actuation in these axis, oscillation in the rotational axis is done by shifting weight from side to side in phase with the oscillations. In a similar fashion, oscillation in heave is archived by shifting weight up and down, in phase such that oscillation is archived.

1. Oscillate the axis corresponding to the current iteration
2. Through SSH Run The command: "rosrun core system.launch" on The Intel Nuc
3. Wait for the system to be sufficiently excited
4. Stop oscillation
5. Through SSH stop command from step 2
6. wait for the system to be at rest
7. repeat from step 1 next iteration until 4 iterations is made

Yaw Test

The yaw test is performed by obtaining an rotational velocity, then stop giving the system input. As the actuation system is not able to provide actuation on the yaw axis isolated, a set of rudders is used. By moving the rudders in opposite directions, rotation around yaw can be archived without significant action on other axis. To get an accurate approximation of the drag force in yaw, rudders must be out of the water when no actuation is done, as these have a drag contribution. To compensate for the vessel being performed by manpower and the potential issues this causes when replicating the test, multiple tests are performed to get a more stable result.

1. Obtain rotation around ψ by moving the rudders in the pattern described above.

Appendix B. Determination of Hydrodynamic and hydrostatic coefficients

2. Wait for the system to obtain constant velocity.
3. Remove the rudder from the water.
4. Wait for the system to settle.
5. Repeat step 1, but move in the opposite direction until 4 tests are made total.

B.0.7 Parameter Fitting

The following section will be used to analyze the acquired data from the different tests. While the test was performed as described, a missing script in the system made the IMU acquire data at a rate of $6.25Hz$ instead of the assumed 100. while this does effect the measurements for the relevant tests, the procedure and analysis is still relevant, but could be improved with better measurements. To convert the GPS coordinates to distance, the Haversine equation is used shown below:[14]

$$a = \sin^2(\Delta\phi/2) + \cos(\phi_1) \cdot \cos(\phi_2) \cdot \sin^2(\frac{\Delta\lambda}{2}) \quad (B.29)$$

$$c = 2 \cdot \text{atan}2(\sqrt{a}, \sqrt{(1-a)}) \quad (B.30)$$

$$d = R \cdot c \quad (B.31)$$

Equation B.31

similarly the heading is obtained by: [14]

$$\psi = \text{atan}2(\sin(\Delta\lambda) \cdot \cos(\phi_2), \cos(\phi_1) \cdot \sin(\phi_2) - \sin(\phi_1) \cdot \cos(\phi_2) \cdot \cos(\Delta\lambda)) \quad (B.32)$$

Surge fitting

During testing, no velocity measurements received, so the velocity is estimated by dividing the distance traveled by the sample rate. The model used to fit the parameters is:

$$\ddot{x} = -(\frac{d_x}{m_x} + \frac{d_{nlx}}{m_x} \|\dot{x}\|)\dot{x} \quad (B.33)$$

From the model fitting the two coefficients is found to be:

$$d_x = 0.11 \quad (B.34)$$

$$d_{nl} = 0.0005 \quad (B.35)$$

The fitting is done by initializing Equation B.33 to the velocity relative to the water speed, which is assumed to be the velocity of the vessel at rest. Equation B.32 is used to separate the velocities into \dot{x} and \dot{y} to better results.

Figure B.3 Shows the fitted curve in red compared with the measured velocities in blue, using Equation B.33 with the fitted coefficients. The coefficients is fitted to the first two measurements, then verified by the remaining measurements. This is done to prevent over fitting to the data.

Appendix B. Determination of Hydrodynamic and hydrostatic coefficients

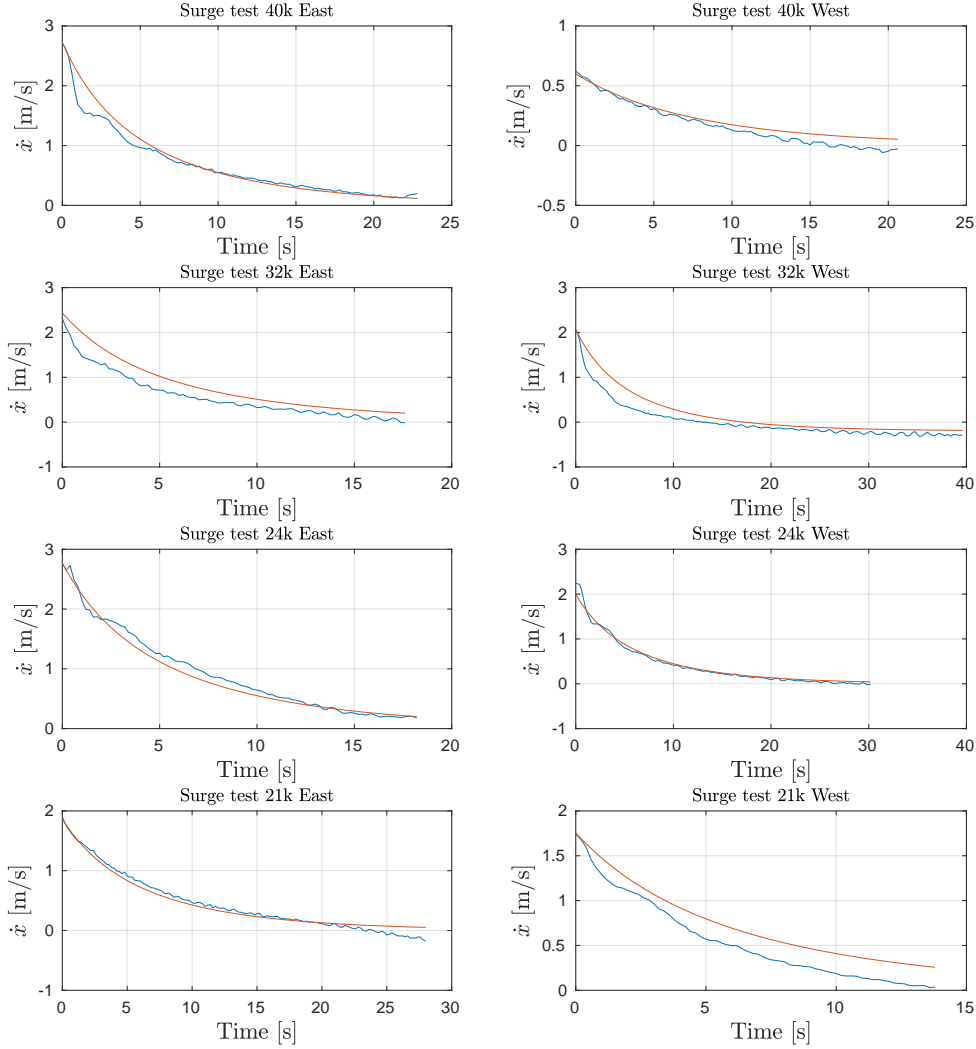


Figure B.3: Fitted curve to surge

Some disturbances can be seen in the data, most significantly in "Surge test 40K East". Here some ripples can be seen before the system follows the curve. This is assumed to be due to the vessel planning, as this was observed on some of the test, and will alter the coefficients of the vessel and cannot be accounted for with the current model.

Sway Fitting

The sway coefficients is obtained similarly too the surge analysis, however a linear model is used to fit this model. From the theory, the system is assumed to be critically damped, which is known to have the following:

Appendix B. Determination of Hydrodynamic and hydrostatic coefficients

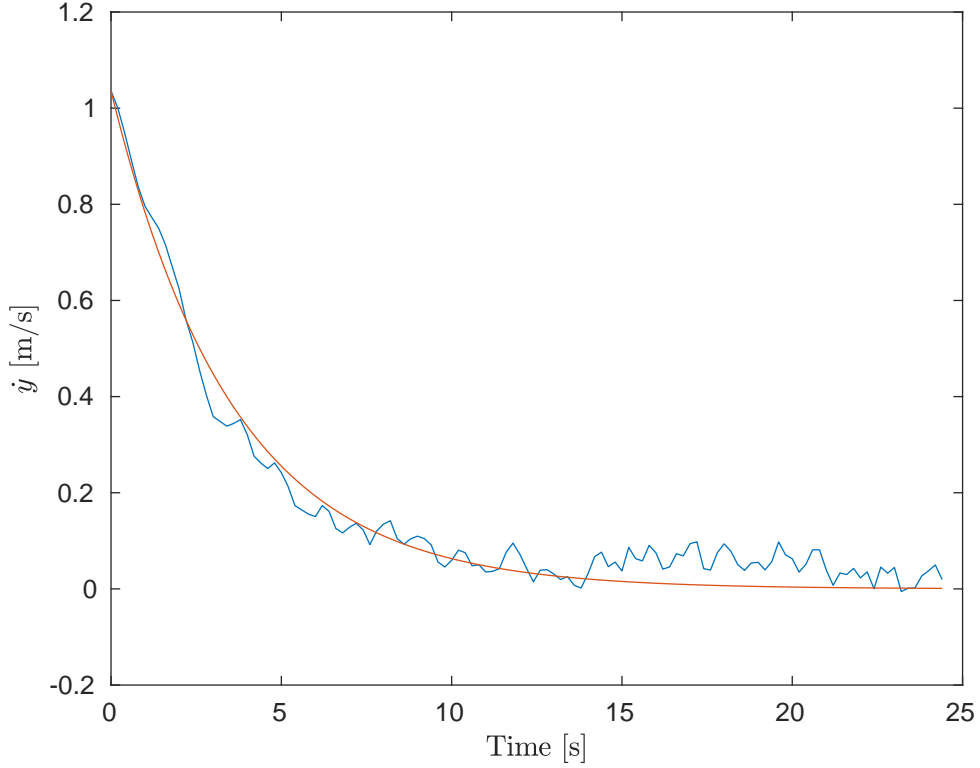


Figure B.4: Fitted curve to sway

Figure B.4 shows the fitted curve in red, compared with the measured data in blue with the following estimated coefficient:

$$d_y = 0.28 \quad (\text{B.36})$$

Yaw Fitting

The yaw is modeled as a critically damped system, meaning the regression curve is described by Equation B.3 which have been used to fit the data. The model is fitted to the measured gyroscope data, showed in:

The figure shows multiple tests are performed. The data is fitted to the curve from test 2 as this resembles the expected regression curve the best, and is thus assumed to be the best representation of the system.

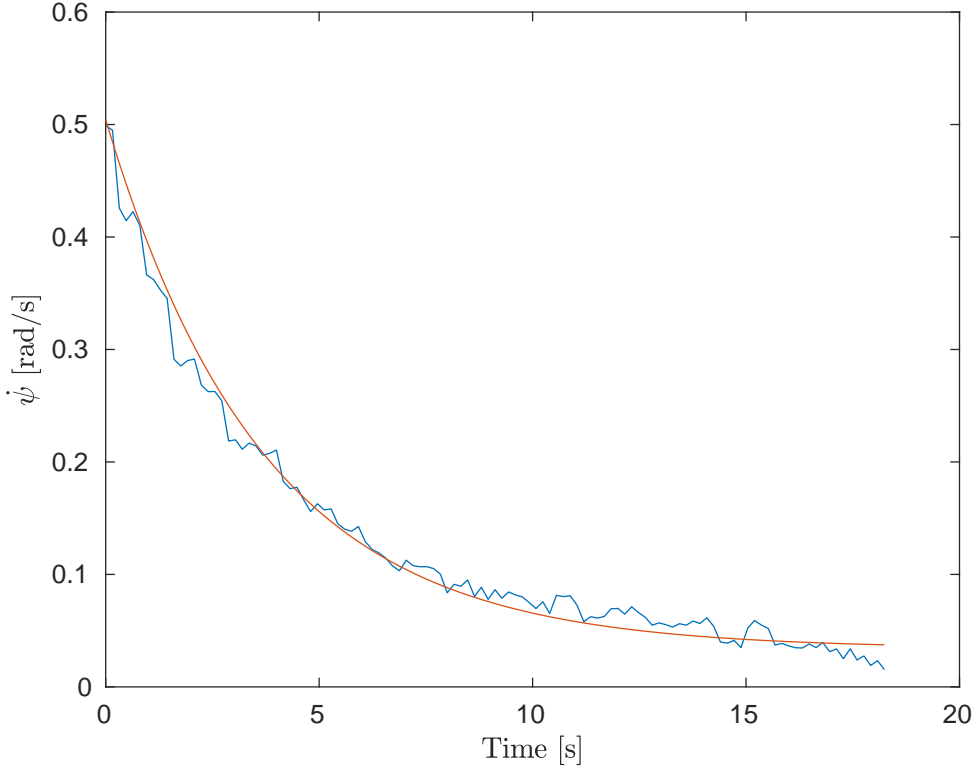


Figure B.5: Fitted curve to Yaw

From the fitted data the drag coefficient is found to be:

$$\frac{d_\psi}{I_\psi} = 0.27 \quad (\text{B.37})$$

Roll Fitting

Ideally the inclinometer data would be used for the fitting, however after analyzing the inclinometer data from the measurements, this is not feasible. This is assumed to be due to the low-pass filter effect of the inclinometer described in subsection 3.5.4. Instead, the fitting data can be estimated from integrating the gyroscope data. Figure B.6 Shows the data measured by the gyroscope.

Appendix B. Determination of Hydrodynamic and hydrostatic coefficients

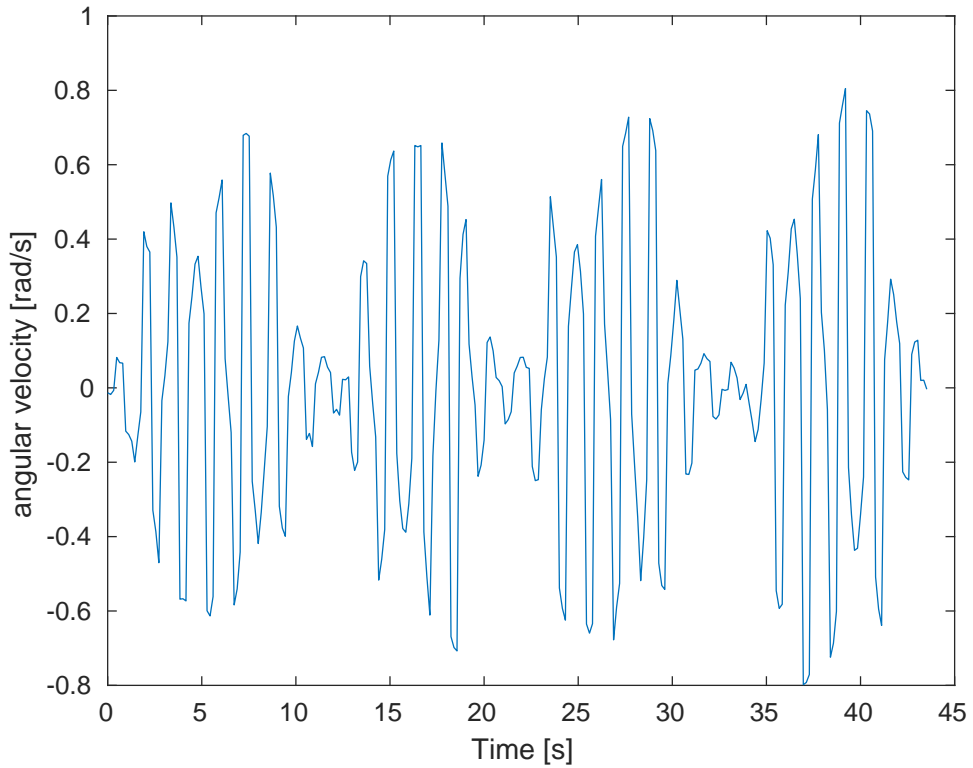


Figure B.6: Measured data from the gyroscope

This data have been intergated to obtain the estiate of ϕ presented in Figure B.6.

Figure B.7 shows the result of this.

Appendix B. Determination of Hydrodynamic and hydrostatic coefficients

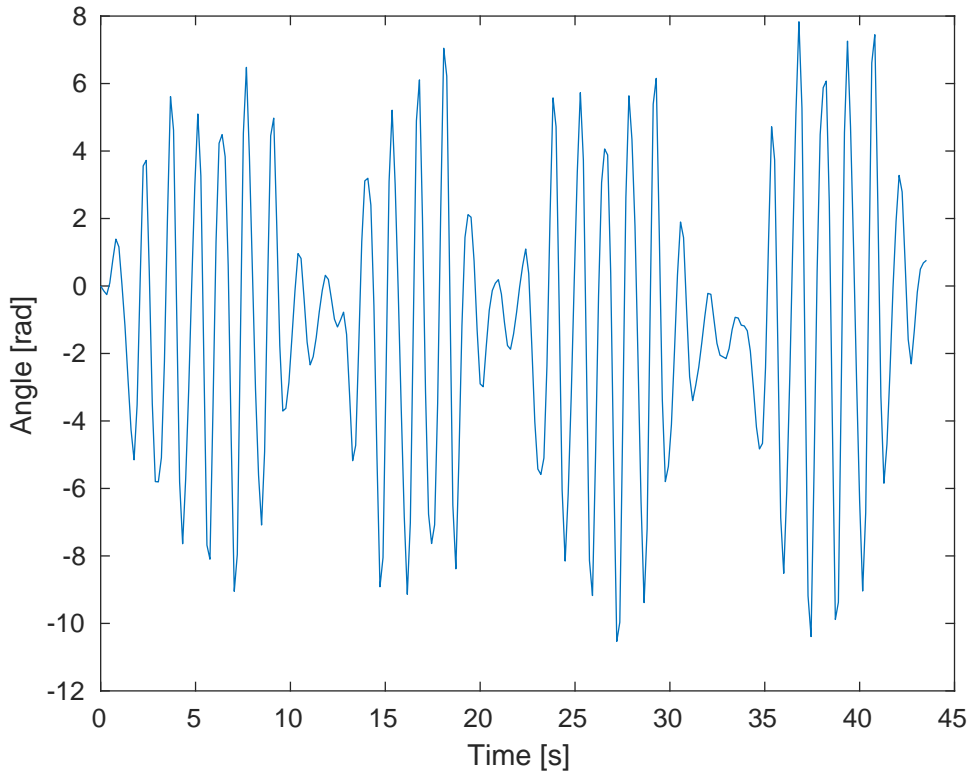


Figure B.7: Roll obtained from integration of gyro measurements

The integrated data is then used to perform the parameter fitting, as shown in Figure B.8. The Blue curve shows the integrated roll velocity, the red line shows the fitted second order system and the red dotted line shows the amplitude damping.

Appendix B. Determination of Hydrodynamic and hydrostatic coefficients

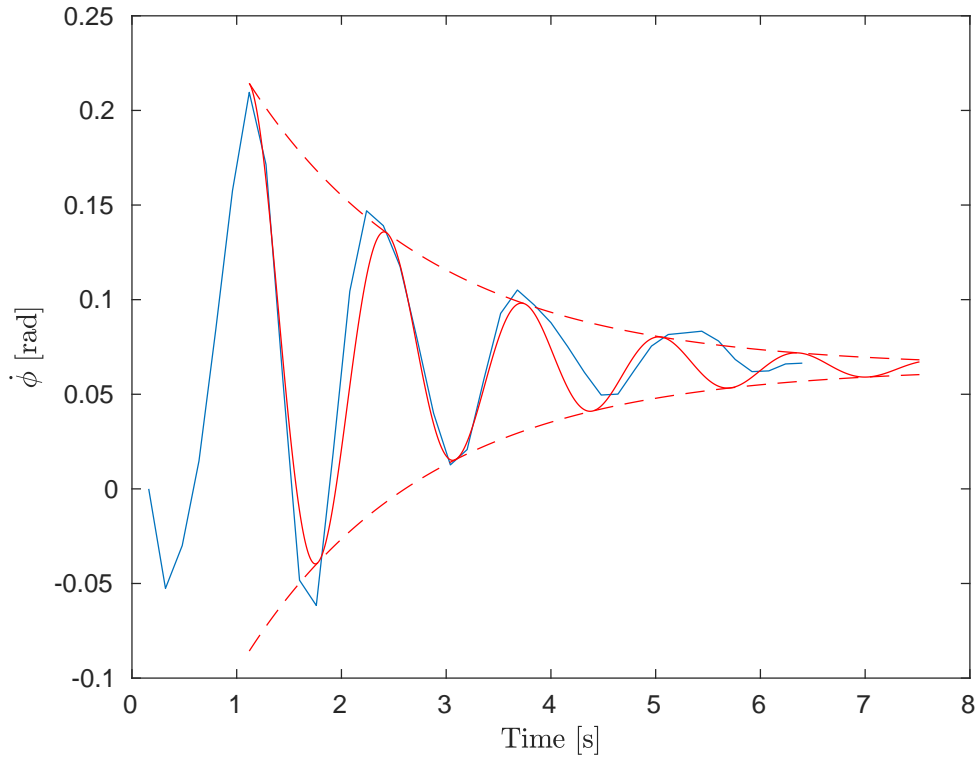


Figure B.8: Fitted curve to Roll

From the fitted curve, the coefficients is found to be :

$$d_\phi = 1.14 \quad (\text{B.38})$$

$$B_\phi = 23.269 \quad (\text{B.39})$$

Pitch Fitting

Similarly to the roll analysis, the integrated gyroscope data is used to estimate the coefficients for the pitch.

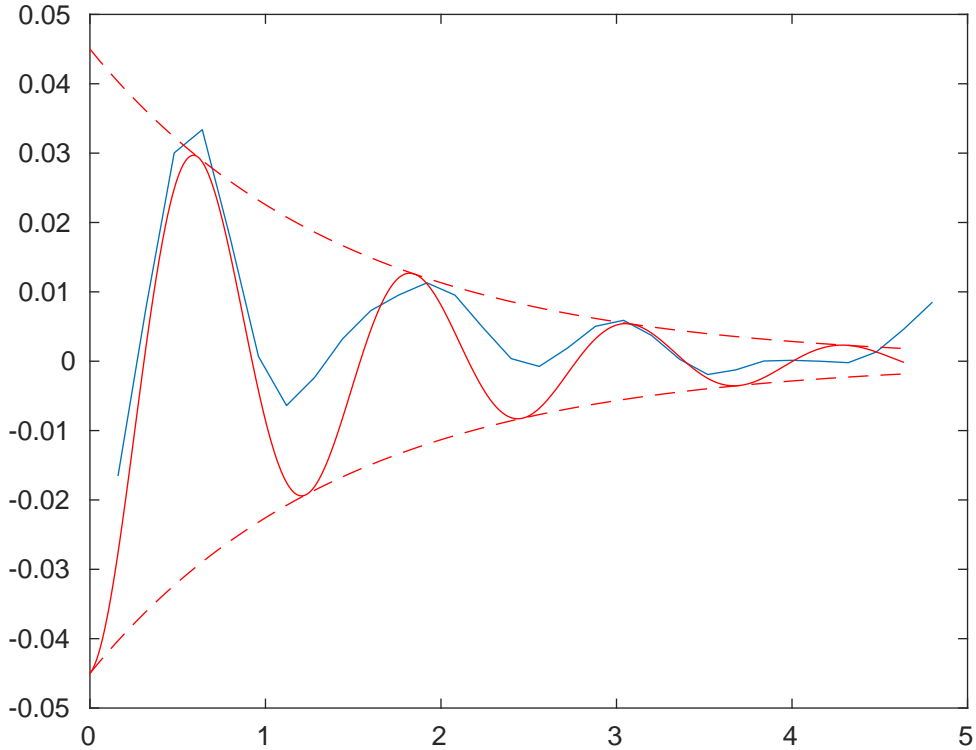


Figure B.9: Fitted curve to pitch

From the fitted curve, the coefficients is found to be :

$$d_\theta = 1.38 \quad (\text{B.40})$$

$$B_\theta = 26.4861 \quad (\text{B.41})$$

B.1 Results

Table B.1 shows the determined coefficients.

Axis	Coefficients
x_b	$d_x = 0.11$, $d_{nl} = 0.0005$
y_b	$d_y = 0.28$
ϕ_b	$d_\phi = 1.14$, $B_\phi = 23.269$
θ_b	$d_\theta = 1.38$, $B_\theta = 26.4861$
ψ_b	$d_\psi = 0.27$

Table B.1: Table of Coefficients

B.2 Conclusion

While the parameters shown in Table B.1 is estimated using the data obtained by the described methods, it is important to notice that an error occurred causing the data from to be down sampled from assumed 100Hz to 6.25Hz. This was caused by a script intended to be run during the initial startup process, setting the sample rate to 2000Hz instead of the default 125Hz. As a result the coefficients found based on these measurements is expected to have larger than initially assumed error margins, they are however still considered to be representative of the dynamic system.

Additionally it was found during testing that the described method of obtaining heave dynamics could not induce the significant oscillations on the system, presumably because the required forces was larger than expected, meaning the results are omitted.

C | Extracting Pull Test Data

C.0.1 Purpose

The purpose of this Journal is to obtain the relationship between motor signal and output force. The relationship is based upon measurements taken by a previous project to establish Throttle to engine power ratio of the actuator. As it have not been possible to get access to the raw measurements, meaning the only data available is a graph within the Report. [28]

C.0.2 Theory:

The relationship between the motor signal and the force can be found by measuring the force delivered by the motor given different inputs. The force is measured by attaching the vessel to a static point with a string attached to a dynamo meter. The forces acted upon the vessel also acted upon the string, under the assumption that the string isn't relaxed and the vessel is not planning. By measuring the force acted upon the string with the dynamo meter and linking it to a motor input a model for the motor behavior can be obtained.

C.0.3 Method of Extraction

As the only data obtainable from the test is the graph shown in Figure C.1, the data needs to be extracted from this. [28] This is done by measuring the axis corresponding to each sample interval. The measurement starts at a measured throttle position of 45° and ends at 15°. It is known that at 45° there is no output from the thruster. This will be used to establish a baseline for the test, as forces acting upon the system here then must be external.

A scale of the graph can be established by measuring the distance between two given y-values of the graph, then dividing this by the values to the corresponding value as shown in ??.

$$scale = \frac{value}{distance} \quad (C.1)$$

Multiplying this with every measured value returns the Force in Newton.

In order to extract the values from the graph, a digital ruler is used. For this the graph is imported into Inkscape v.0.92.2 where the "Measurement Tool" is used. Each data point is measured in pixels

C.0.4 Data

The graph obtained from the previous project is shown in Figure C.1.

Appendix C. Extracting Pull Test Data

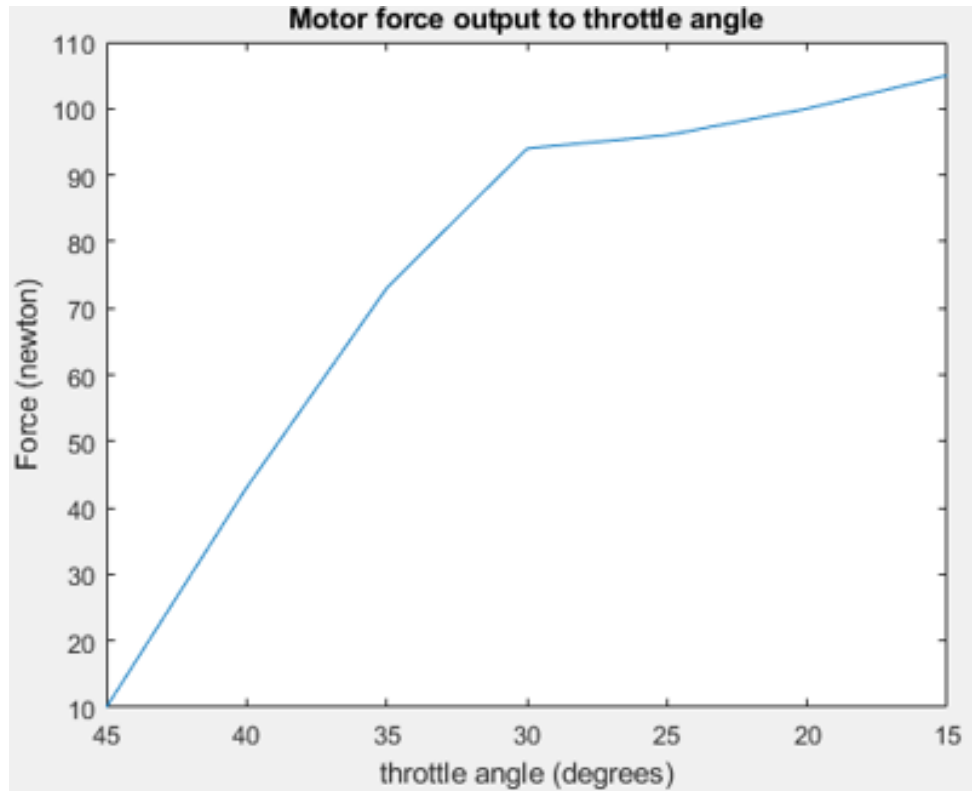


Figure C.1: Measured Throttle to Force Ratio

The extracted data is shown in Table C.1.

Angle	Measured Height	Equivalent Force output
40°	90.72 px	32.905N
35°	171.57 px	62.230N
30°	229.33 px	83.181N
25°	235.35 px	85.365
20°	247.02 px	89.597N
15°	259.94 PX	94.284N

Table C.1: Throttle to Force ratio

C.1 Stim Driver: Datagram extraction

The stim driver is the interface responsible for reading and decoding the data received from the Stim300 IMU. The purpose of this appendix is to outline the necessary knowledge for understanding how to operate the imu, and document how the datagram is decoded and implemented on the system. The Driver consists of two parts, a Initialization script, and the driver obtaining the data.

From the data sheet it can be seen that the driver have 3 modes; Initialization mode, normal mode and service mode. The data sheet also states that the standard baud rate is 921600 baud with no stop or parity bits.

The Initialization mode is the first mode the IMU enters when powered on. This mode initializes and synchronizes the internal sensor references and transmits manufacturer information about the unit.

When the unit is successfully initialized, it enters Normal mode. When in this mode, the unit transmits the datagram, with the configured sample rate. From this mode the system is able to enter the initiation mode if the external reset button is pressed or it receives a reset signal. When reading the datagram, it is important to ensure the data is valid by checking the status bytes as the unit keeps sending data regardless of errors. Additionally when the unit first enters Normal mode, the startup subroutine is run. During this period, the gyros is being stabilized, and data reviewed form these during that period should be considered non-valid. This is indicated by setting bit 6 in the STATUS byte 1 which will be 0 when the gyros is usefully stabilized. The datagram used in this project contains gyro, accelerometer and inclinometer data. The datagram have a constant length of 38 bytes including the identifier byte.

1. Identifier byte (1 byte)
2. Gyroscope data (3x3 bytes)
3. Gyroscope status (1 byte)
4. Accelerometer data (3x3 bytes)
5. Accelerometer status (1 byte)
6. Inclinometer data (3x3 bytes)
7. Inclinometer status (1 byte)
8. Sample Counter (1 byte)
9. Latency (2 bytes)
10. Cyclic redundancy Check (4 bytes)

The identifier byte is used to look for a beginning of a data gram. For the datagram type used within this project, the identifier is 0x93 This is used to ensure the bitstream is properly synced, as these have to be 38 bytes apart.

Appendix C. Extracting Pull Test Data

If the 38th byte is found not to be the identifier, the driver enters search mode where it looks for the next instance of 0x93 and checks one datagram ahead, meaning it will sync eventually.

D | Noise Test: IMU

Date: 2017-10-3

D.0.1 Purpose

Measure noise of IMU sensor unit to obtain the Allan variance. By measuring the unit while stationary, and no external forces applied the measurement noise can be extracted.

Theory

For this analysis the Allan Variance is used, which is a IEEE accepted standard for evaluating MEMS sensors. This method is used to analyze the random drift characterization of devices, such as MEMS-based IMUs.

Obtaining root Allan plot

The root Allan variance analysis relies on obtaining a stationary set of samples over a period of time. The data must be discreetly sampled data with constant sample rate τ_0 .

In general the more data acquired, the more accurate the analysis becomes. The method Divides measured data into M clusters of length $N\tau_0$. The average of each cluster is then computed by:

$$\bar{\Omega}(\tau) = \frac{1}{N} \int_{t_k}^{t_{k+1}} \Omega(t) dt \quad (\text{D.1})$$

Where:

- $\bar{\Omega}(\tau)$ Is the cluster average
- $\Omega(t)$ Is the measured Gyro output.
- τ Is the average period

The Allan variance is then computed by summing the normalized, squared difference between two adjacent clusters. The Allan variance for average time τ then becomes:

$$\sigma^2(\tau) = \frac{1}{2(N - 2n)} \sum_{k=1}^{N-2n} [\bar{\Omega}_{k+1} - \bar{\Omega}_k]^2 \quad (\text{D.2})$$

By repeating this process with various cluster sizes, the root Allan plot is then generated.

Root Allan variance Plot Curve

A Root Allan variance plot allows the identification of the noise type and nature through inspection. Such plot is illustrated on Figure D.1 where the different noise contributions is shown. The slope of the curve indicates which kind noise is dominating. In general, can the curve be

Appendix D. Noise Test: IMU

separated into three sections, namely **angle random walk**, **bias instability** and **rate random walk**.

The angle random walk is caused by high frequency noise, This type of noise is from sources with a very short correlation time, significantly lower than the sample time and can be reduced by integration. [29] This contribution will have a negative slope, reducing with integration time.

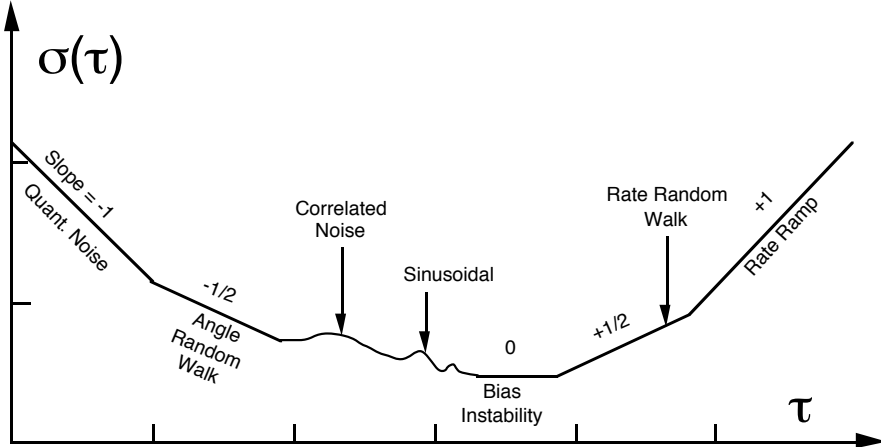


Figure D.1: Illustration of allan noise sources [29, p. 71]

At some point, the noise cannot be reduced more through integration and the curve will flatten. This region is the bias instability region, which is the theoretical best achievable performance of the unit.[29] At this point the bias of the unit is starting to become significant, and the accuracy of the measurements cannot be increased further by integration. This contribution can be identified by a slope of 0 on he root Allan curve, indicating that increasing sample time wont improve the measurement any further. [29]

At some point the bias starts to grow with integration time. As this type of noise oscillates with a much slower frequency, this contribution is not reduced by integration. When this is the case, the noise starts to increase with sample time. This type of noise can be identified as a noise contribution with a slope of 1.

Setup

List of Equipment

Instrument	AAU-no.	Type
Stim300	60764	
Computer	03039	

Procedure

1. Install required software on computer
2. Connect IMU to computer
3. Wait 24 hours
4. Retrieve Log
5. edit line 8 in script imu.m to match filename of data log

D.0.2 Results

D.0.3 Accelerometer

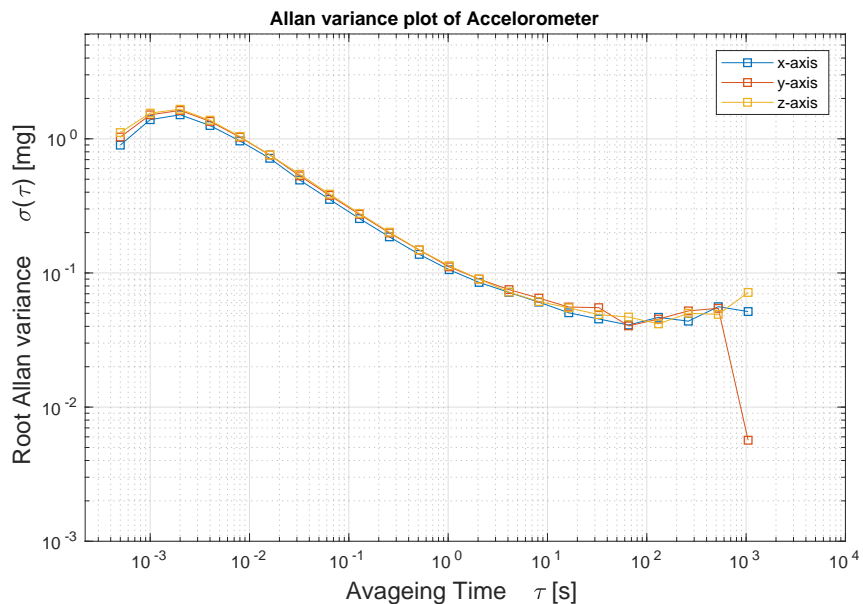


Figure D.2: Root Allan variance of the Accelerometer

The relevant coefficients is shown in Table ??

Axis	allan var @ $\tau = 0.005s$	allan var @ $\tau = 1000s$	bias instability
x	0.001154 g	5.156e-05 g	4.097e-05 g
y	0.001237 g	7.158e-05 g	4.033e-05 g
z	0.001281 g	5.668e-05 g	4.691e-05 g

Appendix D. Noise Test: IMU

D.0.4 Gyroscope

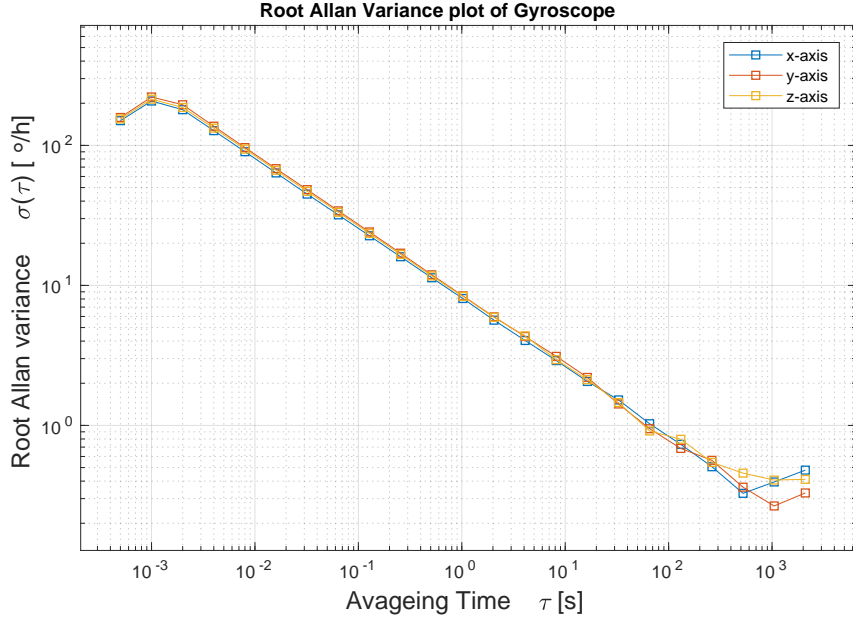


Figure D.3: Root Allan variance of the Gyroscope

The relevant coefficients is shown in Table ??

Axis	allan var @ $\tau = 0.005s$	allan var @ $\tau = 1000s$	bias instability
x	114.1 °/h	0.3868 °/h	0.3272 °/h
y	122.2 °/h	0.2718 °/h	0.4071 °/h
z	118.7 °/h	0.4111 °/h	0.2659 °/h

D.1 Evaluation

By inspection of the Allan curves and comparing them with the ones supplied my the manufacturer, data can be seen to be similar for the lower averaging times. [12] This means the measured data for a averaging time of 0.005s is considered to be a good representation. However, as this method is very computational expensive, sample data from the entire 24 hr period have not been utilizes, meaning the accuracy of the curve for larger integration times is questionable.

This becomes especially apparent from inspection of the Allan curve for the accelerometer, as the z axis is showing a significant jump. This is likely attributed to lack of data points when generating that part of the curve. While the bias instabilities of the accelerometer have been found to be close, albeit slightly lower, than the manufacturer specifications, they are considered a good representation of the actual value.

Appendix D. Noise Test: IMU

Regarding the gyroscope, these values seems to be more spread out, and deviate more from the $0.5 \frac{\circ}{hr}$ specified. These values should therefore be considered invalid, and instead rely on manufacturer specifications.

E | IMU Whiteness test

The purpose of this section is to analyze to which degree the IMU sensor data is WGN. Some noise reduction techniques, such as the kalman filter, relies on this assumption meaning noise types that fail to meet the requirements introduce potential uncertainties.

E.1 Theory:

In order for the sensor noise to qualify as being AWGN, it must be a normal, independent and identically distributed (IID) random process.[26] The noise can be analyzed by taking a set of stationary measurements, meaning no external disturbances affect the sensors while the measurements is taken, meaning only noise should appear on the sensors.

To test if the sensor noise meets these criteria, they must be verified individually. The sensor noise can be verified to be normally distributed through norm plot and histogram inspection. The autocorrelation describes the correlation between the samples, which shows if the samples are independent or not. If the sample set is highly correlated, it indicates that the samples are not independent and the noise is not WGN.

The data should be analyzed, keeping in mind that the discrete time-model, derived in section 5.1 and the test sample time is different by a factor of 1:10 meaning there is 10 samples in between each update of the model.

E.2 Results

The Following figures shows the Histogram, normality plot and autocorrelation for the Accelerometer, Gyroscope and Inclinometer. The test was performed over the span of 10 minutes with a sample rate of 2000Hz. The raw data from the sensor is used, with the exception of the inclinometer which have been converted from a 3-d vector to attitude using Equation 2.11 and 2.12.

E.2.1 Accelerometer

The autocorrelation plot of the accelerometer is shown in Figure E.1. From the graph it can be seen that the samples are correlated, 3 time lags ahead where after it becomes uncorrelated. While this fails the whiteness test, as there is correlation between the samples, the correlation time is significantly short that the measurements can be assumed white for all practical purposes.

Appendix E. IMU Whiteness test

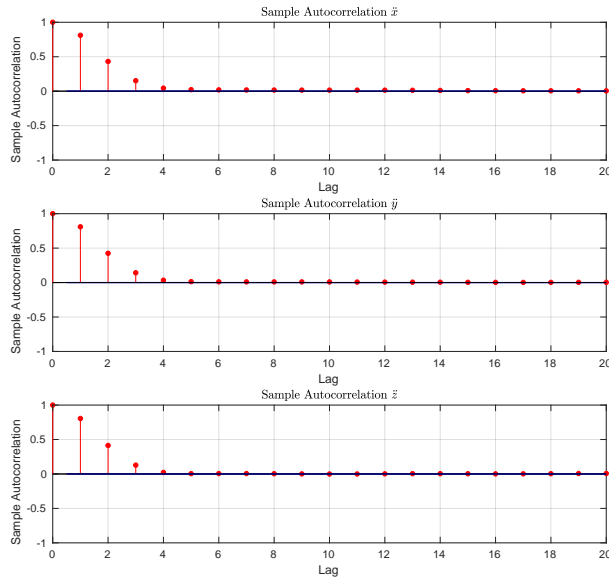


Figure E.1: Autocorrelation plot of the accelerometer

The Histogram and normally plots is shown in Figure E.2. While majority of the data follows a normal distribution, it can be seen that the axis show signs of a large kurtosis, which is most significant in \ddot{z} .

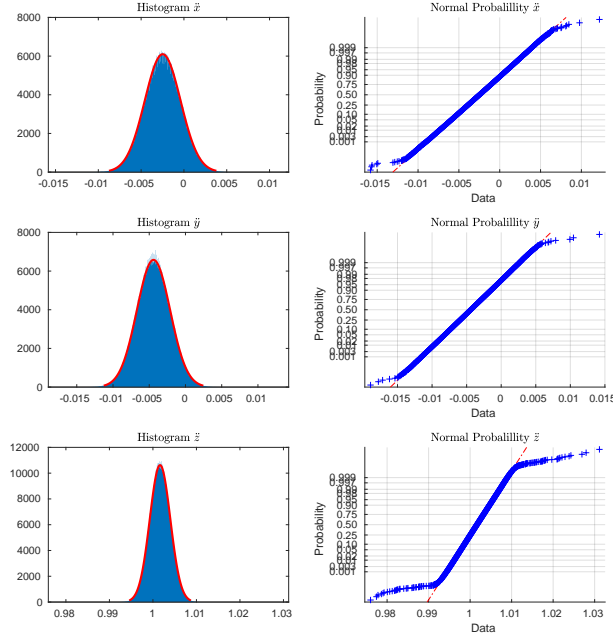


Figure E.2: Histogram and Normal plot of the accelerometer

Appendix E. IMU Whiteness test

E.2.2 Gyroscope

The autocorrelation plot of the gyroscope is shown in Figure E.3. Similarly to the accelerometer data, this sensor shows some signs of correlation, with a correlation time of 3-4 samples.

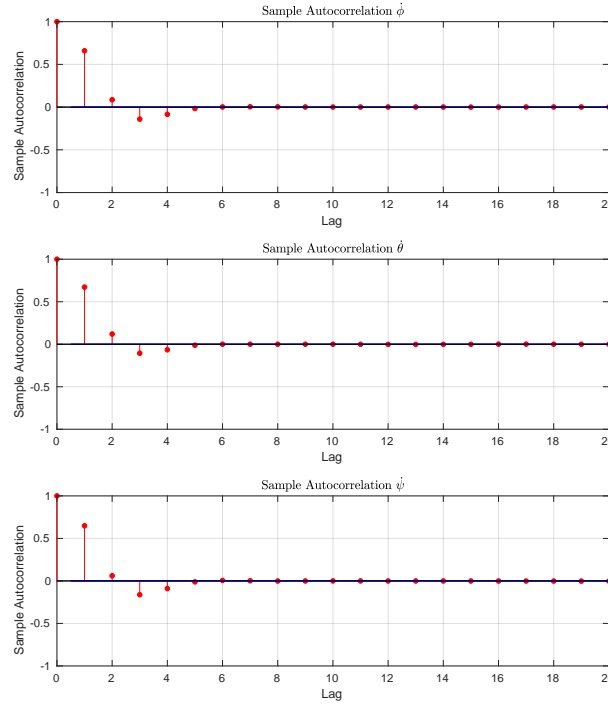


Figure E.3: Autocorrelation plot of the gyroscope

The Histogram and normally plots is shown in Figure E.4. From this is can be seen that the data is normally distributed, with no noticeable deviation from the normal distribution.

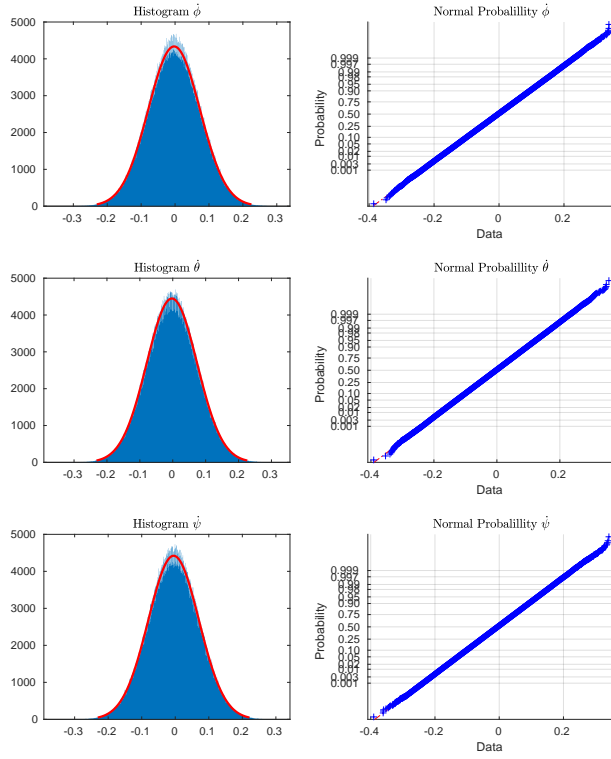


Figure E.4: Histogram and Normal plot of the Gyroscope

E.2.3 Inclinometer

The autocorrelation plot of the accelerometer is shown in Figure E.5. The measurements show a significant correlation time, which settles after around 40 samples. This correlation is significant enough to fail to approximate white noise, and fails the whiteness test .

Appendix E. IMU Whiteness test

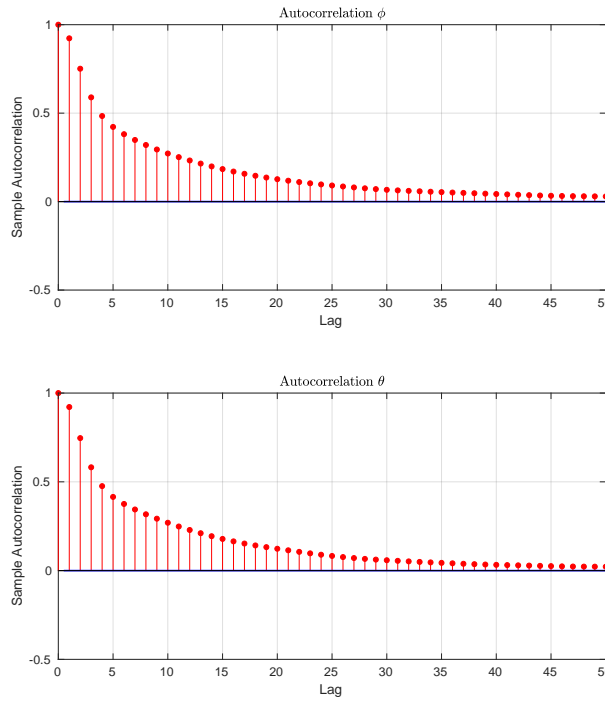


Figure E.5: Autocorrelation plot of the Inclinometer

The Histogram and normally plots is shown in Figure E.6. The data is shown to be normally distributed, with no noticeable deviation from the normal distribution.

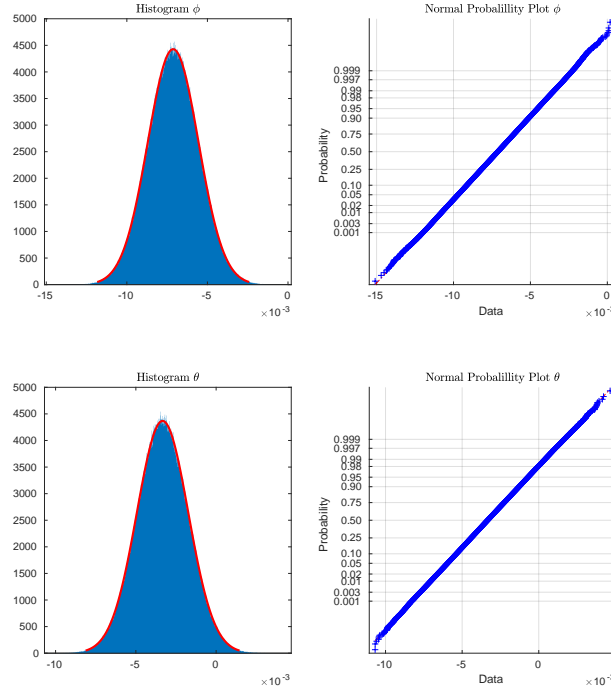


Figure E.6: Histogram and Normal plot of the Inclinometer

E.2.4 evaluation

The normality plot accelerometer indicated that the noise was not normally distributed. The origin of this is unknown, and could be a subject for further investigation if a problem arises, however as the majority of the deviation is seen on \dot{z} this could indicate that this is external disturbances due to the high sensitivity of the units. A potential source of this could be accelerations caused by vibrations through the floor the IMU is placed on.

As shown on the autocorrelation plots for the gyroscope and the accelerometer, some correlation exists between the first few samples. This have been attributed to the internal filter of the IMU. This effect is expected to be negligible, as the correlation between samples falls off before the system is updated. While this might be indicative of the non white noise coming from, the degree of it is deemed negligible. This can be shown by taking the autocorrelation of the data, downsampled to 200Hz from the 2kHz.

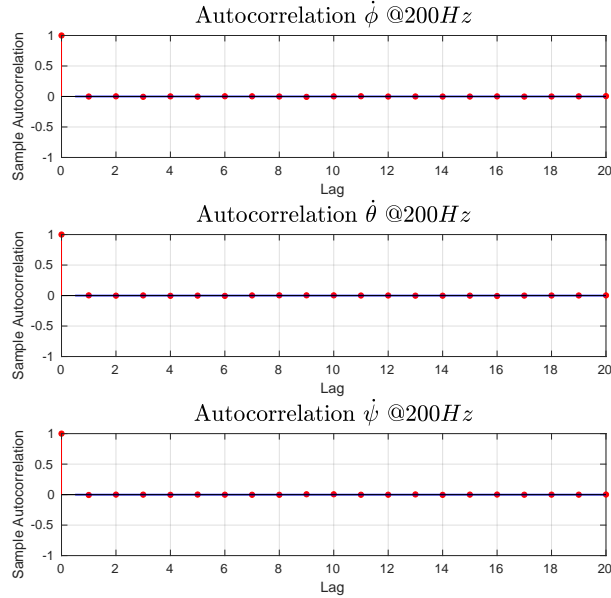


Figure E.7: Autocorrelation plot of the Gyroscope evaluated at 200Hz

Appendix E. IMU Whiteness test

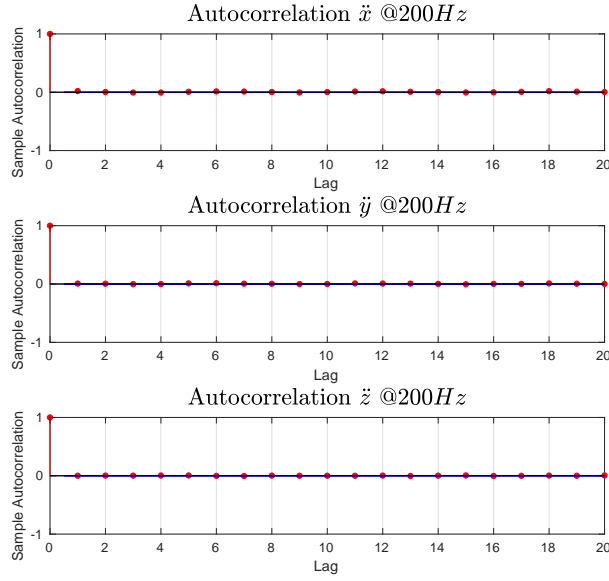


Figure E.8: Autocorrelation plot of the Accelerometer evaluated at 200Hz

From Figure E.7 and E.1 it can be seen that when evaluated at 200Hz, the data no longer appears correlated, and thereby can be considered white under this assumption. This is not the case for the inclinometer as shown in Figure E.5 as this still shows signs of correlation.

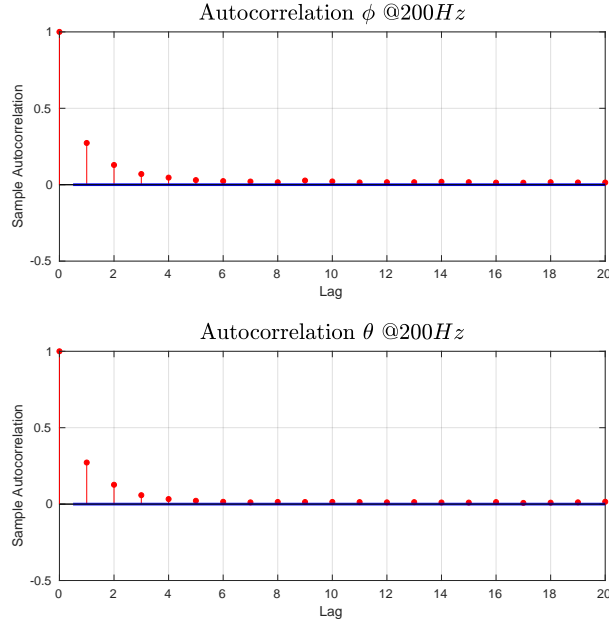


Figure E.9: Autocorrelation plot of the Inclinometer evaluated at 200Hz

Additionally, the impact of averaging the data to reduce noise have been verified. The data have been verified with a averaging time to match the 200Hz of the discretization. Figure E.10 shows

the autocorrelation of the averaged data. While it shows some increase in autocorrelation, this have been found to be negligible, as is wears off .

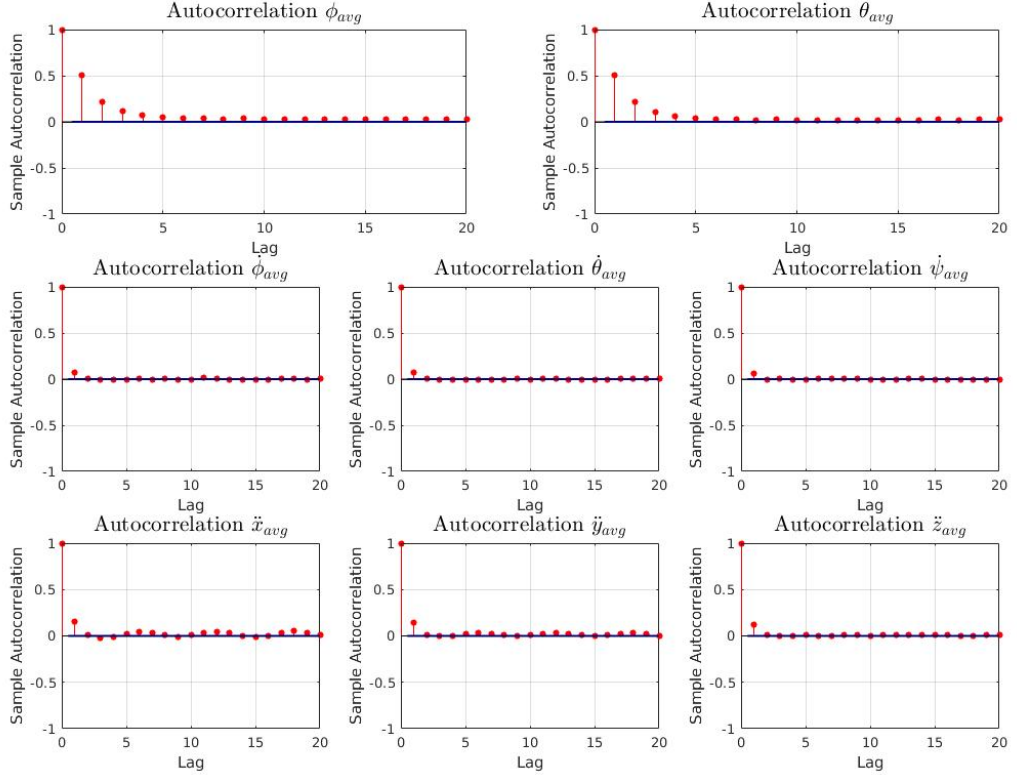


Figure E.10: Autocorrelation plot of the data averaged over 10 samples

E.2.5 Conclusion

The test have shown that the gyroscope and accelerometer data is approximately white when avaged and observed at 200 Hz, while the Inclinometer have found to be normally distributed but colored noise.

F | Measurement Journal: IMU misalignment

F.0.1 Purpose

The purpose of this test is to obtain the angular misalignment of the IMU. This will be used for calibrating the inclinometer for misalignment and initial bias. This test is obtains the constant bias of the IMU as well as the misalignment introduced by mounting the IMU in the casing. The following biases is obtained:

- Roll bias: $b_{\phi,con}$
- Pitch bias: $b_{\theta,con}$

F.0.2 Theory

The constant misalignment of the IMU is obtained by computing the offset of the measurements when the casing is placed on a leveled surface. The surface should be verified using a digital level to get as close to 0° as possible for the most accurate results. By analyzing the measurements as close to perfect level as possible, this eliminates external biases, which isolates the other sources of error; noise and internal bias of the system. The bias for each axis can then be obtained by taking the mean of the measurements over a period of time.

F.0.3 Procedure

1. Find or construct a leveled surface, this should be verified by a level.
2. Place the IMU mounted in the casing on a leveled surface.
3. Turn on the system and wait for 10 minutes such that the IMU is properly initialized.
4. Run the following command "roslaunch core imulog.launch"
5. Obtain inclinometer samples over a period between 40min and 1hr.
6. Retrieve the Log and import it into Matlab.
7. Run script "inclinometerBias.m" to obtain the bias for each axis.

F.0.4 Results

The result of the measurement is shown in Figure F.1.

Appendix F. Measurement Journal: IMU misalignment

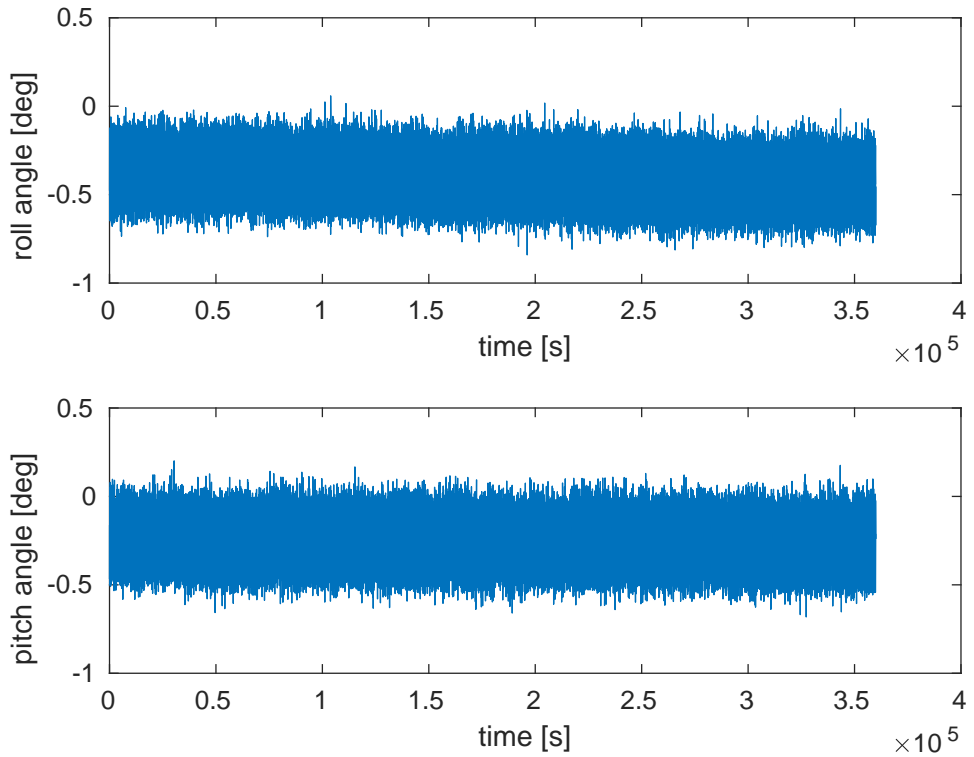


Figure F.1: Measurements used for taking the mean

From these measurements the following biases is obtainind:

$$b_{\phi,con} = -0.4^\circ \quad (\text{F.1})$$

$$b_{\theta,con} = -0.2539^\circ \quad (\text{F.2})$$

Appendix F. Measurement Journal: IMU misalignment

Measurement Journal: GPS

F.0.5 Purpose

The purpose of this test is to obtain the measurement noise levels of the GPS module. The test will determine the AWGN of the position as well as the heading measurements.

F.0.6 Theory

By sampling a set of measurements when the system is stationary, the noise of the GPS measurements can be isolated. As the noise is assumed to be zero mean AWGN, the describing factor is the variance of the noise. The mean of this type of noise will tend towards 0 as the sample size tends towards infinity, due to the law of large numbers . As a result a large sample set will provide better results.

Using the system configuration presented in this, the measurements is received as a NMEA string. The relevant NMEA messages for this test is the GGA and PTNL messages. The GGA message contains the longitude latitude and distance from sea level, while the PTNL message contains the heading information.

When the latitude longitude coordinates is obtained from the NMEA string, the sample average can be found. The average position is assumed to be the point closest to the actual position. When the average position is found, the haversine equation is used to obtain the distances from each measurement to the center point. [14]

$$a = \sin^2(\Delta_{lat}) + \cos(lon_m) \cdot \sin^2(\Delta_{lon}) \quad (\text{F.3})$$

$$c = 2 \cdot \text{atan2}(\sqrt{a}, \sqrt{1-a}) \quad (\text{F.4})$$

$$d = R \cdot c \quad (\text{F.5})$$

When the distance from the center is computed, the direction of the offset can be determined. The bearing between two GPS points can be computed by: [14]

$$x = \cos(lat_m) \cdot \sin(lat) - \sin(lat_m) \cdot \cos(lat)\cos(\Delta_{lon}) \quad (\text{F.6})$$

$$y = \sin(\Delta_{lon}) \cdot \cos(lat) \quad (\text{F.7})$$

$$\alpha = \text{atan2}(x, y) \quad (\text{F.8})$$

The deviation in x and y can the be found as:

$$\Delta_x = \cos(\alpha) \cdot d \quad (\text{F.9})$$

$$\Delta_y = \sin(\alpha) \cdot d \quad (\text{F.10})$$

When then measurements is converted to meters, the variance can be computed by:

$$\sigma_{\{x,y\}} = \frac{\sum \Delta_{\{x,y\}}^2}{N - 1} \quad (\text{F.11})$$

The heading variance in radians can be found by:

$$\sigma_\psi^2 = \frac{\sum (\psi_{deg} \cdot \frac{\pi}{180})^2}{N - 1} \quad (\text{F.12})$$

F.0.7 Procedure

The test procedure is as follows:

- Place system away from nearby obstacles
- Power on the system
- wait for 10 minutes for sensors to settle
- Run command "\$roslaunch core system.launch"
- Extract GPS-LOG-[date].log
- Analyze the data as presented in the theory

F.0.8 Results

Position Analysis

Figure F.2 shows the drift of the position measurements during measurement period.

Appendix F. Measurement Journal: IMU misalignment

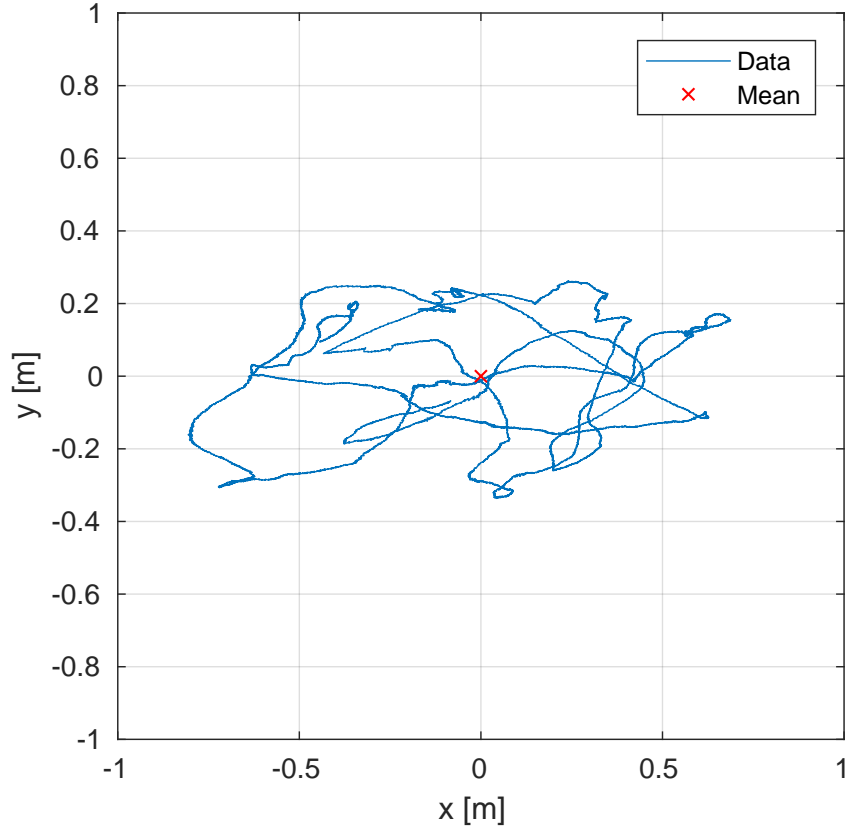


Figure F.2: plot of GPS measurement

$$\sigma_{\{x\}}^2 = 0.1460 \text{ m} \quad (\text{F.13})$$

$$\sigma_{\{y\}}^2 = 0.0260 \text{ m} \quad (\text{F.14})$$

Heading Analysis

$$\sigma_{\psi,deg} = 0.272^\circ \quad (\text{F.15})$$

$$\sigma_{\psi,rad} = 8.2910 \cdot 10^{-6} \text{ rad} \quad (\text{F.16})$$

Figure F.3 shows the distribution of the samples.

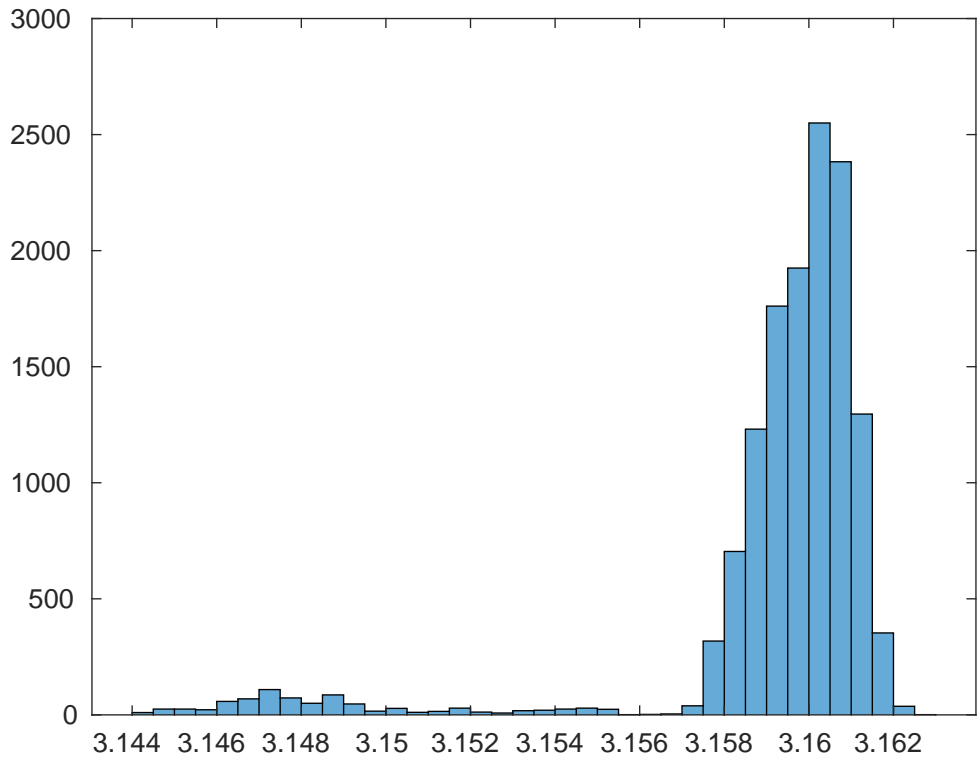


Figure F.3: Histogram of heading Measurements

F.0.9 Evaluation

Heading Analysis

By observing Figure F.3 it can be seen that a bell curve represent a significant part of the measurements with a smaller portion diverging from the Gaussian distribution. This smaller portion is shown to be within the first 1000 samples, as illustrated by Figure F.4.

Appendix F. Measurement Journal: IMU misalignment

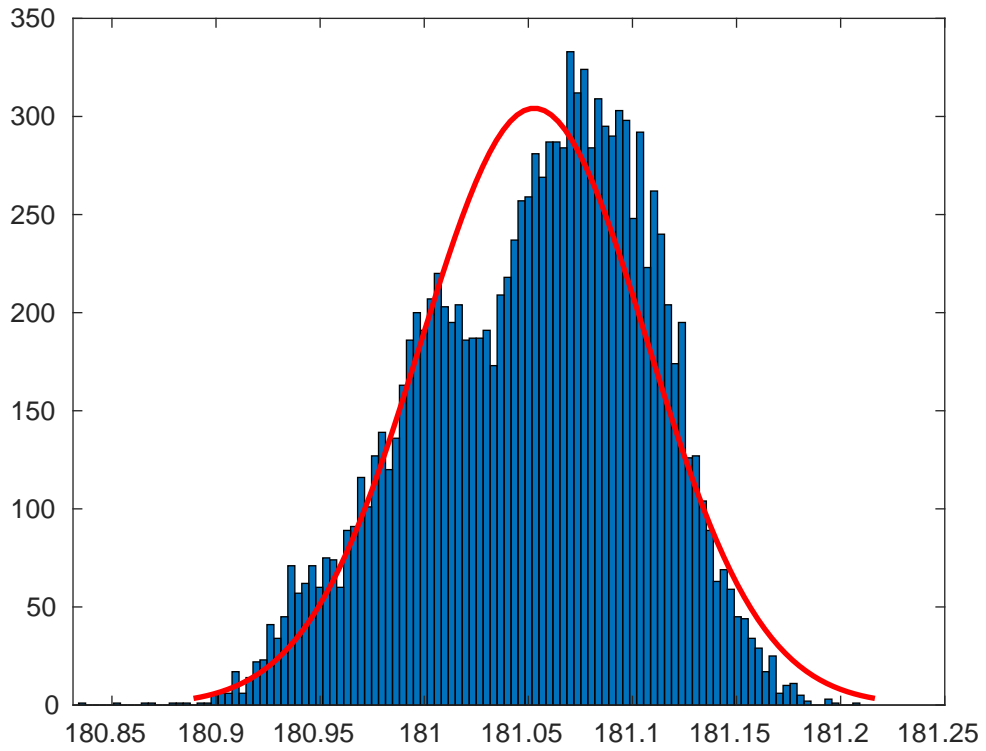


Figure F.4: filtered heading histogram

Additionally this is shown as an decreased variance of the as shown below:

$$\sigma_{\psi,deg,filt} = 0.030^\circ \quad (\text{F.17})$$

$$\sigma_{\psi,rad,filt} = 9.0616 \cdot 10^{-7} \text{ rad} \quad (\text{F.18})$$

Position Analysis

By evaluating the plot and variance it is clearly shown that the sensor produced a higher deviation in x_n than y_n indicating an error source in the measurements. In contrast to the heading, the position error sources is not improved by removing the first 1000 samples. A potential error source is the placement of the vessel in relation to surrounding buildings. As there were no good spot practically available for testing during the time of measurements, potential multipathing from surrounding buildings is a possible explanation for the deviation.

G | Coriolis and Centripetal Matrix

The position of CG in relation to $\{n\}$ is:

$$\vec{r}_{g/n} = \vec{r}_{b/n} + \vec{r}_{b/g} \quad (G.1)$$

Where:

- $\vec{r}_{g/n}$ is the distance between center of gravity and origin of $\{n\}$ [m]
- $\vec{r}_{b/n}$ is the distance between origin of $\{b\}$ and origin of $\{n\}$ [m]
- $\vec{r}_{b/g}$ is the distance between the center of gravity and origin of $\{b\}$ [m]

Assuming the center of gravity remains constant, the velocity, being the time derivative of the distance becomes becomes:

$$\frac{d\vec{r}_{g/n}}{dt} = \vec{v}_{g/n} = \vec{v}_{b/n} + \vec{\omega}_{b/n} \times \vec{r}_g \quad (G.2)$$

Using newtons second law of motion and equation 2.4 the following can be derived:

$$\begin{aligned} \vec{f}_g &= \frac{^i d}{dt} (mv_{g/n}) \\ &= \frac{^b d}{dt} (mv_{g/n}) + m\vec{\omega}_{g/n} \times \vec{v}_{g/n} \\ &= m(\dot{\vec{v}}_{g/n} + \vec{\omega}_{b/n} \times \vec{v}_{g/n}) \end{aligned} \quad (G.3)$$

Where:

- $\frac{^n d}{dt}$ Denotes the time derivative within the NED frame
- $\frac{^b d}{dt}$ Denotes the time derivative within the body frame

Equation G.3 describes the centripetal force contribution of the system when the boat frame rotates within the inertial evaluated at the center of gravity.

Similarly to the translational movement, the angular movement can found to be:

$$\begin{aligned} \vec{m}_g &= \frac{^i d}{dt} (I_g \vec{\omega}_{b/n}) \\ &= \frac{^b d}{dt} (I_g \vec{\omega}_{b/n}) + \vec{\omega}_{b/n} \times (I_g \vec{\omega}_{b/n}) \\ &= \vec{\omega}_{b/n} - (I_g \vec{\omega}_{b/n}) \times \vec{\omega}_{b/n} \end{aligned} \quad (G.4)$$

Equation G.4 describes the Coriolis forces.

Appendix G. Coriolis and Centripetal Matrix

Equation G.3 and G.4 can now be used to define:

$$C_{cen} \triangleq M_{11}(\dot{\vec{v}}_{g/n} + \vec{\omega}_{b/n} \times \vec{v}_{g/n}) \quad (G.5)$$

$$C_{cor} \triangleq \vec{\omega}_{b/n} - (M_{22}\vec{\omega}_{b/n}) \times \vec{\omega}_{b/n} \quad (G.6)$$

Where:

$$\begin{bmatrix} M_{11} & M_{12} \\ M_{21} & M_{22} \end{bmatrix} \triangleq M = M_{RB} + M_A \quad (G.7)$$

Which will be the sub indexes in the coriolis and centipedal matrix defined as:

$$C_a(\nu) = \begin{bmatrix} 0_{3x3} & C_{cen} \\ C_{cen} & C_{cor} \end{bmatrix} \quad (G.8)$$

This matrix contains the coriolis and centripedal forces acting upon the vessel

This results in the following Coriolis and inertial Matrix:

$$C_a(\nu) = \begin{bmatrix} 0 & 0 & 0 & 0 & -m_z\dot{z} & m_y\dot{y} \\ 0 & 0 & 0 & m_z\dot{z} & 0 & -m_x\dot{x} \\ 0 & 0 & 0 & -m_y\dot{y} & m_x\dot{x} & 0 \\ 0 & -m_z\dot{z} & -m_y\dot{y} & 0 & -I_z\dot{\phi} & I_y\dot{\theta} \\ m_z\dot{z} & 0 & -m_x\dot{x} & I_z\dot{\psi} & 0 & -I_x\dot{\phi} \\ -m_y\dot{y} & m_x\dot{x} & 0 & I_y\dot{\theta} & I_x\dot{\theta} & 0 \end{bmatrix} \quad (G.9)$$

H | Kalman Verification

H.0.1 Method

In order to verify the kalman filter, the whiteness of the residuals have been analyzed. Specifically the Verification is performed on the measurement residual. The simulation is performed with no external forces acting upon the vessel and with a thrust of 30N and a angle of the podded propel of $\frac{\pi}{5}$.

The simulation is performed using the model derived for the system in Appendix D, ?? and Appendix B. Additionally biases have been added to the accelerometer and gyroscope measurements using values derived from [stim] due to the Allan variance obtained in Appendix D showing significant uncertainties within this region.

H.0.2 Data

Figure H.1 shows the whiteness analysis of the positions. The horizontal velocities is shown to be white as they are normally distributed and contain no noticeable correlation. z_n is shown to be normally distributed but having mildly correlated samples.

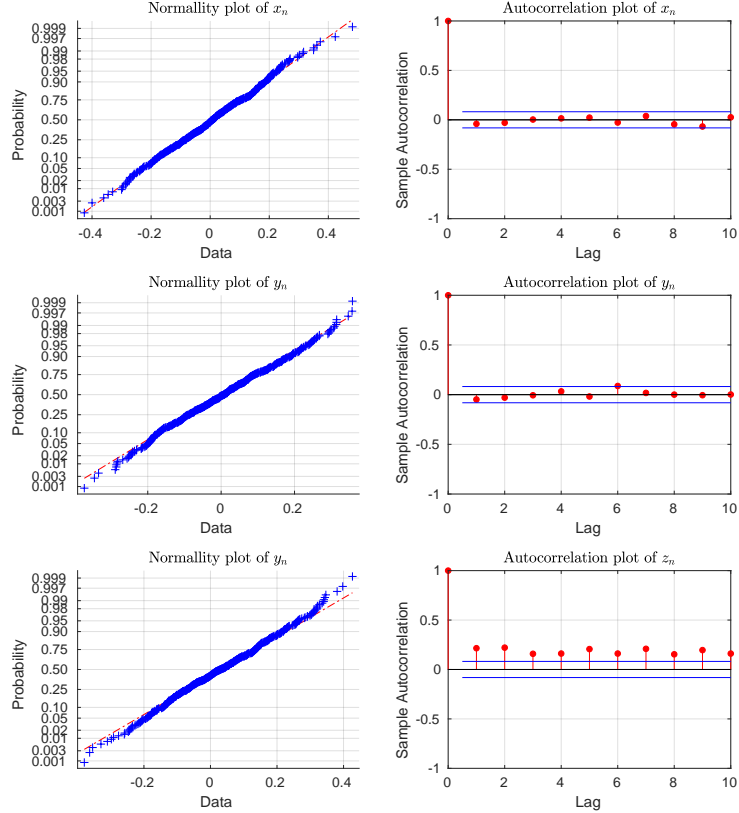


Figure H.1: Whiteness analysis of the in $\{n\}$

Appendix H. Kalman Verification

Figure H.2 shows the whiteness analysis of the orientation. ψ shows more correlation than ϕ and θ .

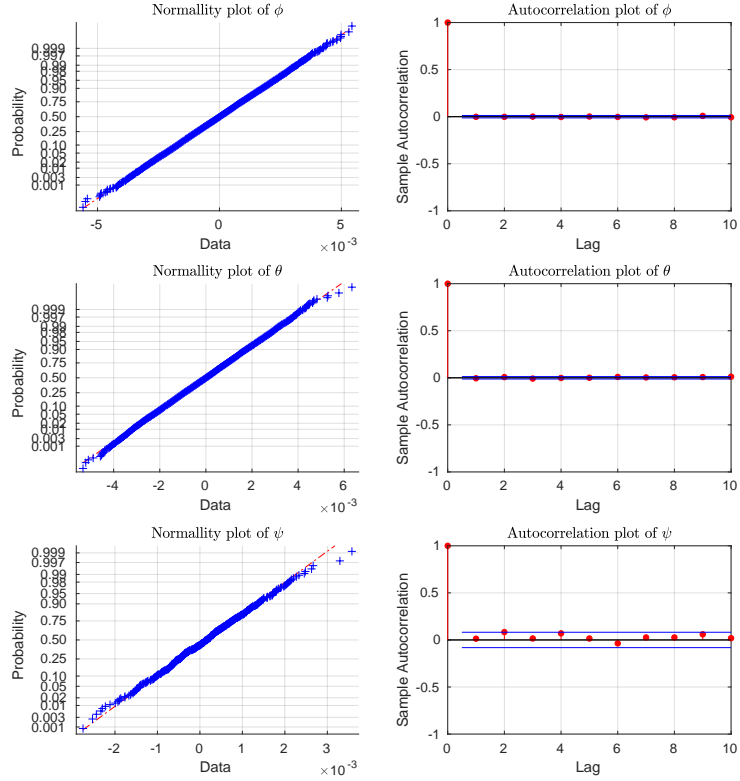


Figure H.2: Whiteness analysis of the orientation

Figure H.2 shows the whiteness analysis of the orientation. ψ shows more correlation than ϕ and θ .

Appendix H. Kalman Verification

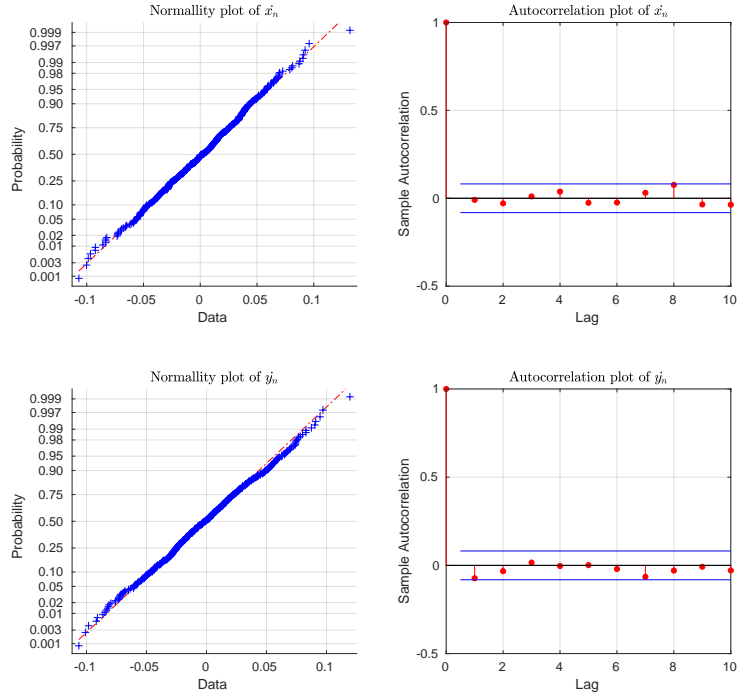


Figure H.3: Whiteness analysis of the translational velocities

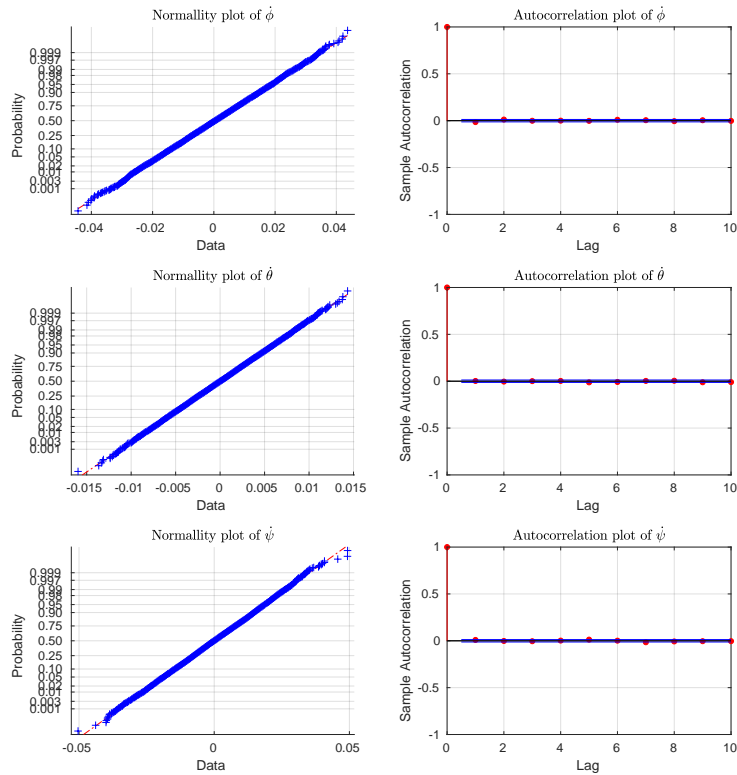


Figure H.4: Whiteness analysis of the angular velocities

Appendix H. Kalman Verification

Figure H.5 shows the whiteness analysis of the translational accelerations. All the residuals is shown to deviate from a normal distribution.

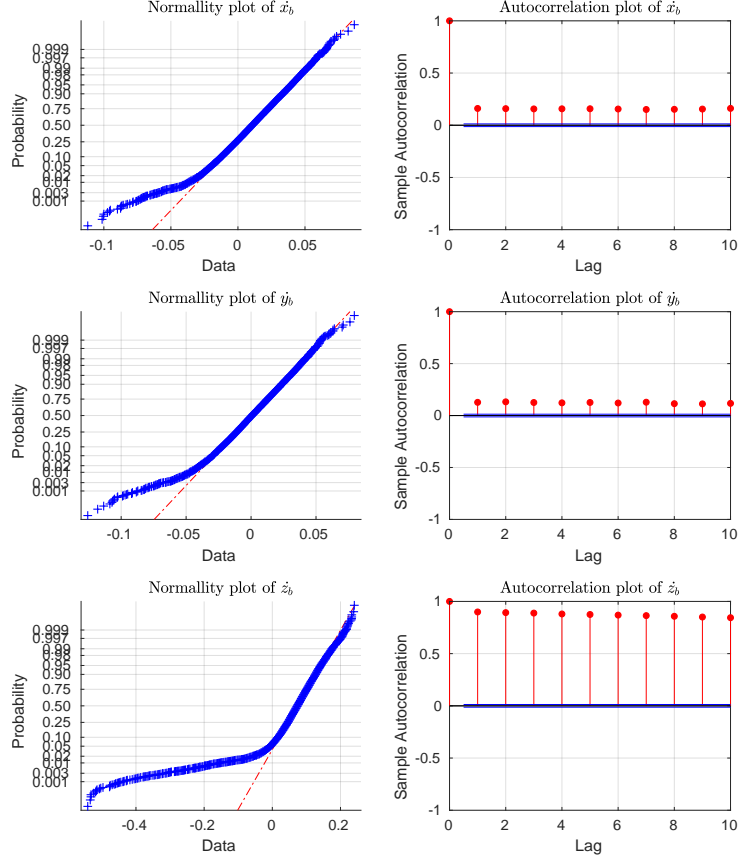


Figure H.5: Whiteness analysis of the translational acceleration

H.0.3 Conclusion

As shown the translational accelerations is not considered white. Where \ddot{z} also shows of significant correlation. It is unknown what causes said correlation, but it seems to impact the state estimate, as shown in ??

Bibliography

- [1] International Chamber of Shipping. *Shipping And Wold trade*. Aug. 11, 2018. URL: www.ics-shipping.org (visited on 08/29/2018).
- [2] I. Winkel Smith. *Bekendtgørelse om sejlads på Limfjorden mellem Egholm og Kattegat*. Aug. 11, 2018. URL: <https://www.retsinformation.dk/forms/r0710.aspx?id=65125> (visited on 08/29/2018).
- [3] National Ocean Service. *What is Hydrography?* Aug. 11, 2018. URL: <https://oceanservice.noaa.gov/facts/hydrography.html> (visited on 03/17/2018).
- [4] International Hydrographic Bureau. *Handbook of Marine Craft Hydrodynamics and Motion Control*. 2008.
- [5] Canadian Hydrographic Service. *Standards For Hydrographic Surveys*. 2008.
- [6] Biezl. *Hydrodynamik*. Apr. 11, 2018. URL: <http://e-learning.skaldyrcenter.dk/vandmiljoe/limfjordens-hydrodynamik> (visited on 12/15/2018).
- [7] Eric Weisstein. *Overdot*. Aug. 11, 2018. URL: <http://mathworld.wolfram.com/Overdot.html> (visited on 12/15/2018).
- [8] Brig. *Brig*. Aug. 11, 2018. URL: <http://brigboats.com/models/falcon-tender/falcon360/> (visited on 12/15/2018).
- [9] Ubuntu. *Ubuntu*. Aug. 11, 2018. URL: <http://www.ros.org/core-components/> (visited on 12/15/2018).
- [10] Ros. *Core Components*. Aug. 11, 2018. URL: <http://www.ros.org/core-components/> (visited on 12/15/2018).
- [11] Creative Commons. *Creative Commons*. Aug. 11, 2018. URL: <https://creativecommons.org/licenses/by/3.0/us/> (visited on 08/11/2018).
- [12] Sensonor AS. *Datasheet STIM300 Inertial Measurement Unit*.
- [13] Trimble. *Trimble MB-Two OEM GNSS Board*.
- [14] Movable Type Scripts. *Calculate distance, bearing and more between Latitude/Longitude points*. Apr. 11, 2018. URL: <http://e-learning.skaldyrcenter.dk/vandmiljoe/limfjordens-hydrodynamik> (visited on 12/15/2018).
- [15] Mark Looney. *The Basics of MEMS IMU/Gyroscope Alignment*. Aug. 11, 2018. URL: <http://www.analog.com/en/analog-dialogue/articles/mems-imu-gyroscope-alignment.html> (visited on 08/11/2018).
- [16] Thor I. Fossen. *Handbook of Marine Craft Hydrodynamics and Motion Control*. 2011.
- [17] Nasa. *Boundary layer*. Aug. 11, 2018. URL: <https://www.grc.nasa.gov/www/k-12/airplane/boundlay.html>.
- [18] Danmarks Metrologiske Institut. *sealevl*. URL: <https://www.dmi.dk/hav/maalinger/vandstand/> (visited on 12/15/2015).

Bibliography

- [19] Masayoshi Tomizuka Hoday Sterns. *Multiple model adaptive estimation of satellite attitude using MEMS gyros.* 2011.
- [20] Liang Xue et al. *Noise Reduction of MEMS Gyroscope Based on Direct Modeling for an Angular Rate Signal.* 2015.
- [21] Sebastian O.H Madgwick. *An efficient orientation filter for inertial and inertial/magnetic sensor arrays.*
- [22] Jean-Michel Pfliimlin. R. Mahony Tarek Hamel. *Nonlinear Complementary Filters on the Special Orthogonal Group.*
- [23] Mohinder S. Grewal and Angus P. Andrews. *Kalman Filtering Theory and Practice Using MATLAB.* 2008.
- [24] Francis Colas Roland Siegwart Gregory Hitz François Pomerleau. *State Estimation for Shore Monitoring Using an Autonomous Surface Vessel.*
- [25] Robert H. Ronge et al. *MEMS-based Inertial Navigation on Dynamically Positioned Ships Dead Reckoning.* 2016.
- [26] Steven Kay. *Intuitive Probability and Random Processes using MATLAB.* 2006.
- [27] Hiener Kuhlman. *Kalman-Filtering For Coloured Measurement Noise for Deformation Analysis.*
- [28] Anderas Flem Norman et al. *Autonomous Surface Vessel.* 2017.
- [29] Institute if Electrical and Inc. Electronics Engineers. *IEEE Standard Specification Format Guide and Test Procedure for Single-Axis Interferometric Fiber Optic Gyros.*